# INVESTIGATION OF NEW
# IONOSOUNDER TECHNIQUES

GFO PRICE    $ _____

CFSTI PRICE(S) $ _5.00_

Hard copy (HC) _____

Microfiche (MF) _1.25_

**NATIONAL AERONAUTICS AND SPACE ADMINISTRATION   •   WASHINGTON, D. C.   •   JUNE 1966**

# INVESTIGATION OF NEW IONOSOUNDER TECHNIQUES

Distribution of this report is provided in the interest of information exchange. Responsibility for the contents resides in the author or organization that prepared it.

Prepared under Contract No. NAS 5-9108 by
CUTLER-HAMMER, INC.
Deer Park, Long Island, N.Y.

for Goddard Space Flight Center

NATIONAL AERONAUTICS AND SPACE ADMINISTRATION

# ABSTRACT

The objective of NASA Contract NASA 5-9108 with
Airborne Instruments Laboratory, a Division of Cutler-
Hammer, Inc., was to study the feasibility of experiments
using radio sounding techniques for the investigation of the
ionospheric properties of Mars and Venus. The study effort
was divided into two areas. Constraints were applied in size,
weight, and power consistent with modern spacecraft technology.
The techniques study was concerned with instrumentation suit-
able for sounding a planetary ionosphere from nearby to
100,000 km from the planet in flyby or orbiting spacecraft.
A parametric analysis related power, resolution, frequency,
range, and other parameters of importance. A system analysis
was performed using the methods of modern radar systems and
applying them to ionospheric sounding. The results were
applied to a specific mission, such as a Voyager flight to
Mars, with requirements to sound from distances of 1000 to
40,000 km. A system to accomplish such a mission is described.
The various elements of this system are within the present
state of the art and the entire system is considered feasible.
Weights, sizes, and powers are given.

The theoretical studies investigated the propaga-
tion properties of an ionosphere in terms of propagation time
delay, doppler shift, polarization, and dispersion. It was
found that the principal method for sounding should be propa-
gation time delay and the bulk of the effort was applied to
virtual depth analyses and interpretation. The study was
carried out using magneto-ionic theory, assuming typical
models for the electron density profiles and taking the mag-

netic field strength and direction as variable parameters. Useful relationships were found between the incremental path length increase due to the ionosphere and the scale height and magnetic field. Interpreted in terms of virtual height, a data analysis technique was evolved that should permit a reasonable first approximation to the ionospheric profile and planetary magnetic field. A more refined analysis can be attempted from this approximation using known techniques. These known techniques require the stipulation of a magnetic field prior to analysis, which is unknown in the early planetary ventures. Although the results of Mariner 4 were not known until the end of this program, these techniques are still of interest for other planets such as Jupiter. For Mars, which has no magnetic field, they simplify considerably.

The report recommends continued efforts. Those techniques that were evolved for long-distance sounding should be developed further, starting initially from a breadboard phase. Studies should be continued with respect to system design and equipment specifications, the further analysis of propagation aspects, data reduction and interpretation methods, analyses of the significance of measurement and interpretation errors, and the physics of the ionospheres of both planets.

# TABLE OF CONTENTS

# LIST OF ILLUSTRATIONS

# SECTION 1
## INTRODUCTION

This final report describes a feasibility study
of experiments using radio sounding techniques for the
investigation of the ionospheric properties of Mars and
Venus. The present contract (NAS 5-9108) was a follow-
up of another contract awarded by NASA to Airborne Instru-
ments Laboratory (AIL) in 1962 (NASW-513) in which plane-
tary sounder techniques were investigated. The object of
the present contract was a broader, more comprehensive
investigation than the earlier effort.

The work was divided into two coordinated main
tasks--a theoretical investigation of the propagation prop-
erties of an ionospheric medium in terms of those param-
eters that might be instrumented, and studies of instru-
mentation suitable for sounding a planetary ionosphere from
near to far-off distances. Ranges were considered out to
100,000 km and the effort is applicable to both flyby as
well as orbiting spacecraft.

Knowledge of the atmospheres of Mars and Venus is
extremely limited and is based upon observations from the
Earth and the Mariner 2 and 4 missions. The data is very
sparse in comparison with the Earth, and the electron density,
constituents, and temperature of the planetary ionospheres
are not very well-known. Theoretical models have been derived,
but are too speculative to be relied upon very seriously.

A scientific investigation of a planetary ionosphere
must include measurements of the degree of ionization, the
source, the neutral and ionized constituents, the upper atmos-
pheric temperature profile of neutral, ionized and electron
particles, and the magnetic field within the ionosphere.

Radio sounding techniques have successfully measured the electron concentration at a distance, and presumably the total ion concentration. The scale height can be determined and, assuming thermal equilibrium, temperatures may be derived if an atmospheric model can be deduced. However, differences in neutral, ionized, and electron particle temperature, and neutral particle and specific ion densities have not been established using such techniques. High-power scattering can be used to provide some temperature information, but there are many practical difficulties in implementing such techniques for space use.

Existing sounding techniques are limited in range due to power, weight, and size constraints. Planetary missions will range from flybys to orbiters, and a sounding experiment will be required to function to very large distances, on the order of 40,000 to 100,000 km. Where the range is small, existing techniques can be used, such as that provided by the Alouette satellite or the Explorer XX. However, in close approaches, it would be desirable to use more advanced methods measuring much more data, in particular those parameters not measurable by existing techniques. For much longer ranges, on the other hand, it is necessary to use techniques that will be able to measure, at the very least, those parameters presently measured at close range. However, such long-range techniques must meet power, weight, and size requirements.

During the study various techniques were investigated in terms of their performance with respect to range, power, weight, size, and complexity. The goal was to be able to specify those techniques to be used for a specific mission.

The study was at first general, and the results parametric in nature. Toward the end of the study the results of the investigation were applied to more specific missions such as the Voyager Mars orbiter. These matters are described more fully in Section 3.

The intent of the theoretical propagation studies was to evaluate those ionospheric characteristics that were measurable from a distance. These characteristics include propagation time delay, doppler shift, polarization, and dispersion. It was found that doppler shift and polarization were only useful with a second cooperative station, such as a receiver or transmitter, placed on the planetary surface. With respect to dispersion, the necessary precision of waveform analysis and generation precluded a simple system. Nevertheless, a fuller examination of methods for using the information contained within waveshapes remains to be accomplished and may prove fruitful.

The bulk of the theoretical effort was applied to delay-time analyses and some effort was applied to the interpretation of such measurements. In the general planetary situation, unlike topside sounding of the Earth's ionosphere, an initial experiment lacks a suitable model of the planet's magnetic field which is of utmost importance in the interpretation of data. However, much information can be obtained from sounding data concerning the magnetic field, and this from measurements at a distance.

The study was carried out using magneto-ionic theory, assuming typical models for the electron density profiles and taking the magnetic field strength and direction as variable parameters. Scale heights were chosen based upon an isothermal, constant-g model with the constituents in diffusive equilibrium. Although the results appear most useful, they require further

treatment and confirmation for models with dipole fields, inverse square gravitational forces, and temperature distributions similar to those found from Earth backscatter measurements. Fuller details of these studies are described in Section 4.

Section 2 contains a general summary of the pertinent knowledge concerning Mars and Venus and the theoretical treatments of their upper atmospheres and ionospheres. This information was applied in establishing suitable models and requirements for an ionospheric sounder mission. The requirements are also fully described as well as the reasoning appropriate to their specification. Various present-day sounding techniques are also briefly reviewed for orientation with respect to a planetary mission.

Section 5 summarizes the recommendations resulting from these studies. **The report also contains a bibliography and several appendices in which pertinent mathematical relationships are derived.**

Certain terminology is used in this report. Most of it is that common to the ionospheric propagation and radar disciplines. Scale height referred to herein is the electron density scale height, which is usually taken as twice the neutral scale height. The symbol H used here is the electron density scale height and not the neutral particle scale height. To distinguish between the propagation modes, the small letters o (ordinary) and x (extraordinary) are used. The use of small letters also distinguishes the x-mode from the commonly used plasma frequency parameter X. In addition, the x-mode is not taken as including the z-mode which may propagate for $Y < 1$ if the plasma frequency parameter meets well-known condi-

tions. Finally, propagation in this report is taken as those paths which are vertical or nearly vertical in the main and produce reflection by the ionosphere that returns to the space-craft. As such, oblique propagation paths were not included nor whistler-type propagation. This was not done to minimize the possible importance of these paths, but rather because the scope of the program necessarily limited the efforts.

# SECTION 2
## GENERAL DISCUSSION

A. **THE PLANETS MARS AND VENUS**

Basic data on Mars and Venus have been taken from Rasool[1], who has compiled this information from various sources. The data are shown in Table I.

### TABLE I
### DATA ON MARS AND VENUS

|  | Mars | Venus |
|---|---|---|
| Mean distance from sun | 1.52 AU | 0.72 AU |
| Mean equatorial diameter | 6810 km | 12,240 km |
| Length of day | 1.0012 Earth days | 250 Earth days* |
| Length of year | 1.8808 Earth year | 0.613 Earth year |
| Mass | 0.1078 Earth mass | 0.81 Earth mass |
| Mean density | 4.12 gm/cm$^3$ | 4.8 gm/cm$^3$ |
| Gravity | 377 cm/sec$^2$ | 842 cm/sec$^2$ |
| Total integrated albedo | 0.26 $\pm$ 0.02 | 0.73 |
| Effective blackbody temperature | 209$^{\circ}$K | 235$^{\circ}$K |

---

* Carpenter and Goldstein[2].

7

Certain of the numbers in Table I are not agreed upon by all authorities. However, there is close agreement, and for the purposes of this report the numbers are suitable.

Carbon dioxide is the only gas in the atmospheres firmly detected on both planets.[3-16] Some $H_2O$ has been detected on Mars.[3] The atmosphere of Venus is far more uncertain due to its thick cloud cover, and far less is known about it than Mars. There is considerable uncertainty about the surface pressure of Mars, with values of various investigators ranging from 85 mbars down to 10 mbars.[3-11] Mariner 4 may have cleared up this uncertainty, and preliminary results available during the writing of this report indicate a surface pressure of about 4 to 5 mbars.[17, 18]

Although the atmospheres of Mars and Venus may contain any of a variety of gases in addition to $CO_2$, it is common practice, because of abundance and extrapolation of the Earth's atmosphere, to take nitrogen as the major constituent.[5, 10] In any event, the gases must be of sufficient mass to have a time of escape greater than the age of the planet. The exospheric temperature cannot be too high for the assumed constituents. These considerations lead in turn to an ionosphere which is due to ionized atomic oxygen that is supplied by the photodissociation of $CO_2$. The exospheric temperature must then be less than the value which would lead to an oxygen escape time of about $3 \times 10^9$ years. It is expected that the light gases, hydrogen and helium, will have mainly escaped. However, like the Earth, there may be residual layers of helium and hydrogen contributed to by outgasing or solar influx. Argon and neon may also be significant constituents of the Mars and Venus atmospheres.

For this program, it was assumed that $CO_2$ was the principle source of ionized constituents. At some altitude below the peak electron density, $CO_2$ was assumed mostly

dissociated into CO and O. $O_2$ formed by three-body recombination would be of some importance below the peak ionization level and, in diffusive equilibrium, the lighter mass of atomic O would make it the principle constituent absorbing solar radiation below 900 A. This reasoning leads to a single-constituent upper ionospheric layer of $O^+$ for both Mars and Venus. In addition, if hydrogen and helium exist as upper layers, similar to the Earth,[19] another model of the ionosphere could be assumed with $O^+$ the principle ion in the region immediately above the peak density and $He^+$ and $H^+$ the principle ions at much higher levels. Models were selected as described in Section 4 based on these considerations.

Several theoretical studies have been made of the atmosphere and ionosphere of Mars and Venus. The results of these studies aided in judging suitable peak levels and scale heights for the models used during the program. Figure 1 illustrates the ionospheres derived for Mars by Danilov,[20] Chamberlain,[21] Yanow,[22] and Norton.[23] Theoretically derived ionospheres of Venus were derived by Danilov[20] and Norton.[23] In all cases, $O^+$ is the principal ion above the peak density consistent with the thinking previously described.

For Mars, the theoretically derived peak densities and scale heights differ. Yanow proposes a peak of $2 \times 10^4$ el/cc, Danilov $1.5 \times 10^5$ el/cc, Chamberlain $10^5$ el/cc, and Norton $1.5 \times 10^5$ el/cc. The electron density scale heights for the same order of authors are roughly 26, 46, 200, and 250 km. Theoretical studies by McElroy and Chamberlain[24] have been for exospheric temperatures from about 600 to $1200^{\circ}K$. Norton's temperatures are higher and the presence of a magnetic field is very important with respect to escape time and the exospheric temperature.
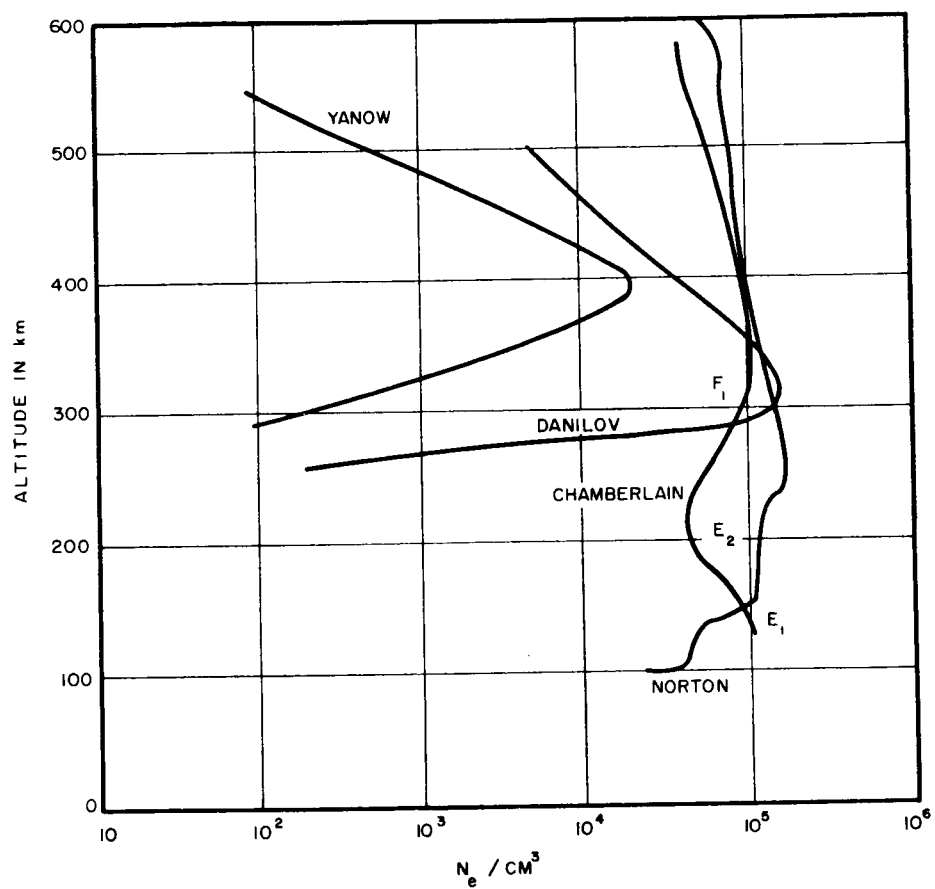
FIGURE 1. IONOSPHERIC MODELS FOR MARS (ELECTRON DENSITY VS ALTITUDE)

10

For Venus, Danilov derives a peak ionization of about $4 \times 10^5$ el/cc with an upper electron scale height of about 15 km. Norton's peak value varies with sunspot number. At sunspot minimum, he finds about $10^6$ el/cc and an electron scale height of about 200 km and at sunspot maximum about $4 \times 10^6$ el/cc with a scale height of about 500 km. Danilov's exospheric temperature is very low whereas Norton used much higher temperatures.

The variation between all of these theoretical treatments is considerable and, in any event, the results are highly speculative. In choosing a profile, the works of Chamberlain and Norton were considered most significant. Although the work performed during the program was not critically dependent on the accuracy of the profile some degree of consistency was attempted. Furthermore, it did not matter whether the selected profile was applicable to Mars or Venus, since the nature of the results of the present study are applicable to either. Furthermore, until such time as a frequency range for sounding must be selected, such differences are not important. Since the earliest missions available for a sounding experiment were destined for Mars (Voyager 69, 71, and 73), the profile was selected based on the theoretical work for Mars. Norton had used too high a total atmospheric density, since his work was based on earlier estimates[7] and the measurements of Kaplan, Münch, and Spinrad[3] were not known by him until the end of his work. Furthermore, Chamberlain's arguments for lower temperatures were reasonable in terms of the escape of atomic oxygen. In addition, the peak density is quite uncertain, since it is controlled by the recombination and diffusion processes in the peak region, which in our present state of knowledge are quite uncertain. It was considered likely that the peak density could range anywhere from $10^5$ to $10^6$ el/cc at an altitude of 200 to 400 km, the peak only

affecting the minimum penetration frequency. (The Mariner 4 results were not available till the writing of this report.) Consequently, a model was used with an $O^+$ scale height of 120 km. This represents a neutral particle exospheric temperature of about $500^O$K. Although this may be too low for Mars with a magnetic field, it was a reasonable choice for computational purposes. Nevertheless, results for other scale heights are readily determinable from the theoretical results. In the more complex model, including He and H layers, a mean scale height was chosen based on a mixture of He and H for the upper region.

At the start of this program, it was believed that Mars had a magnetic field based on the 21.2 cm observations of Davies and Williams.[25] Neither the magnitude of the magnetic field nor its orientation were known. Consequently, it was decided to include the magnetic field as an important set of parameters, and various values of gyrofrequency and angular orientation were assumed. The interpretation of data in terms of the field parameters was considered of much significance. For the propagation studies, it was considered sufficient to take the magnetic field as constant in magnitude and direction at the chosen parametric values. Since Mariner 4 has recently found no sensible magnetic field near Mars and Mariner 2 had found the same for Venus, the field, mode splitting, and propagation are of little importance for Mars or Venus. The results of the study are still applicable, though simpler, to Mars and Venus. In their more complex aspects they are still applicable to other planets with magnetic fields, such as Jupiter and Earth.

B. REQUIREMENTS FOR SOUNDING

Requirements were considered relative to sounding distance, precision of virtual depth measurements, resolution, frequency range, weight, size, power and other charac-

teristics dependent on flight trajectory relative to the planet. These requirements are considered very tentative, since firmer specifications can only be applied for definite missions. Consequently, the following discussion and requirements were established primarily as a guide and for specifying parameter ranges.

### 1. SOUNDING DISTANCE

Since planetary missions may range from flybys to orbiters, and since such complex missions could conceivably miss their intended trajectories, ranges from as far out as feasible to near distances are necessary. At extreme ranges, power is a very significant limitation and resolution and precision require stable equipment.

The maximum Mariner distance provided for the previous study (Contract NASW-513) was 40,000 km, and it was decided to equal or better this distance. Preliminary indications had shown that a range to 100,000 km could be considered, and this was chosen as the maximum range for feasibility analysis.

### 2. PRECISION AND RESOLUTION

Precision refers to the inherent ability of equipment to measure the virtual depth of a particular layer. Resolution involves the ability to separate two echoes. Numerical values which should be attached to both requirements depend to a certain extent on the scale height of the profile. The greater or smaller the scale height, the larger or smaller these values may be for the same degree of derived information. The smaller the precision and resolution, the greater the precision or stability of the required components.

From the standpoint of present practice in sounding from the topside of an ionosphere and because the electron density scale height may range from 100 km and above, 50 km

was set as a target requirement for both precision and reso-
lution. Resolution and precision were used parametrically,
and it was realized that it might be necessary to permit less
resolving ability at very far ranges with practical instru-
mentation.

### 3. FREQUENCY RANGE

For the expected range of electron densities, a
sounding frequency range from 0.5 to 20 Mc was chosen. It
was recognized that the 0.5-Mc lower limit requires longer
antennas for efficiency, but this figure represents a reason-
able compromise between power and reflections at as high an
altitude as possible. As advances are made in transmitter
design, antennas, and matching networks, this limit could be
extended. The upper limit was chosen to provide penetration.
It is conceivable that a higher frequency, such as 50 Mc,
might be desirable to obtain a good surface reflection.

### 4. WEIGHT, SIZE, AND POWER

Constraints are usually established by the specific
mission. As spacecraft payload capability increases with the
introduction of higher propulsive rockets, these constraints
may ease considerably. For presently conceived missions,
upper limits of 25 pounds in weight, 1 cubic foot in volume,
and 15 watts average power were specified.

### 5 ORBITAL ASPECTS

Doppler shift and range to the planet are the impor-
tant orbital aspects. The missions include flybys as well as
orbiters. Orbiters may be in elliptic or circular orbits.
Due to energy limitations, flybys were approximated as para-
bolic orbits about the planets. There would be no doppler
requirement for circular orbits and the largest doppler shift
could occur in a parabolic orbit for a given latus rectum.
Thus, the maximum doppler shift will depend on the nearest

14

approach to the planet. The closer the approach in a parabolic orbit, the larger the doppler shift. For a miss distance of 1000 km from the surface, the maximum possible radial velocity, which occurs for the 90 or 270 degree true anomaly, would be about 2.25 km/sec for Mars, or a doppler shift of 15 cps at 1 Mc or 150 cps at 10 Mc. For Venus, the corresponding quantities are 6 km/sec and 40 cps at 1 Mc or 400 cps at 10 Mc. Since this is an extreme case, the doppler shifts are expected to be less. Thus, a flyby missing by 10,000 km from the surface of Mars would cause doppler shifts of about 9 cps at 1 Mc and 90 cps at 10 Mc. An eccentric orbiter about Mars with a periapsis of 1000 km and an apoapsis of 40,000 km would result in a doppler shift of 12.5 and 125 cps at 1 and 10 Mc, respectively.

The maximum range affects the extent of the orbital coverage. If the apoapsis of an elliptical orbit is beyond the maximum range, then sounding will occur from the periapsis to the maximum equipment range. In a flyby there will be two points in the orbit beyond which the range exceeds the equipment capability. These points will limit the range of sounding or the angular extent of the true anomaly within which sounding occurs.

Another important parameter is time in orbit. When far out, the angular velocity is very small and the time for sounding is increased. This extra time may be of considerable help in providing sufficient integration time. When close, power is not limited and the faster angular rate and reduced time per sounding is compensated. For the highly elliptical orbit described, the near angular rate is about $10^{-3}$ rad/sec and the far rate is about $3.5 \times 10^{-5}$ rad/sec. This is a ratio of about 30 to 1, indicating that the time available is about 30 times as great for sounding with the same horizontal resolution at 40,000 km as at 1000 km.

Consideration must also be given for planetary rotation during sounding periods as well, particularly for Mars.

## C.  REVIEW OF SOUNDING TECHNIQUES

Since the advent of the space era, various techniques have been used to measure the Earth's upper ionosphere. Prominent among them are the pulse sounding or time delay measuring technique, the differential doppler shift method, the polarization change measurement, and the incoherent scatter radar. These techniques will be discussed relative to planetary sounding.

The various time delay sounding techniques radiate medium- and high-frequency waves and measure either echo time delay, phase shift, or frequency shift interpreted in terms of the electron density profile. The measurement of the time delay of pulse echoes is a technique that has been used on board space vehicles. Both the doppler shift and polarization measurements use a cooperative ground station and a space vehicle. In a vertical trajectory, it provides profile information. In a satellite, it provides the path-integrated electron density. Frequencies above the ionospheric cutoff are used since penetration is necessary and the simplifications at higher frequencies (100 Mc, for example) are required for easier interpretation of the data. The polarization change requires a magnetic field, since the integrand involves the magnetic field strength as a proportional factor. The doppler shift method, however, does not depend on a magnetic field. Incoherent scatter has been used as a ground radar facility and has not been placed aboard a space vehicle as yet. It is a more powerful technique in that it can provide temperature and some constituent data as well.

During the program these techniques were reviewed for application to the planetary sounder. It was found that

only the time-delay type of sounder would be suitable for the period of the presently programmed missions, although it is conceivable that future developments may yield other suitable methods. As a result, the bulk of the techniques effort described in Section 3 is devoted to system techniques for time-delay measurements. The reasoning that leads to this is described in this section.

## 1. DOPPLER SHIFT AND POLARIZATION CHANGES

Except for analytical differences resulting from the inclusion of a magnetic field, both relative doppler shift and polarization change for higher frequencies depend on the same path length integral. The doppler technique does not provide the desired information in the absence of a cooperative ground station unless it is placed in a prescribed elliptic orbit and signals are bounced off the planet. The uncertainties in accomplishing such orbits dictates against this method. When space missions have been advanced to the point where a suitable receiver or transmitter can be placed on Mars or Venus, a doppler experiment may be more desirable.

If a magnetic field is present, however, signals at high enough frequencies bounced off the planetary surface will contain polarization information which will result from two passes through the ionosphere. This type of experiment would be similar to the moon bounce measurements made from Earth. It requires an orthogonal set of receiving antennas with either spacecraft orientation information or an oriented vehicle. If the spacecraft is within a significant part of the ionosphere, small changes in spacecraft altitude produce significant changes in polarization, since the two component waves are traveling at different velocities. If the spacecraft is outside the ionosphere, then changes in altitude

are not significant since the component waves are traveling at the same velocity in this region. Assuming a known orientation and the presence of a magnetic field, the experiment is feasible if the spacecraft is out of the ionosphere. The information obtained is the integral of the product of the vertical component of the magnetic field and the electron density along the vertical propagation path. Unless the magnetic field is known, the electron density cannot be readily extracted.

The polarization experiment was not considered further for several reasons. First, it requires a magnetic field and knowledge of the magnetic field which is difficult to obtain without the help of an independent experiment. Second, it can be accomplished by modifying a time-delay type of experiment. A planetary sounder should sense the planet and locate it relative to the ionosphere. Thus, a comprehensive sounder will include the radiation of some penetrating frequency. Adaptation to polarization measurements requires an extra receiver on an orthogonal antenna. Third, it provides, at best, integrated electron density, which would be most useful to have if it were in addition to profile information. Consequently, it was considered a supplementary experiment, or an experiment to be recommended in the event there are severe antenna, weight, and power constraints which would necessitate the sacrifice of a more elaborate arrangement to measure the vertical profile.

Doppler shift, on the other hand, requires a path length that changes with time. Aside from a highly elliptical orbit, vertically bouncing signals off the planetary surface will result in very slow changes in path lengths, since the horizontal gradients generally can be assumed to be small compared with the vertical gradients. At best then, horizontal gradient information is obtained. Again this would

18

be a supplementary type of experiment, the prime interest being the vertical profile which is not obtained by doppler shift even in the integrated form. Time-delay soundings taken along a trajectory can provide such information as well as the vertical profile. The same consideration applies to doppler measurements at frequencies which reflect from the ionosphere. In an elliptical orbit, the path length change is primarily a local ionization measurement, and a suitable orbit may be difficult to accomplish.

The principle use for doppler shift is for measuring the spacecraft's radial component of velocity. As such it becomes a subsystem problem that may be important in one or other versions of a time-delay sounding system.

2.    INCOHERENT SCATTER RADAR

This type of system operates at UHF or VHF. It has been very successful as a ground experiment. In a spacecraft there are several difficult problems to encounter. To begin with it requires considerable power, weight, and size. Only the largest spacecraft could be considered capable of carrying it in its present form. The scattered signal is very small. On the ground the ground clutter interferes with the reception of data from the first 150 to 200 km of the radar. The ground reflection in a spacecraft would be very strong compared with the scattered signal. Unless care were taken to avoid receiver blocking, the small backscattered signal could be lost. Ground reflections could also be picked up by antenna side lobes. On the ground large antenna structures are used. At 400 Mc, both 85- and 200-foot antenna dishes are required. A large antenna structure would be needed for a spacecraft as well. Considerable time can be taken to integrate the weak backscattered signal in a ground installation. The extent of equipment required in a spacecraft may not be feasible, and there may not be sufficient

time since the spacecraft is not stationary. Extremely low noise receivers also would be required in a spacecraft. We are presently on the forefront of using such equipment in Earth satellites. To use such equipment in a planetary mission is premature at present.

Backscatter techniques may eventually be adaptable to space use. For the present, it was considered well beyond the state of the art and was not considered further.

# SECTION 3
## SOUNDING TECHNIQUES STUDY

## A. INTRODUCTION

The scientific objectives set forth in the previous sections for a mission to Mars or Venus can be accomplished using techniques which have proven successful in our observations of the Earth's ionosphere. Radars operating in the high- and medium-frequency region have long provided vertical bottomside soundings and, more recently, topside soundings from satellites to establish electron density profiles. Although the method is well established, the application to planetary flights becomes difficult due to limited available power, high cosmic noise levels, and far greater distance variations over which the sounding equipment must operate.

The purpose of the techniques study was to provide the parametric relationships and systems approach which may be used in determining the requirements and specification for a Mars or Venus mission. This parametric study will also be helpful for other planetary missions.

### 1. OBJECTIVES

The object of the techniques study is to provide a useful set of data in parametric form from which a concise estimate of all requirements and specifications for a planetary mission to Mars or Venus might be drawn.

The study includes the relationship of miss distance or orbital height, power, resolution, antenna requirements, and frequency, and the particular constraints imposed by a specific mission. The various types of modulation and advantages and disadvantages of each are considered. The applica-

tion of the data to assumed specific missions is given, as
well as recommendations for a system applicable to the
requirements currently anticipated for an early mission to
Mars.

2.    CONDITIONS

The following conditions have been imposed for this
study:

1.    Multiple ionospheric echoes are expected
      to be observed and must be resolved.

2.    The planet's ionosphere has specular
      properties and minimal diffusion of return
      echoes will occur.

3.    The latest and best known values of cosmic
      noise level should be used.

4.    The spacecraft orientation to the planet
      will be known, as determined by suitable
      sensors.

5.    Provisions can be made to equip the space-
      craft with at least one set (or preferably
      two sets) of erectable dipole antennas which
      will be oriented parallel to the planet's
      surface.

3.    RANGE OF PARAMETERS

The range of parameters for general use in this
study will attempt to cover the most probable applications
for present or future use.  In most cases, the parameter
relationships can be presented in a form that readily per-
mits extrapolation beyond the study limits.  Data will be
presented in a form suitable for technique comparison using
parameter cross-reference where possible.  The following
parameter limits have been established:

| | |
|---|---|
| Distance | 1000 to 100,000 km |
| Resolution | 1 to 100 km |
| Frequency range | 0.5 to 20 Mc |

|             |                     |
|-------------|---------------------|
| Primary power | 15 watts maximum   |
| Weight        | 25 pounds maximum  |
| Size          | 1 cubic foot maximum |

4. TYPES OF MODULATION

The methods of modulation considered in this study can be generalized under three basic types: pulse (amplitude), phase, or frequency.

All other modulation types can be considered as special cases of these basic types. To convey a given amount of information per period of time from a transmitter to a receiver uniquely determines the bandwidth requirements independent of modulation method. Likewise, the energy required to convey this information is independent of modulation. The system complexity can be affected by the choice of modulation method; however, basic limitations normally existing in each method require tradeoff considerations for each specific system.

B. GENERAL PARAMETERS

The techniques study can be divided into general and specific parameter portions. The general portion will cover those characteristics which are basic to any system regardless of type of modulation or signal improvement techniques. The following paragraphs cover the general aspects.

1. RECEIVED POWER

The classical radar equation gives a received power $P_R$, which is inversely proportional to the fourth power of range R:

$$P_R = \frac{P_T G_T^2 \lambda^2 \sigma}{(4\pi)^3 R^4} \tag{1}$$

This is applicable when the target area is small and intercepts only a small portion of the radiated energy. This condition prevails when sounding a planet from large distances. When the target size becomes large, such as when sounding a planet from low altitudes, a greater portion of the radiated power is intercepted and reflected. Consequently, a more inclusive derivation will be required to cover both aspects.

### a. FLAT-PLANE APPROXIMATION

It is assumed that, below the maximum plasma frequency, the ionosphere would approximate a specular spherical reflector. At small altitudes in comparison to the radius of the sphere, a flat-plane approximation (Figure 2A) may be made. Using Snell's law for reflecting incident rays, the power density (p) seen by the source is that which would be radiated by an image source (S') located at a distance h behind the plane. For a transmitted power $P_T$, and antenna gain equal to unity

$$p = \frac{P_T}{4\pi(2h)^2}$$

The effective area of the receiving isotropic antenna assuming unity gain is $\lambda^2/(4\pi)$. There results a received signal power $P_R$ and a range equation of the form

$$P_R = \frac{P_T \lambda^2}{(4\pi)^2 (2h)^2} \qquad (2)$$

### b. SPECULAR SPHERE

A more exact solution uses the geometry of Figure 2B. Because of the curvature of the sphere, reflected rays diverge considerably more than for the flat-plane approximation. As a

24
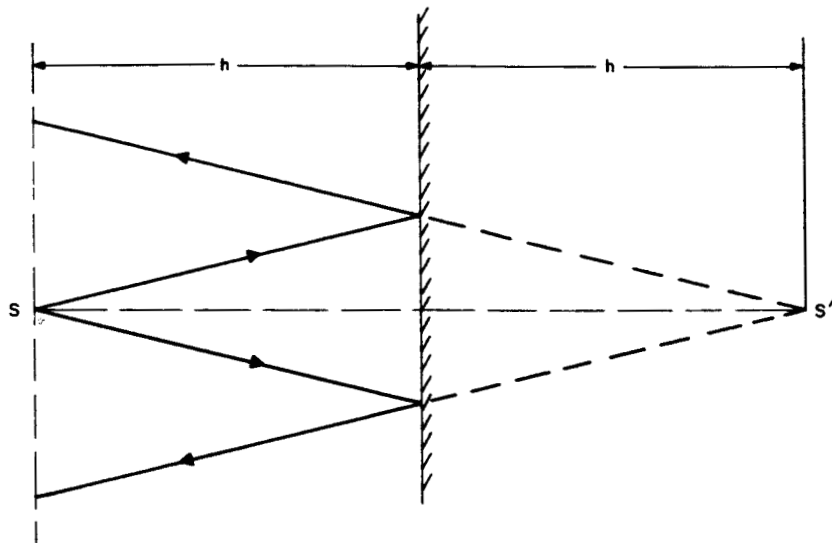
**A. FLAT PLANE APPROXIMATION**
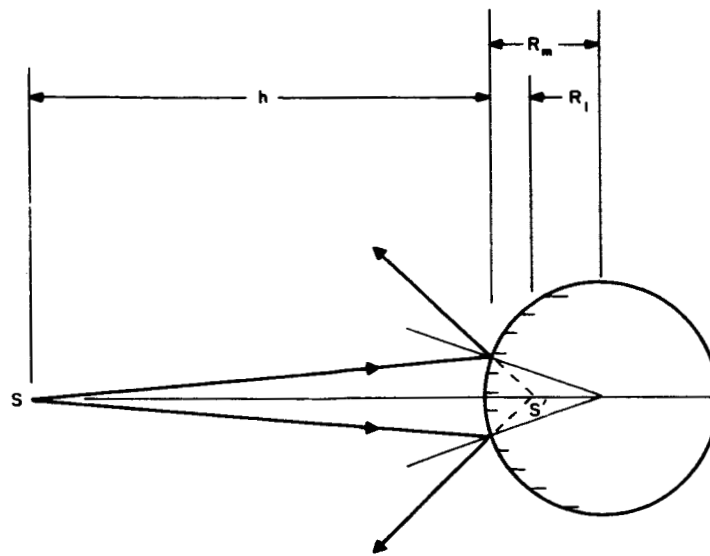


**B. SPHERICAL SURFACE CASE**

FIGURE 2.  FLAT-PLANE AND SPHERICAL CONFIGURATIONS

result, the received power density at S is reduced from the flat-plane case. To determine the power density incident at S, it may be noted that an apparent focus or image antenna appears at S'.

Thus, the power density $p_1$ incident at the sphere due to source S is

$$p_1 = \frac{P_T}{4\pi h^2}$$

The power density $P_2$ due to an image source S' (assumed isotropic) at the surface of the sphere is

$$p_2 = \frac{P_T'}{4\pi R_1^2}$$

Equating this to the above, the equivalent transmitted power of S' is found to be

$$P_T' = P_T \frac{R_1^2}{h^2}$$

Thus, the power density p at S due to image source S' is

$$p = \frac{P_T'}{4\pi(h + R_1)^2}$$

$$= \frac{P_T R_1^2}{4\pi h^2(h + R_1)^2}$$

Assuming an isotropic antenna of area $\lambda^2/(4\pi)$, the power intercepted by a receiver at S due to image source S$'$ is

$$P_R = \frac{P_T \, \lambda^2 \, R_1^2}{(4\pi)^2 \, h^2 (h + R_1)^2} \qquad (3)$$

To find the apparent focus $(R_1)$, the laws of geometrical optics may be applied. The relation for refraction at a spherical surface is:

$$\frac{n}{s} + \frac{n'}{s'} = \frac{n' - n}{R}$$

where

  n and n$'$ = respective indices of refraction,
  s and s$'$ = respective distances to the source and apparent source,
    R = radius of the sphere.

For a reflective surface, n$'$ = -n, and n becomes an arbitrary constant. The relationship becomes

$$\frac{1}{s} - \frac{1}{s'} = -\frac{2}{R}$$

or for this case

$$\frac{1}{h} - \frac{1}{R_1} = -\frac{2}{R_m}$$

Hence,

$$R_1 = \frac{R_m h}{R_m + 2h}$$

Substituting the above into the equation for received power yields

$$P_R = \frac{P_T \lambda^2}{(4\pi)^2 (2h)^2} \times \left[ \frac{R_m}{R_m + h} \right]^2 \qquad (4)$$

It can be seen that the first portion of the equation is the flat plane approximation. The quantity $(R_m/R_m + h)^2$ is the result of the spherical surface and will be referred to as the defocusing loss. As the distance from the surface becomes very large, this equation approaches the radar equation with an inverse fourth power variation with distance.

Figure 3 shows the flat-plane approximation of the received power versus distance as a function of frequency for a transmitted power of one watt. This is the path loss independent of planet characteristics. Separate curves show the defocusing loss versus distance for each planet.

2.  COSMIC NOISE

The average cosmic noise level in the medium- and high-frequency regions in interplanetary space is still subject to extensive measurements by experimenters. Many rocket experiments have been conducted which provide an indication of the equivalent brightness factor that may be anticipated. Figure 4 shows a range of results above 1 Mc. For this study, the results of NASA Flight 8.33 will be used since they indicate the latest and possibly most accurate data thus far obtained. Also, since the brightness level obtained during this flight is higher than the norm in the applicable frequency range, it will ultimately provide a slightly more pessimistic indication of received signal-to-noise ratio (S/N), which is to be preferred in this type of study.
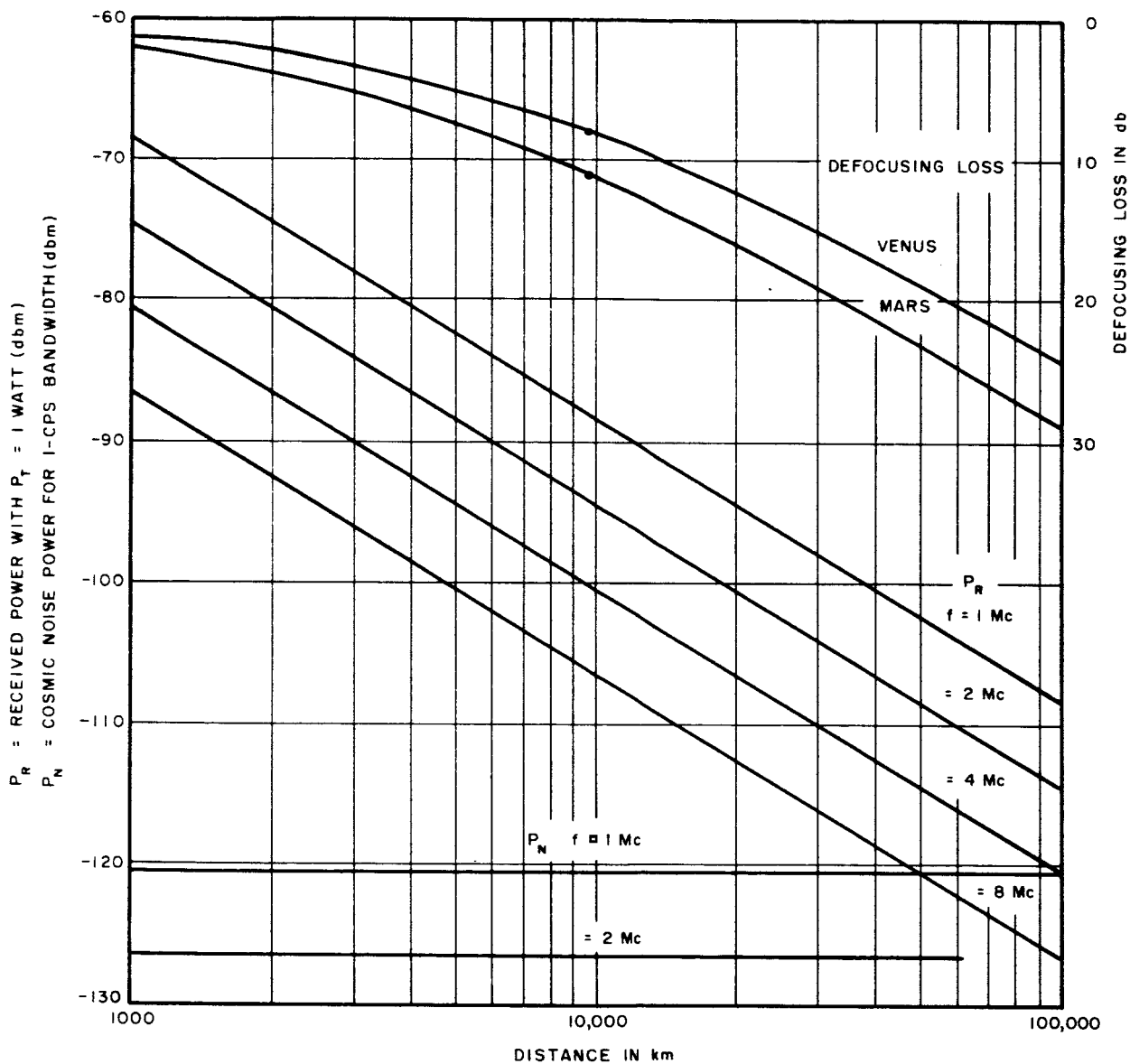
FIGURE 3. RECEIVED POWER VS DISTANCE AS A FUNCTION OF
FREQUENCY
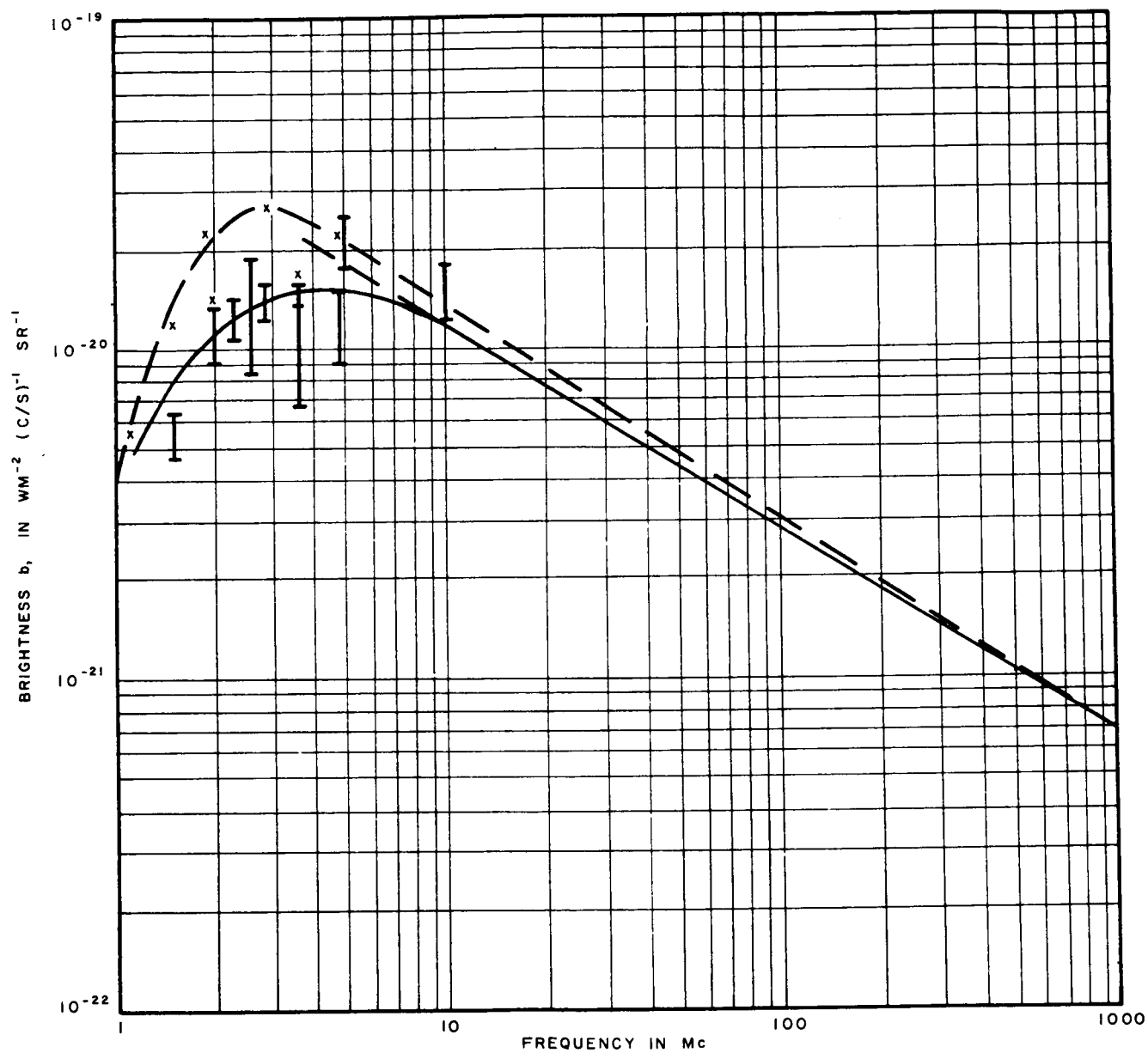
FIGURE 4.  COSMIC NOISE LEVEL ABOVE 1 Mc

The brightness factor (b) is expressed as

$$\frac{\text{watts}}{m^2} \times \frac{1}{\text{cps}} \quad \frac{1}{\text{steradian}}$$

Equivalent noise power is obtained by multiplying by $4\pi$ and the effective antenna area. The resulting expression is in watts/cps. An equivalent temperature (T) may be obtained by equating the above to KTB, where B is the bandwidth and K is Boltzmann's constant. If an average value of brightness factor (b) is chosen, and this is assumed to be constant with frequency, a simplification of the data presentation results. Figure 5 shows the cosmic noise power ($P_{cn}$) versus frequency for an assumed constant value of $b = 2 \times 10^{-20}$ wm$^{-2}$(c/s)$^{-1}$ sr$^{-1}$ and the actual brightness factor. For a frequency range of 1.5 to 10 Mc, a maximum error of 1.5 db results. The cosmic noise power is related to the brightness factor b by:

$$P_{cn} = \frac{\lambda^2}{8\pi} \times 4\pi \times b \tag{5}$$

Therefore, using the constant value of b allows a reduction of cosmic noise power with increasing frequency of 6 db/octave. Since the path loss rises with increasing frequency at a 6 db/octave rate there results an S/N that is independent of frequency over a major portion of the frequency range of interest from 1.5 to 10 Mc.

Figure 6 shows the actual improvement in S/N between 1.0 and 1.8 Mc. With the linear approximation, an analysis independent of frequency can be made with corrections needed only at the lower frequencies and highest frequencies.
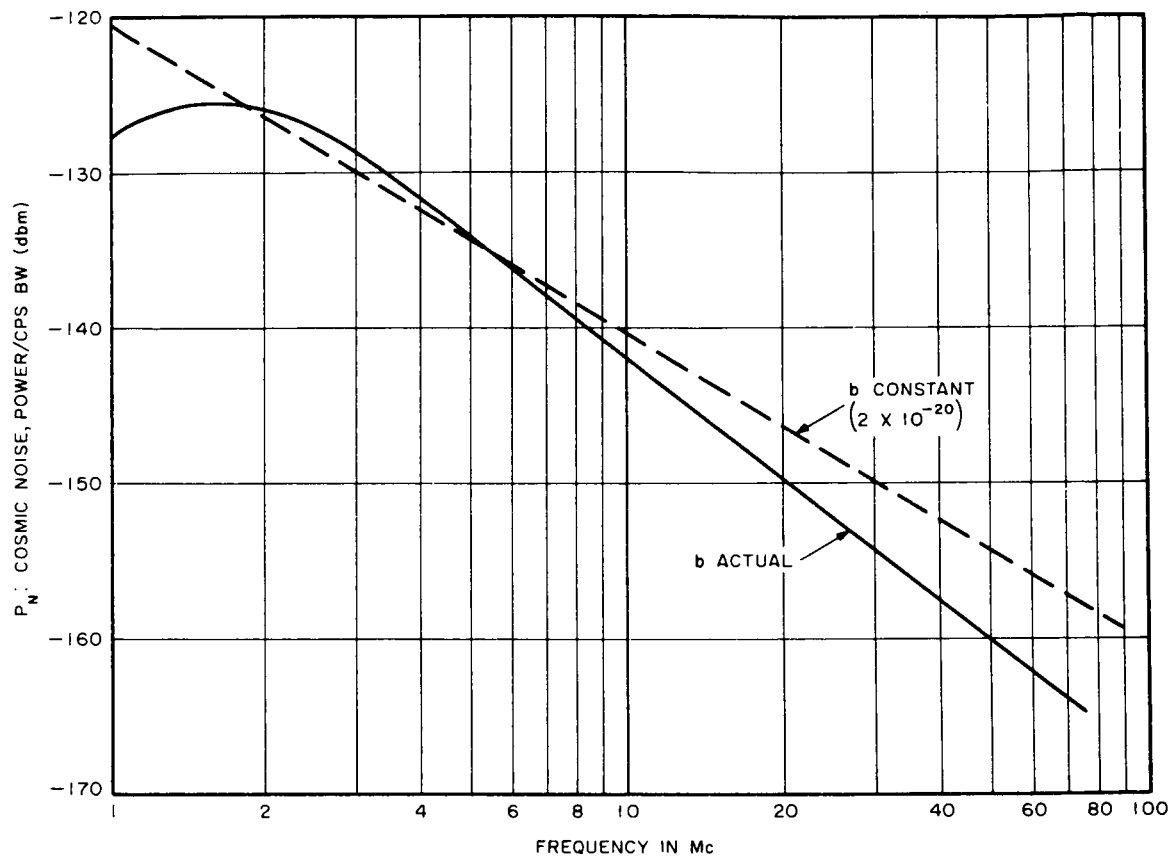
FIGURE 5.  COSMIC NOISE POWER VS FREQUENCY
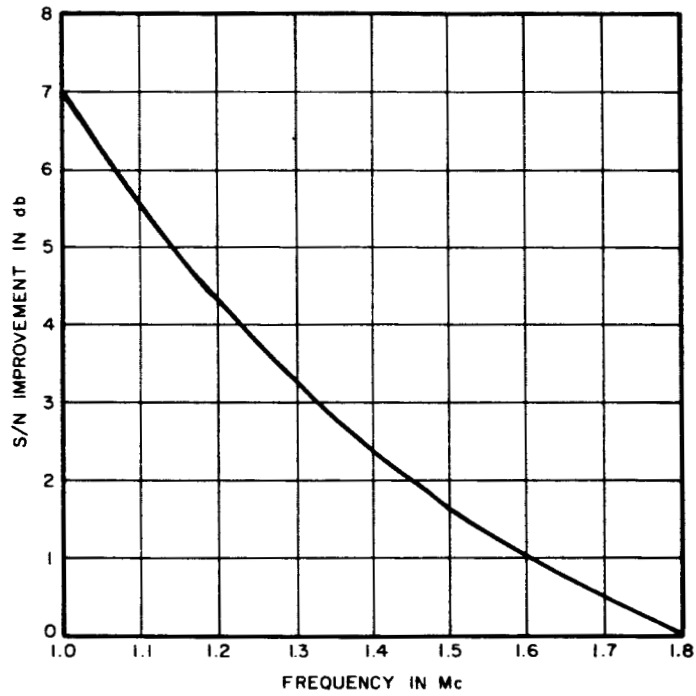
FIGURE 6.    IMPROVED S/N WITH DECREASE IN COSMIC NOISE POWER

## 3. REQUIRED ENERGY

From the relationship established for the received power from a specular sphere and the cosmic noise power, the conditions can be obtained for system operation.

The ratio of received signal power ($P_R$) to noise power ($P_N$) becomes:

$$\frac{P_R}{P_N} = \frac{P_T \lambda^2}{(4\pi)^2 (2h)^2} \times \left(\frac{R_m}{R_m + h}\right)^2 \times \frac{1}{KTB} \qquad (6)$$

Defining the total transmitted energy as:

$$E_T = \frac{P_T}{B} = P_T \tau \qquad (7)$$

and adding fixed losses due to mode splitting and circular polarization of the return signal, equation 6 becomes:

$$\frac{P_R}{P_N} = E_T \frac{\lambda^2}{(8\pi h)^2} \times \left(\frac{R_m}{R_m + h}\right)^2 \times \frac{L}{KT}, \qquad (8)$$

where L is the fixed losses. It will be assumed that the antenna gain is unity at this time. Also, the loss due to antenna matching will be considered separately for simplification, since it is a function of antenna length.

If $P_R/P_N$ is set equal to a required detection threshold level, the required total transmitted energy can be determined by rearranging terms:

$$E_T = \left(\frac{8\pi h}{\lambda}\right)^2 \times \left(\frac{R_m + h}{R_m}\right)^2 \times \frac{KT}{L} \times \frac{P_R}{P_N}. \qquad (9)$$

34

This required total transmitted energy is the average transmitted power times the transmission time (or the coherent integration time upon reception). The relationship is shown in Figure 7 for a 12.5 db threshold.

4. EFFECT OF RESOLUTION ON BANDWIDTH

The desired resolution determines the required information bandwidth. The round-trip time for the modulation signal to traverse one resolution element ΔR is:

$$\tau = \frac{2\Delta R}{c} \qquad (10)$$

where c is the velocity of light. The required information bandwidth B, which will faithfully reproduce this time function is:

$$B \geq \frac{1}{\tau} = \frac{c}{2\Delta R}. \qquad (11)$$

As the bandwidth is opened to allow greater resolution, more cosmic noise enters the receiver causing a degradation of the received signal information. The relationship of resolution, bandwidth, and equivalent signal loss relative to a 1-cps bandwidth is shown in Figure 8.

5. ANTENNA MATCHING

It was assumed for this study that dipole antennas would be used, since they represent the most adaptable, reliable, and easily erectable antenna structure presently available. For the wavelengths of interest, the more optimum antenna poles are mechanically very long but electrically very short. At the longer wavelengths, the antenna pole impedance can normally be represented by a very small radiation resistance in series with a large capacitive reactance. This combination is shunted by the pole-base capacitance.
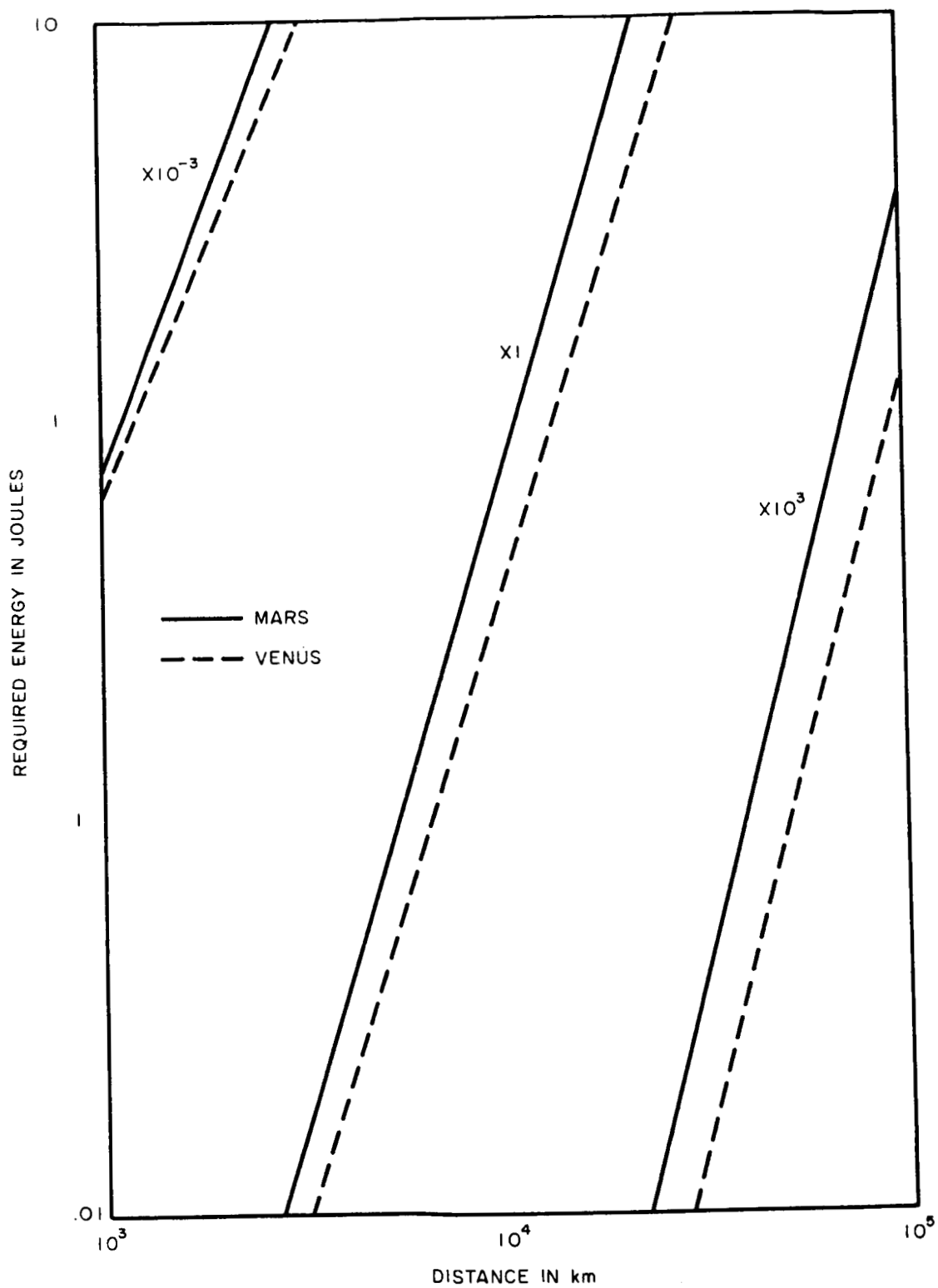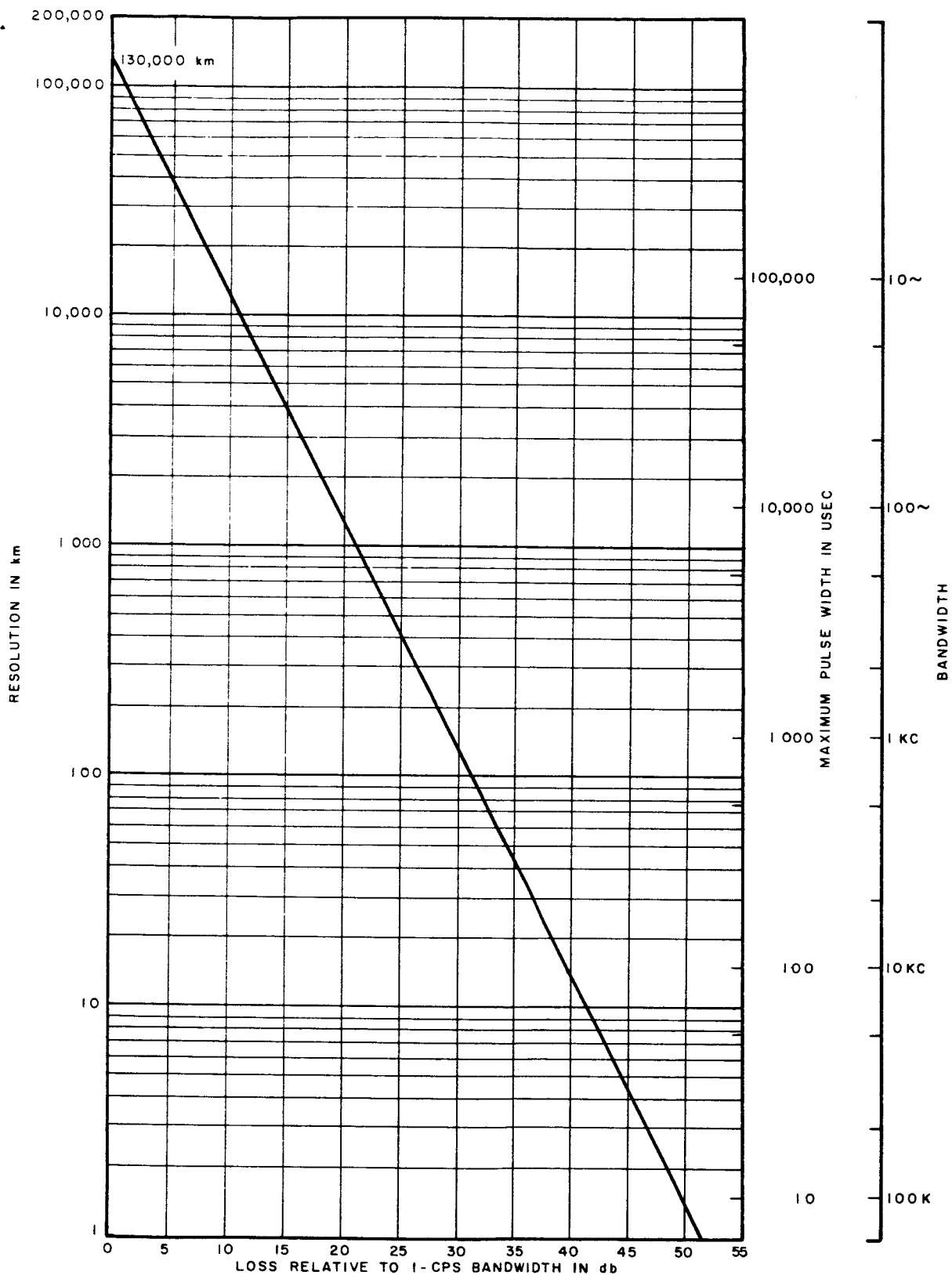
FIGURE 7. REQUIRED ENERGY

FIGURE 8.   RESOLUTION AND BANDWIDTH VS SIGNAL LOSS

The transmitter and receiver must be a conjugate impedance match to the equivalent antenna impedance to minimize losses. Since accurate values of this equivalent impedance were not available, a computer program was established and data obtained of monopole impedance versus frequency for various pole lengths including the effect of the nominal base capacitance. These data are shown in Figures 9 through 14. Assuming the major matching loss to be the result of the finite Q of the matching coils, the computer data was used to determine the antenna matching network loss for coil Q's of 100 and 200. These losses versus frequency for several monopole lengths are shown in Figures 15 and 16, respectively.

## C.   TYPES OF MODULATION

Three basic types of modulation have been considered in this study: pulse, phase, and frequency modulation. Various combinations of these basic types can and have been used in many varied applications to obtain complex modulations. The specific application normally dictates the requirements for these complex types.

The obvious need for modulation is to apply information to a carrier so as to convey intelligence of some form between transmitter and receiver. The system bandwidth determines the rate at which this transfer takes place, and the energy involved in the transfer determines the propagating distance which may exist between transmitter and receiver. These principles apply independently of type of modulation. Usually phase and frequency modulation are applied because they spread the bandwidth, resulting in S/N improvements over amplitude modulation. However, good S/N are required before detection for such improvements. In radar, the transmitted signal is known and optimum approaches are based on filter designs which are related to this signal. This is different from communications in which a large number of signals may be

38
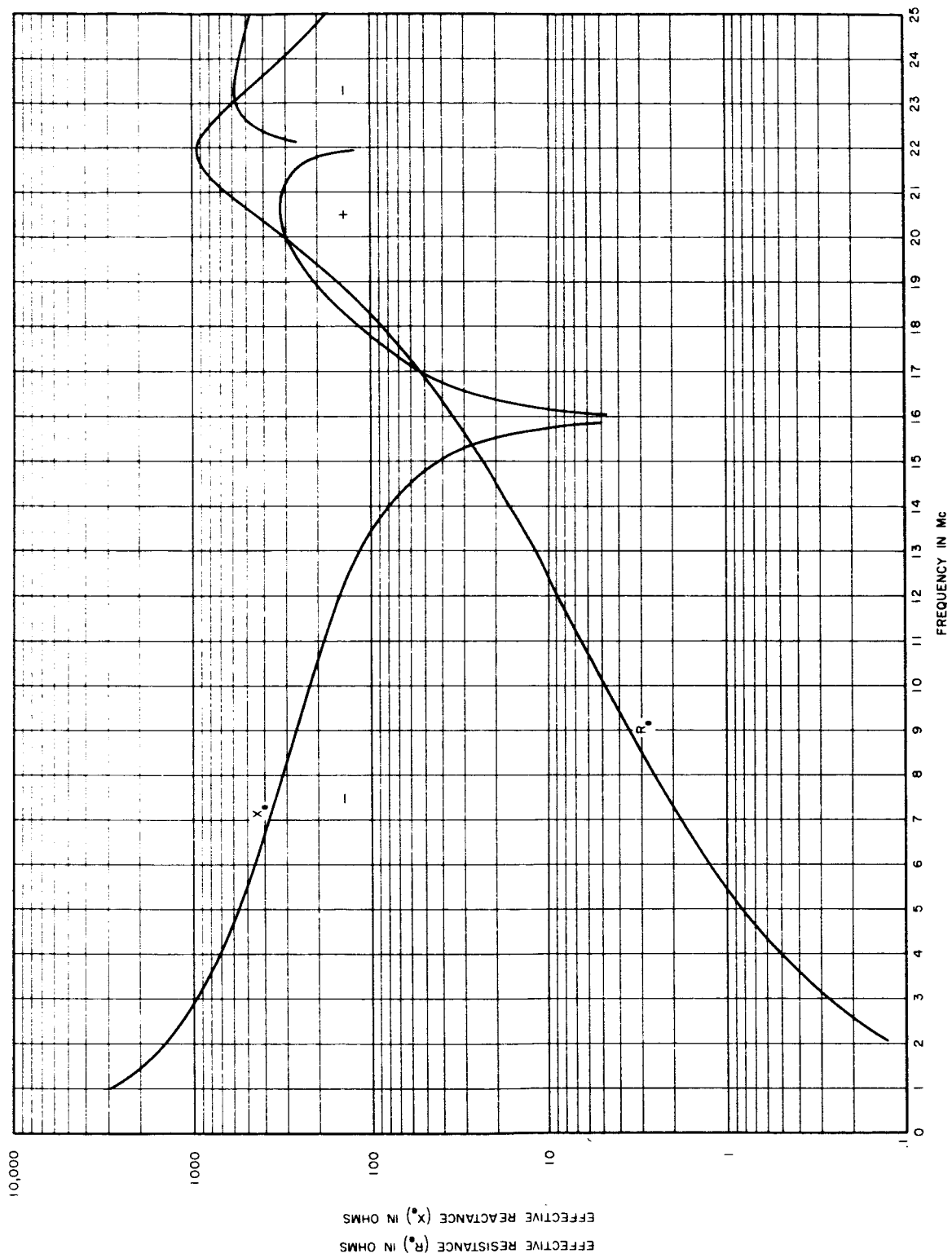
FIGURE 9. MONOPOLE ANTENNA IMPEDANCE (15 FOOT)

EFFECTIVE REACTANCE $(X_e)$ IN OHMS

EFFECTIVE RESISTANCE $(R_e)$ IN OHMS

FREQUENCY IN Mc
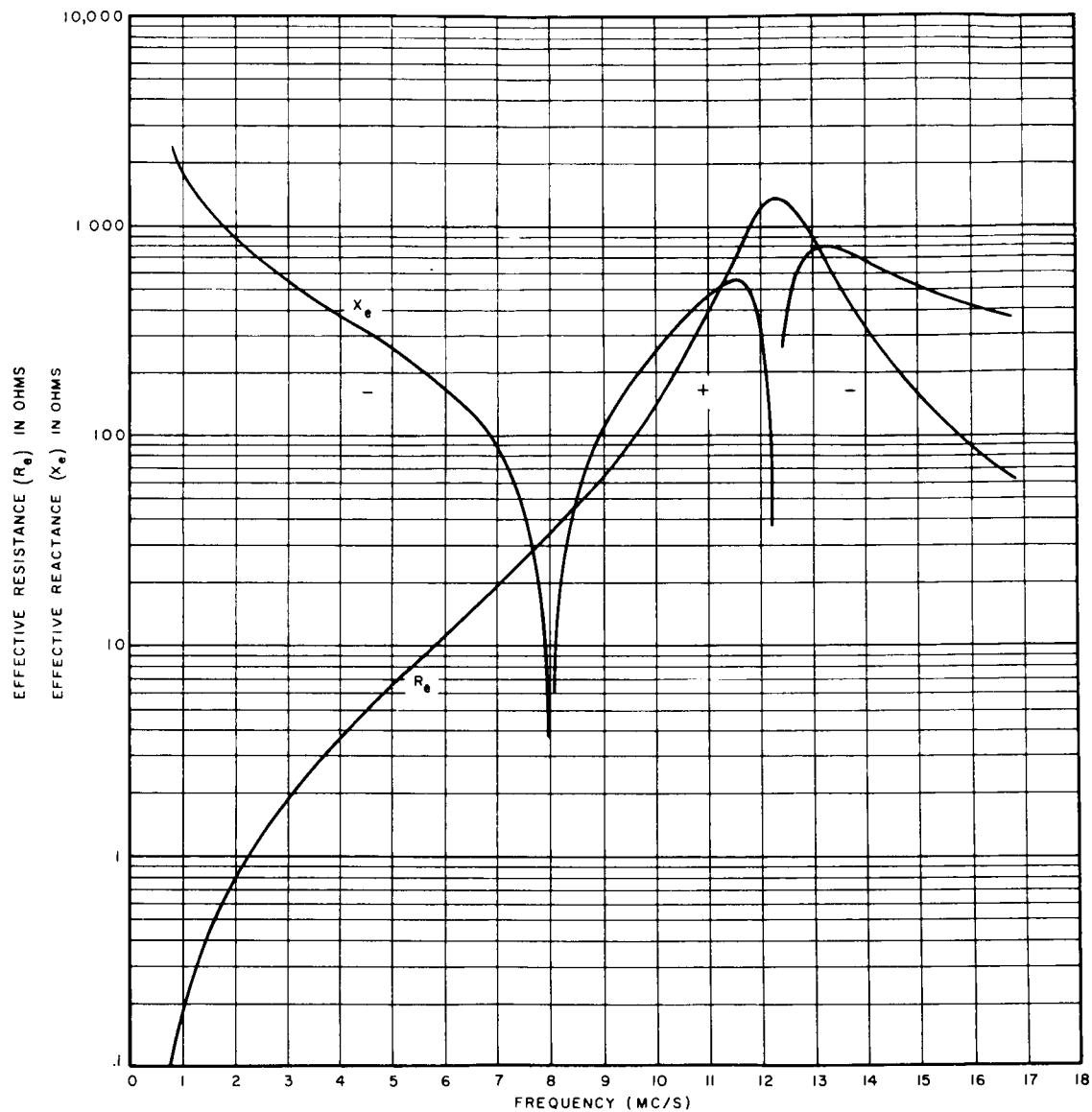
FIGURE 10.   MONOPOLE ANTENNA IMPEDANCE (30 FOOT)
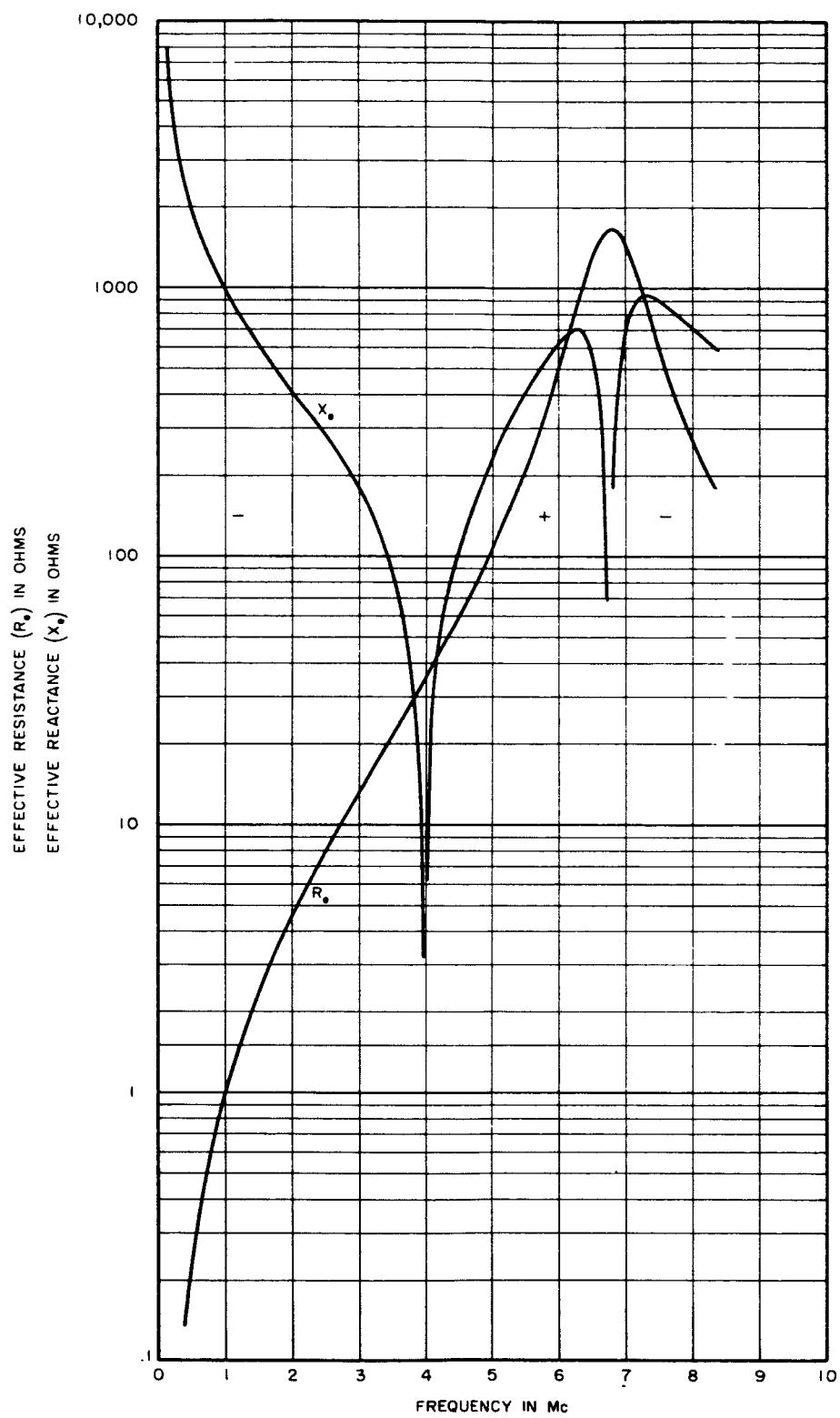
FIGURE 11. MONOPOLE ANTENNA IMPEDANCE (60 FOOT)
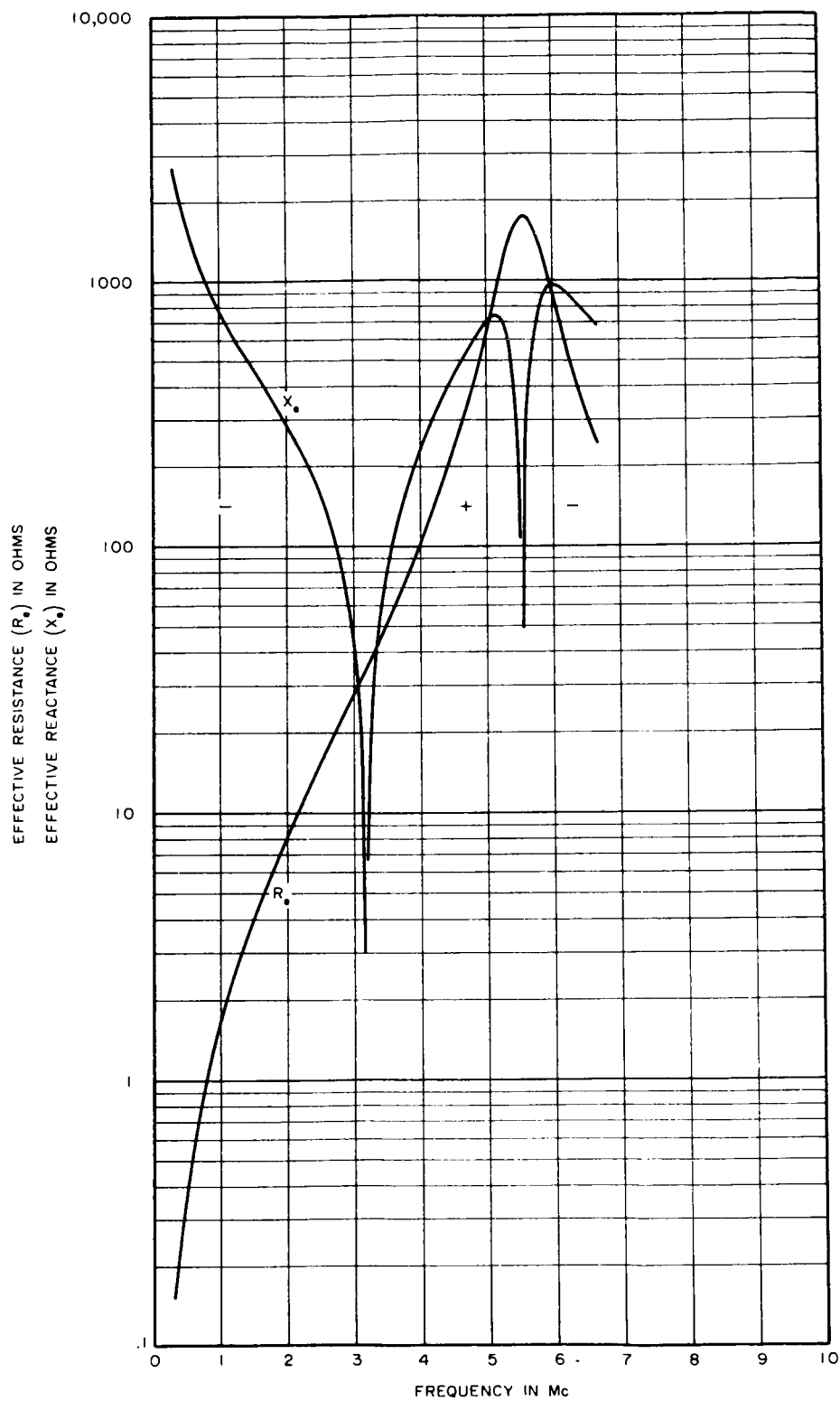
FIGURE 12.  MONOPOLE ANTENNA IMPEDANCE (75 FOOT)
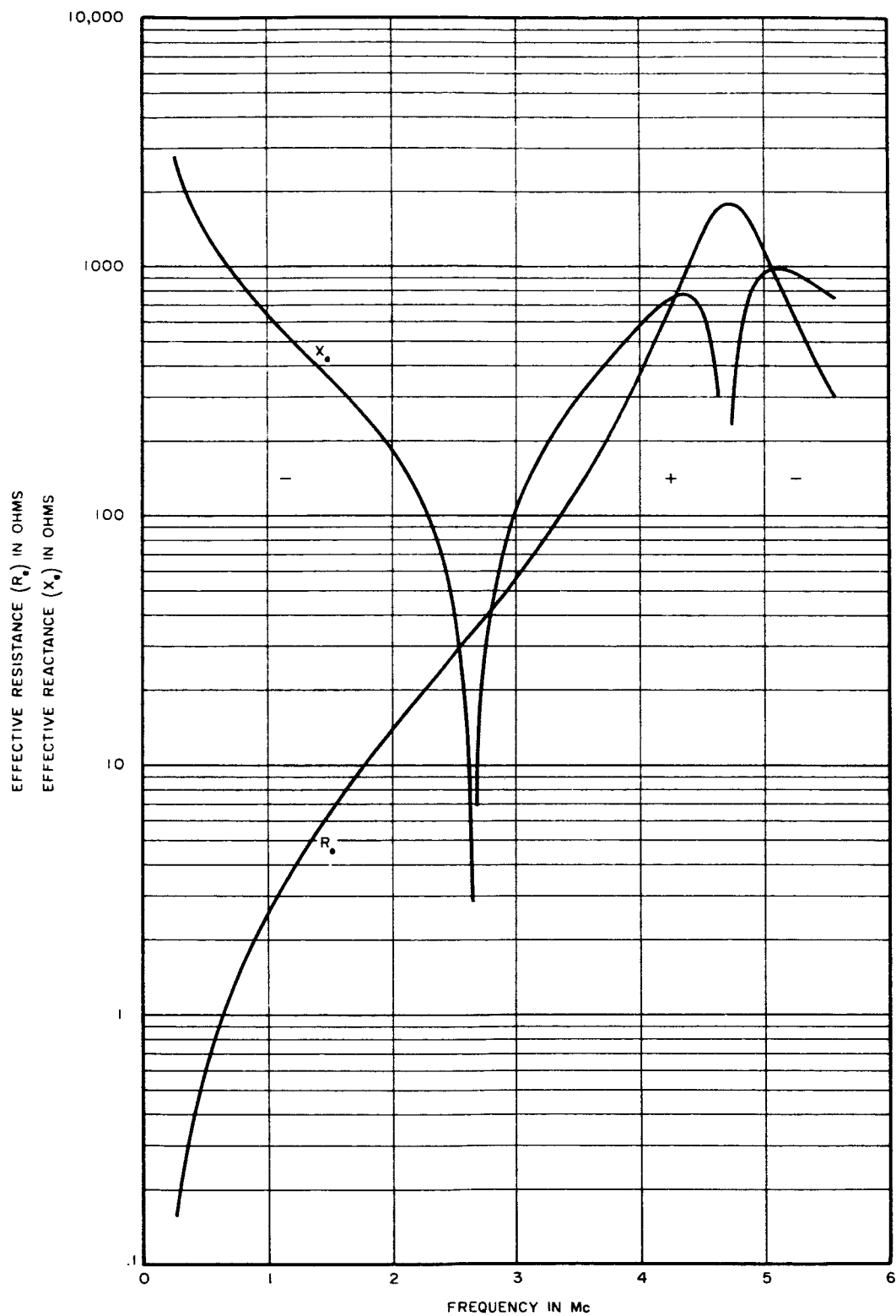
FIGURE 13. MONOPOLE ANTENNA IMPEDANCE (90 FOOT)

43
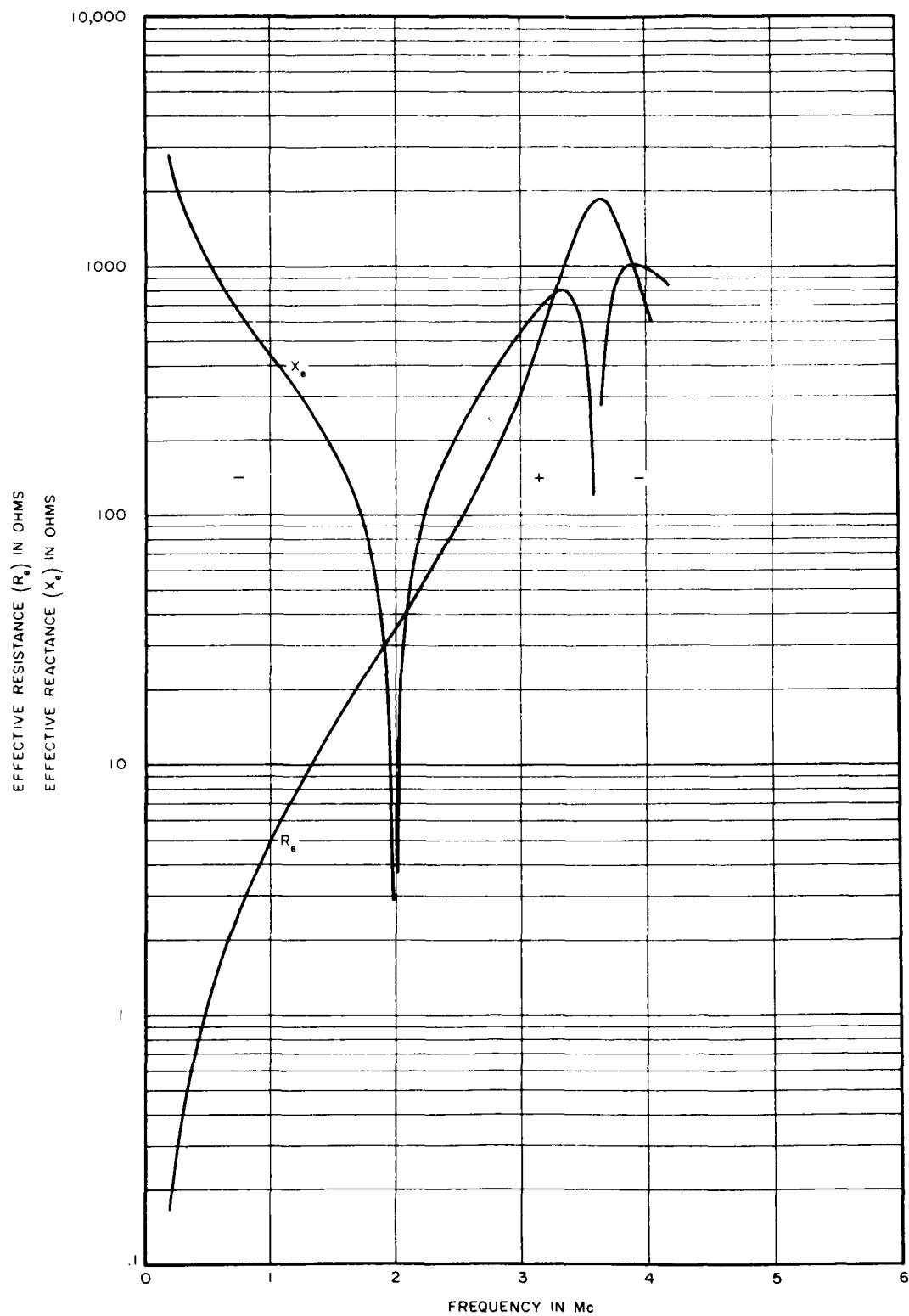
FIGURE 14.   MONOPOLE ANTENNA IMPEDANCE (120 FOOT)
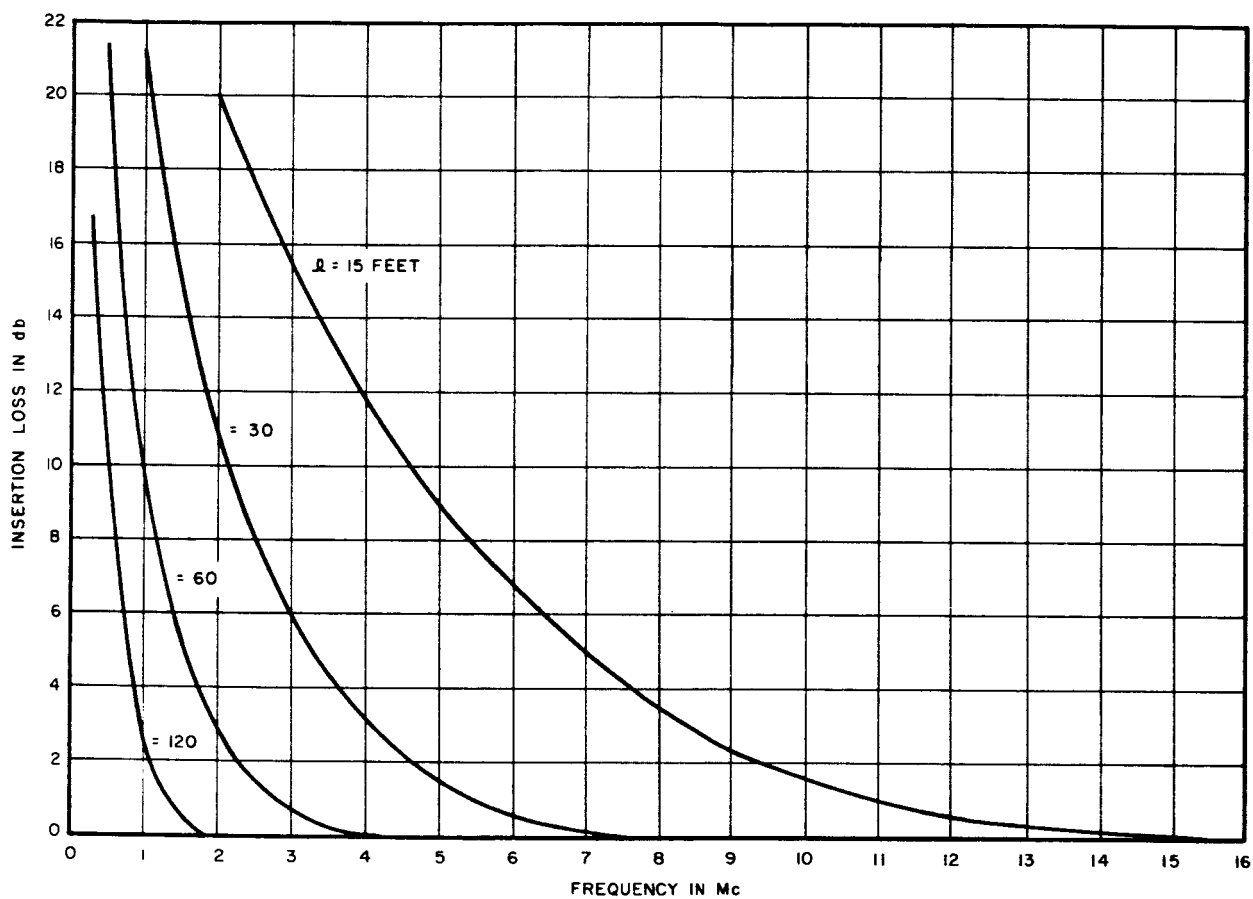
FIGURE 15.   ANTENNA MATCHING NETWORK INSERTION LOSS
            (Q = 100)
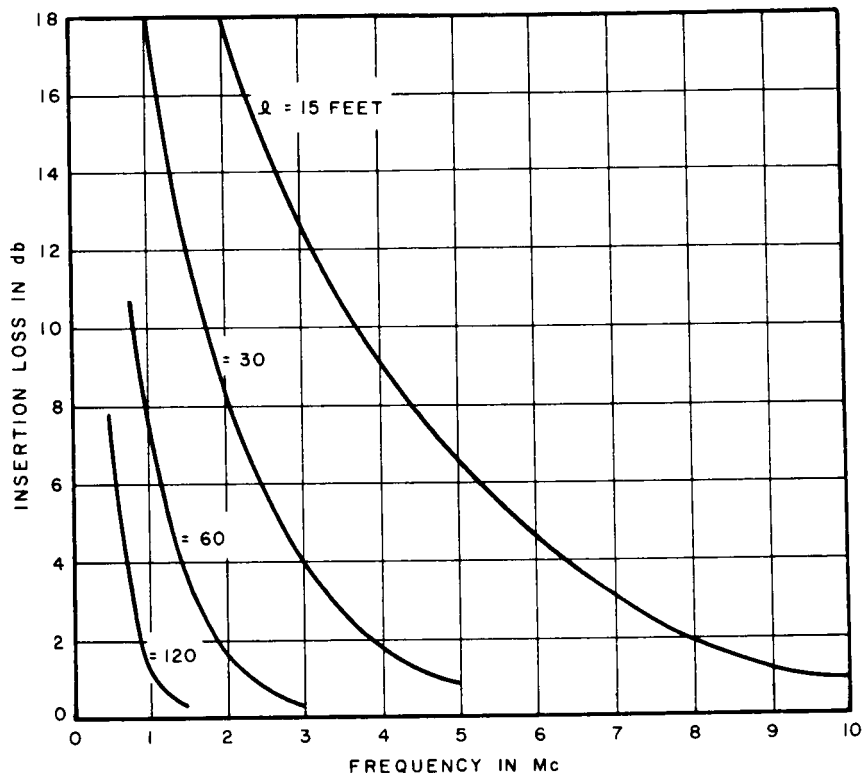
FIGURE 16. ANTENNA MATCHING NETWORK INSERTION LOSS
(Q = 200)

transmitted, and the receiver has little a priori information about the signal.  These matters will be described later in this section.

1.  PULSE MODULATION

The sounder transmits a pulse of time duration ($\tau$) equal to the round-trip time required to cover one resolution element $\Delta R$:

$$\tau = \frac{2\Delta R}{c} \qquad (12)$$

where c is the velocity of light.  If a second pulse is not transmitted until after the return of the first pulse, ambiguity cannot result and the distance (D) to the ionosphere is equal to the round-trip propagation time T:

$$T = \frac{2D}{c} \qquad (13)$$

If multiple mode echoes are spaced in time by an amount greater than the pulse width, they can be resolved.

The parametric relationships for pulse modulation are shown in Figures 17, 18, and 19.

2.  PHASE MODULATION

If a phase-modulated signal is transmitted and a return is obtained after a time T = (2R)/c at the receiver, the transmitted and received modulation signals may be compared in a phase detector to provide an output proportional to their phase difference

$$\Delta\phi = 2\pi f T = 4\pi f \frac{R}{c}$$

where f is the modulating frequency.  The range is therefore
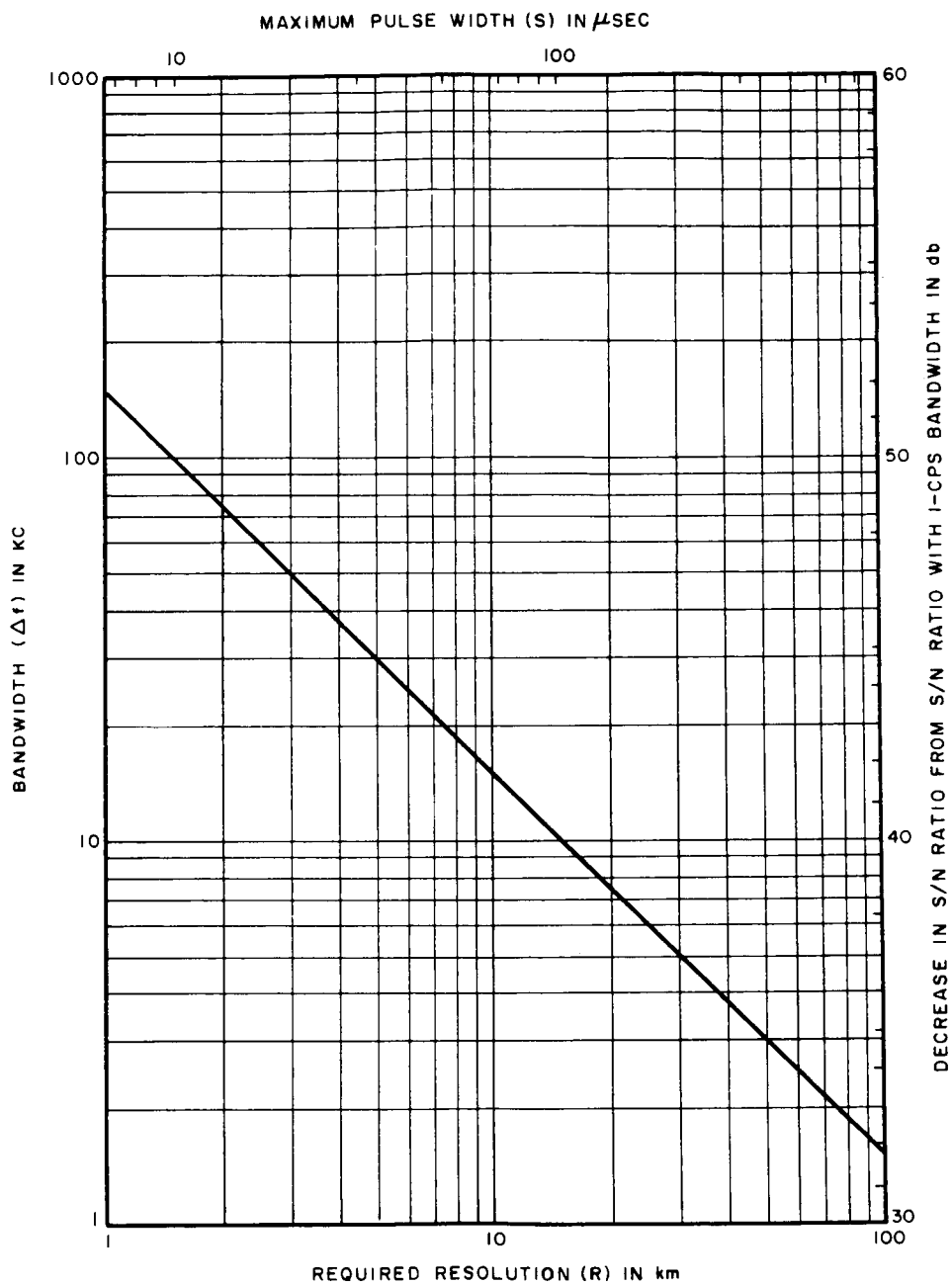
FIGURE 17. BANDWIDTH AND S/N VS RESOLUTION AND PULSE WIDTH
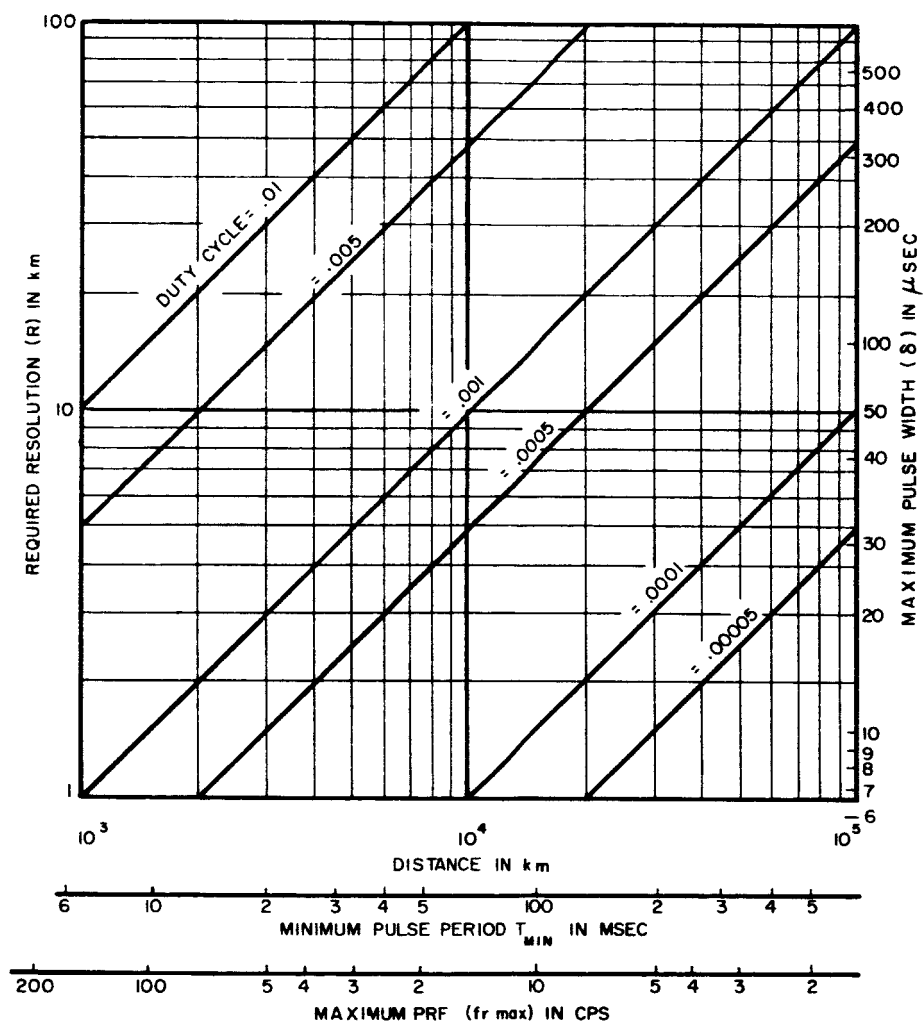
FIGURE 18. RESOLUTION AND PULSE WIDTH VS DISTANCE, PRP, AND PRF
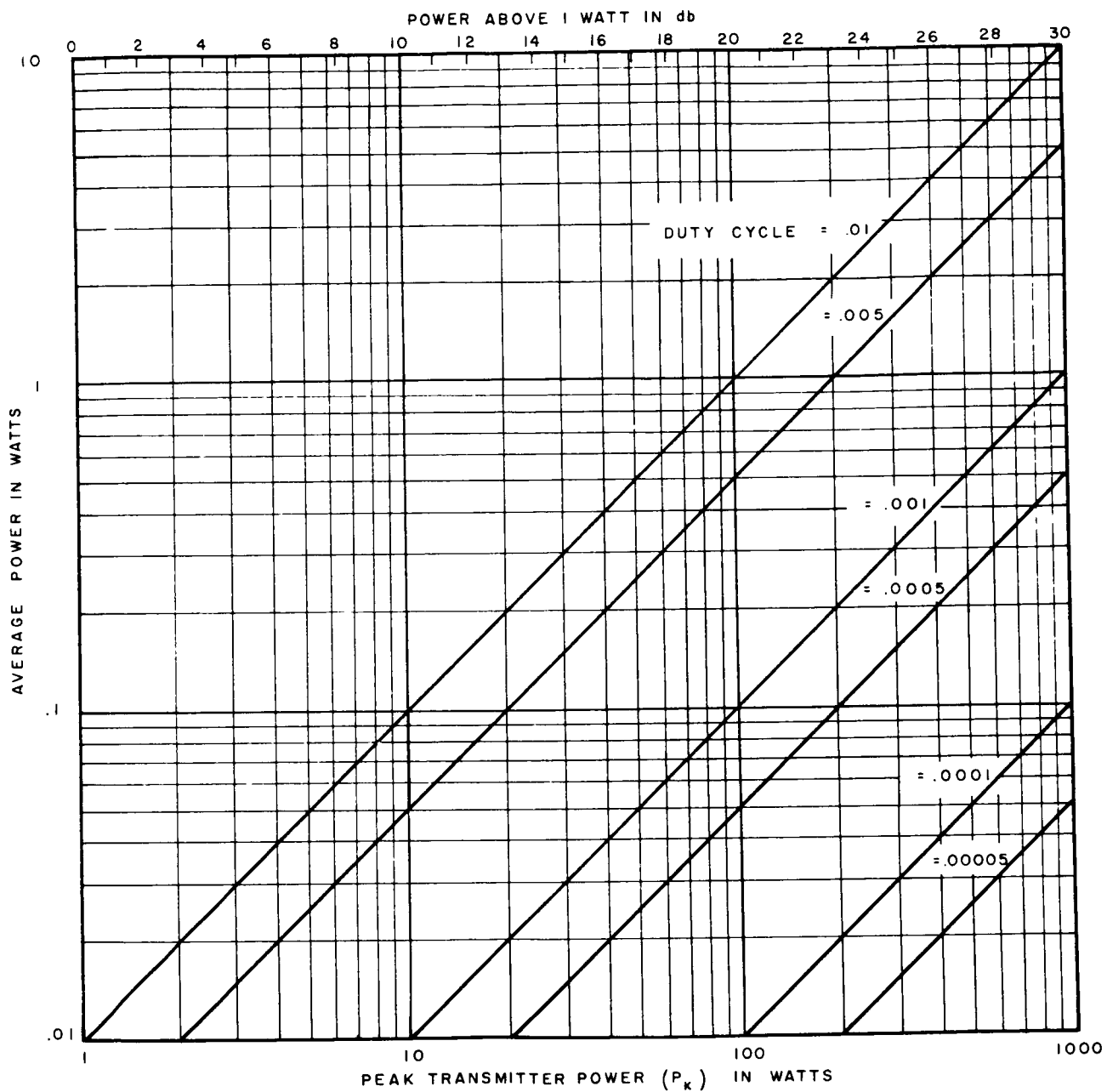
FIGURE 19. AVERAGE VS PEAK POWER

50

$$R = \frac{c\Delta\phi}{4\pi f} \qquad (14)$$

and $\Delta\phi$ is unambiguous only when $\Delta\phi$ is $<2\pi$ radians. The maximum unambiguous range is

$$R_{max} = \frac{c}{2f}. \qquad (15)$$

This type of modulation is acceptable when only a single echo is involved. It has the disadvantage, when multiple echoes return, that the second return may have suffered a phase shift at target reflection so that it would be out of phase with the first return. If the strength of the second return is comparable to the first, almost complete cancellation of the echo could occur. For this reason, phase modulation is not recommended when operating against more than one target and therefore was not considered further in this study. Nevertheless, a planet without a magnetic field and with a smooth ionosphere might prove to be a suitable application. In a previous contract with NASA, a breadboard of this type of system was developed.

3.   FREQUENCY MODULATION

Frequency modulation using a triangular or sinusoidal waveform has the disadvantage that it can only be reliably used with separate antennas for transmission and reception with considerable isolation between the two. If this isolation does not exist, the high transmitter power cannot be kept from overloading the receiver. If the transmitter is turned off during the reception period, the modulation-type actually reverts to a complex pulse-modulated waveform. A form of this type of modulation is discussed as a system concept in Section 3-D.

## D.  SYSTEM CONSIDERATIONS

Having determined the basic parametric relation-
ships in Section 3-B and reviewed the basic types of modula-
tion in Section 3-C, the system aspects will now be considered.
The present state of radar development incorporates several
optimum techniques which have been studied relative to planetary
sounding systems.

### 1.  OPTIMIZING TECHNIQUES

#### a.  MATCHED FILTER

The radar receiver has been shown to exhibit optimum
performance when it contains a filter network having a trans-
fer function which is the conjugate of the target echo spectrum.
This matched filter forms the cross-correlation between the
received signal corrupted by noise and a replica of the trans-
mitted signal which is designed into the filter's frequency
response function.

The matched filter has the same amplitude spectrum
as the signal, but a negative phase spectrum plus a phase
shift proportional to frequency.  Therefore, the output of
the filter is not a replica of the input signal and cannot
be used for applications where this requirement exists.
Regardless of the shape of the input signal the maximum ratio
of peak signal power to mean noise power is equal to $(2E)/N_O$
where E is the signal energy and $N_O$ is the noise power per
cycle of bandwidth.  In practice the effect of doppler shift
becomes a primary consideration.

#### b.  CORRELATION RECEIVER

The cross-correlation receiver gives performance
equivalent to the matched-filter receiver but is implemented
in a different manner.  A noise-free replica of the trans-
mitted signal is coherently stored or delayed and compared
with the return target echo signal by multiplying the two

52

waveforms and averaging the output in a low-pass filter. The coherently stored or delayed replica must be compared in time coincidence with the return signal, necessitating variable storage or delay. Doppler channels must be used to cover the possible doppler-shifted spectrum.

c.  PULSE-COMPRESSION RADAR

Pulse compression is a special form of the matched-filter radar. Linear pulse compression or chirp resulted from the need to transmit greater amounts of energy from peak-power limited transmitters without loss of resolution capability. It is accomplished by transmitting a constant-amplitude linear FM signal during a duration $\tau$. This frequency sweep increases from $f_1$ to $f_2$. Upon reception, the FM echo is passed through a pulse-compression filter having the property that the velocity of propagation through the filter is a function of frequency. Frequencies $f_1$ through $f_2$ are delayed relative to $f_2$ in a proportional manner so that the original pulse duration $\tau$ is compressed into a shorter pulse of duration $1/B$, where $B = f_2 - f_1$. Conservation of energy provides an instantaneous peak power which is $B$- times the original echo power. This is called the "compression ratio." The noise in the receiver is random and it does not exhibit this buildup.

Since the system resolution is determined by the bandwidth B, increased compression ratios can be obtained without loss of resolution by increasing the transmission duration $\tau$. In practice, a slight loss of resolution does occur, and the limitations of this system depend upon the ability to realize the required filter characteristics and the linear sweep. The proper sweep may be realized more accurately by deriving it from the pulse-compression filter directly with an impulse applied to the filter in the reverse direction.

Linear pulse-compression systems can be readily designed for good resolution without ambiguity. Since the frequency components have a linear relationship, frequency doppler shift of the return echo effects all frequency components approximately the same so that a minimum of degradation and acquisition problems occur.

Filter networks have been made from lumped tapped delay lines with phase-shifting networks at each tap; from all-pass band-pass networks; and from acoustical dispersive delay lines. The state of the art has been determined primarily by the requirements set forth by conventional radar. Dispersive delays greater than several milliseconds become research and development tasks.

Since the spectral envelope of linear pulse compression has a rectangular shape, the corresponding time function has a $(\sin x)/x$ form. Spurious lobes adjacent to the main lobe can be reduced by "weighting" filters which attenuate the frequency components at the edges of the rectangular frequency band. Reduction of the time side lobes can be made 20 to 30 db or more below the main lobe response, with reduction of the S/N by the order of 1 or 2 db.

Pulse compression need not be restricted to linear FM. If the filter is designed to match the transmitted waveform, almost any form of frequency or phase modulation may be used. Phase-coded pulse compression using a transmitted duration $\tau$ divided in $B\tau$ intervals each of $1/B$ duration has been used. Phase reversals of 180 degrees can be used to modulate each interval according to a prescribed code.

d.   INTEGRATION

When the return signal energy is insufficient for extraction from the noise during one modulation cycle, integration of many echo returns can be used to reach a detection threshold.

54

Coherent integration is accomplished by coherently detecting the received signal and preserving its phase information. Both sine and cosine functions of the signal are stored and the addition of successive samples before final threshold detection allows a direct enhancement of S/N. The S/N improvement is linear--that is, $\Delta(S/N) \doteq n$, where n is the number of samples. This is also referred to as predetection or cross-correlation detection integration.

Noncoherent integration is accomplished after envelope detection wherein the phase information is lost. Successive samples are stored before final threshold detection similar to coherent detection but is only linear for S/N greater than several db. When the signal is well below the noise, the improvement is $\Delta(S/N) \doteq n^{1/2}$. This is referred to as post-detection or autocorrelation detection integration. Figure 20 illustrates the above improvements. Figure 21 shows the number of noncoherently integrated samples versus coherently integrated samples which must be added to achieve the same resulting improvement.

## 2.   RELATION TO PLANETARY SOUNDER

The anticipated sounding distances expected will require the optimizing of return signal energy relative to cosmic noise within the power, weight, and size constraints. The system bandwidth will be determined by the required resolution. When sounding from long distances to the planet, the modulation rate must be kept low to avoid range ambiguities. The frequency spectrum will contain spectral lines spaced at the modulation rate. Since this rate is low, the lines will be closely spaced. In a matched filter design, separation of lines from the noise requires that extremely accurate frequencies be transmitted and accurate frequency determining components be used. Means must be used to frequency slew the local oscillator of the receiver or the transmitter to acquire
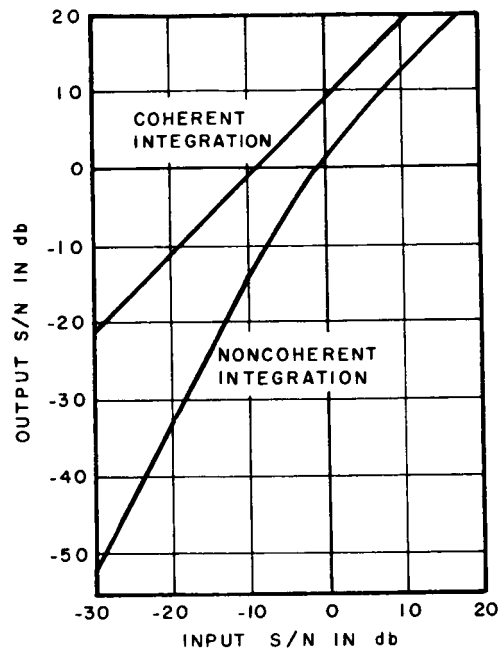
FIGURE 20.   COHERENT VS NONCOHERENT INTEGRATION
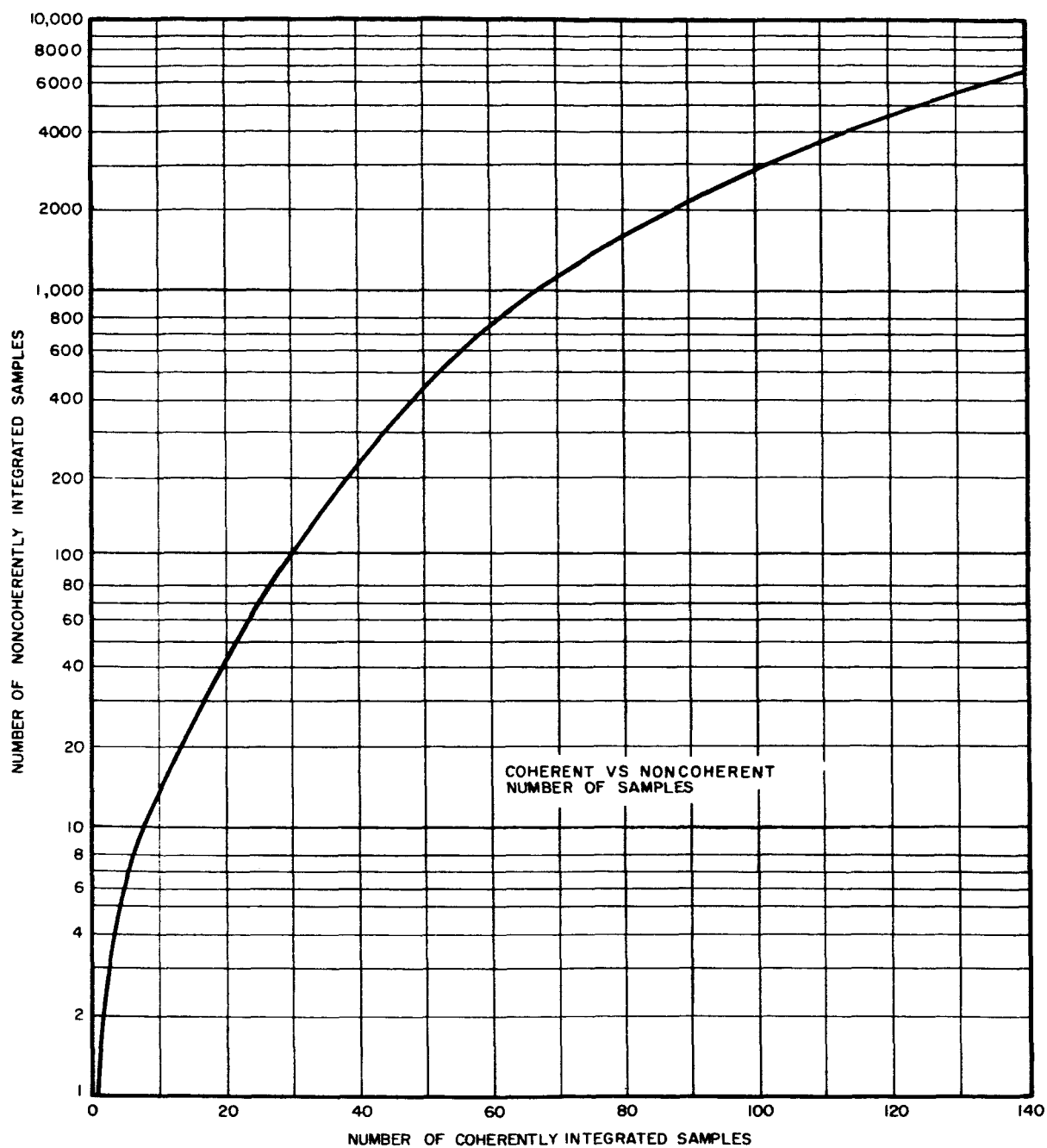
FIGURE 21. NUMBER OF COHERENT AND NONCOHERENT SAMPLES

the doppler shifted signal. Assuming very narrow band-pass
filters for each spectral line, the slewing rate must be kept
low because of the slow response time of tne filter and the
possibility of sweeping past the echo signal without acquiring.

This approach does not appear to be readily adapt-
able to long-distance planetary sounding.

The necessity of the correlation receiver to main-
tain a faithful replica of the transmitted waveform during
the round-trip propagation time imposes stringent require-
ments upon the delay or storage mechanism. The primary power
limitations and the reliability of the storage and delay tech-
niques required appear to indicate that this system is presently
unfeasible.

The use of coherent and noncoherent integration
shows considerable promise for long-distance sounding applica-
tions. Although coherent integration requires much greater
complexity, the significant advantage over noncoherency in
extracting signal from noise dictates its choice beyond cer-
tain ranges.

A method of performing coherent integration would
be to consider an unambiguous range divided into range ele-
ments. After transmission, each range element is coherently
detected and its amplitude and phase information preserved
in separate sine and cosine channels. Each channel is con-
verted to a digital form and this information is retained in
a nondestructive core storage matrix determined by the number
of range elements per period and the number of periods which
are to be integrated. Once the matrix has been filled, the
readout is performed in a serial fashion, in quadrature from
the readin, so that the first range element in each period is
sequentially observed. This process is continued for each
range element. The sine and cosine portion of each range ele-
ment are combined in a digital-to-analog processor in the form

of a balanced modulator and the signal is converted back to
an intermediate frequency.  This signal is then mixed with
a fine doppler scan oscillator and compared with a band-pass
detector.  For each incremental frequency change of the scan
oscillator, the matrix is read out as described.  The scan
oscillator will be stepped through the range of the expected
doppler frequency shift.  At some doppler frequency, one of
the range elements will provide a maximum response at the
detector, thereby indicating the range and the doppler shift.

The potential of pulse compression is limited by
the present state-of-the-art delay lines which are an out-
growth of the application to conventional Earth-based radar.
An obvious solution to far greater delays would be to cascade
existing networks with suitable amplification to overcome the
network losses.  The limitation of this technique would be
dependent upon (1) the continuity of linear dispersive delay,
(2) the overall degradation of S/N due to network losses until
amplifier noise figure becomes significant, and (3) when the
size and weight of the network becomes excessive.  New designs
for this specific application using much of the existing tech-
nology might prove more fruitful than the above approach.
Further study of the detailed requirement would be necessary.
Recently, new concepts for delay applications have appeared
which should be studied for future utilization.  These involve
experiments with magnetoelastic wave propagation at microwave
frequencies, in very compact structures.

For the narrow bandwidths used in sounding systems,
all-pass band-pass networks appear to be the best method of
obtaining reasonably long dispersive delays with a minimum
size and weight.

E.   APPLICATION TO MISSIONS

The formulated data can now be used to determine
the requirements for specific missions.  A suggested procedure

for the use of these graphs is given below.  However, they may be applied in any expeditious manner.  The applications cover a wide variation in distance.  If the total distance is divided into intervals, these intervals can be specified as operating modes.

### 1.  MODES OF OPERATION

Multiple mode operation for different range intervals lends itself to many possible missions.  Each mode which goes to further ranges adds an additional complexity to bring up the signal level to the simpler system for the next closer range.  This philosophy avoids completely different systems for different ranges or missions and results in a simpler, more reliable, overall approach.  In long-distance sounding systems, an acquisition mode is required due to the low levels of the reflected signals that result from power limitations.  Four modes of operation are specified in the following paragraphs; one for acquisition and three for fine ranging in each of three relative range intervals--far, intermediate, and near.  The range intervals are defined relative to the sounding capability of the system

### 2.  USE OF DATA

The maximum operating distance for each range interval is a function of the complexity of the system.  By the use of S/N improvement and coherent and/or noncoherent integration techniques, the greater distances can be covered.  For lesser distances, either the complexity or required power can be reduced.

The available average power for transmission will in most cases be determined by mission constraints.  The assumed total primary power available for the following missions is 15 watts.  For transmission, 5 watts average at 50-percent efficiency will be used, thereby consuming 10 watts

total.  This will leave 5 watts of primary power for the
remainder of the system.

A required resolution of 75 km has been specified
for these applications.

For the use of this data a modulation period must
be determined.  To avoid ambiguity, the modulation period
must be greater than the round-trip propagation time for the
maximum working distance:

$$T = \frac{2D}{c}.$$

By consulting Figure 7, the transmitted energy
required to operate over a given range can be determined.
This is the product of the average power and transmission
time required.  If this amount of energy is not available
during one modulation period, then the power must be inte-
grated over more than one modulation period upon reception.
This is determined by dividing the data from Figure 7 by the
average transmission power to determine the time.  If this
time is greater than one modulation period, it should be
divided by the modulation period to determine the number of
samples which must be integrated coherently.  If noncoherent
integration is to be used, Figure 21 will indicate the num-
ber of samples required.

The antenna matching network losses have not
been included in the evaluation of the required energy in
Figure 7 and must now be considered.  The choice of antenna
pole length will be determined by mounting and/or weight
considerations, frequency range, and permissible loss which
will still allow a feasible mission.  Figures 15 and 16 for
antenna matching losses, and Figure 6 for effective S/N
improvement due to the cosmic noise decrease at low fre-
quencies, should be used.  Any other S/N improvement tech-

61

niques should be evaluated and the resultant loss or gain from the above considerations used to modify the power, or integration time required.

3. MISSIONS

The following assumptions will be used for the missions studied in this section:

1. Since modulation methods do not make significant differences in the ability of a sounder to operate over a given distance, the pulse sounder, due to its familiarity and simplicity will be chosen as the basic system.

2. Antenna poles of 60-foot length (120 feet tip-to-tip) with a matching network Q = 200 will be used for the lower sounding frequencies.

3. A primary overall range of 1000 to 40,000 km will be considered as most likely for missions, with extension to 100,000 km under marginal conditions.

4. All missions will be applied to Mars, which is the worst case. Similar missions to Venus would be from 1 to 5 db better over the maximum distance variation covered by this study.

5. A transmitter with a peak power of 500 watts and a duty cycle of 0.01 will be assumed. This transmitter is feasible within the present state of the art of power semiconductors over this frequency range.

a. MODE OPERATIONS

(1) MODE 1--ACQUISITION

Before presenting mission parameters, the problem of initial acquisition of the return echo must be considered. Since integration will be required at the farther ranges to extract the signal from the noise, a range gate must be provided at the time of echo return to allow optimum S/N storage. Without this provision the receiver would store noise through-

62

out the modulation period and detection would be impossible. If 75-km resolution were desired at a 40,000-km maximum range, and since the distance is not known, there would be a requirement for 40,000/75 = 533 separate range gate channels.

By providing an acquisition mode for the system which determines the echo range within 1500 km, the number of channels could be reduced to 27. The system bandwidth is also reduced so that less noise enters the receiver. Once the range is determined within 1500 km, normal sounding could use the same storage equipment to determine the range to 75 km. The number of channels required would be 1500/75 = 20 of the 27 available.

For acquisition to 40,000 km, the 500-watt peak pulse transmitter operating with a 0.01 duty cycle provides an average 5 watts of power. A resolution of 1500 km necessitates (from Figure 8) a 100-cps bandwidth and a 10-msec pulse width. The modulation period is therefore $(10 \times 10^{-3})/0.01 = 1$ second.

From Figure 7, the required energy at 40,000 km is 100 joules. The required coherent integration time is 100 joules/5 watts = 20 seconds.

Since the modulation period is 1 second, 20 coherently integrated samples are required. The digital storage matrix described in Section 3-D would require a minimum of 27 range elements (range-gate channels) repeated 20 times or 540 bits of information storage. If both sine and cosine channels have the amplitude digitized by 4 bits of information, a storage matrix is required of 540 x 2 x 4 = 4320 bits.

After detection with a doppler scan oscillator, further noncoherent integration can be used to provide an operating margin. A 10-db margin can be obtained by approximately 14 repetitions of the above detection cycle.

## (2)  MODE 2--FAR RANGE

If the acquisition mode determines that the ionospheric range is between 20,000 and 40,000 km, mode 2 operation commences.  The approximate range is now selected by the acquisition gate and examined in greater detail.  To obtain a resolution of 500 μsec (75 km), a 2-kc bandwidth is required which increases the noise entering the receiver or an effective signal loss of 20 × (13 db).

Pulse compression is used to extract the signal under these conditions.  The 10-msec transmitter pulse is linearly chirped over 2 kc.  Upon reception, the obscured signal is compressed by an all-pass time-delay network from the original 10-msec duration to a 500-μsec duration.  This is a compression ratio of 20 times or an increase in signal strength of 13 db.  The signal entering the coherent detector is now at the same level obtained during acquisition but the resolution has been improved by a factor of 20 times.

Detection of the doppler-shifted return is accomplished in the same manner as during acquisition except now the target range is known to exist within the acquisition gate.  This gate is 11 msec wide and is divided into twenty-two 500 μsec (75 km) elements and stored for 20 gate periods.  The doppler ambiguity is resolved in the same manner as during acquisition.  The gated information is envelope-detected and stored in a register matrix.  Noncoherent integration to provide a 10-db margin is required at the furthest range.  The 20,000-km minimum range in this mode is the distance at which this integration is no longer required, as shown in the mode 3 description below.

## (3)  MODE 3--INTERMEDIATE RANGE

If the acquisition mode determines that the ionospheric range is between 8000 and 20,000 km, mode 3 operation

64

commences. This mode is identical with mode 2 operation
except that the noncoherent integration is no longer needed
because of decreased path and defocusing loss.

From Figure 7, the required energy at 40,000 km
was 100 joules. At 20,000 km, this energy is reduced to
7.25 joules or a change of $100/7.25 = 13.8X$ or 11.4 db.

The 10-db operating margin provided by the non-
coherent integration is not needed.

The 8000-km minimum range is determined as the
distance below which coherent integration is no longer
required. The transition is explained in the mode 4
description.

### (4) MODE 4--NEAR RANGE

If the spacecraft is between about 1000 and
8000 km from the ionosphere, the received signal level will
be sufficient for noncoherent integrated pulse detection.
The acquisition mode will indicate a short range and place
the system in this mode. The transmitter will radiate
500-μsec pulses. The pulse-compression network and coherent
integration matrix will be bypassed and the incoherent inte-
gration circuitry will receive the signal directly. The
transfer to this mode can be examined by consulting Figure 7
for the conditions that follow.

The 500-μsec pulses (75-km resolution) occur at a
0.01 duty cycle, so that the modulation period is $(500 \times 10^{-6}/0.01 = 50 \times 10^{-3} = 50$ msec.

The transmitted energy available during this period
is 5 watts $\times 50 \times 10^{-3} = 0.25$ joule. This occurs at 7500 km
for Mars and 9500 km for Venus. A 10-db operating margin can
be obtained by integrating 14 pulses noncoherently. The range
at which the noncoherent integration can be dispensed with can
be determined: (0.25 joule)/10 = 0.025 joule. This occurs at

3700 km for Mars and 4400 km for Venus. Therefore, a conventional pulse sounder without integration can be used between 1000 km and a nominal 4000 km with more than a 10-db operating margin. The transition at 4000 km can be considered either as a separate mode or a subsidiary mode since the integration can just as easily be kept in operation.

### (5) EXTENSION TO 100,000 km

For operation to 100,000 km, a modulation period greater than

$$T = \frac{2D}{c} = \frac{2 \times 10^5}{3 \times 10^5} = 0.667 \text{ second}$$

is required. The system described has a period of 1 second during acquisition and at far ranges, satisfying the above condition. The level of complexity of the above system could possibly be maintained if the operating margin is reduced to zero at 100,000 km. The noncoherent integration of 10 db previously considered would provide 100 joules x 10 = 1000 joules and would extend operation to 73,000 km. The energy required at 100,000 km is 3500 joules. This would mean coherent integration of 3500 joules/100 joules = 35X, or noncoherent integration (from Figure 17) of 160 pulses. Detection would occur at (160 x 20)/60 $\doteq$ 54 minute intervals.

Although the time intervals at these great distances are large, the angular rate of motion relative to the planet may be slow enough to consider such time intervals. Rotations of the planet is significant in these intervals as well as changes in the sub-spacecraft point in the ionosphere for sounding over a range of frequencies. Aside from weight and power, the ultimate limitation in ranging distance would appear to be that point at which conditions have changed so drastically in a measurement time interval that the measured

66

quantities are no longer interpretable as useful physical
information. It is believed this point is reached before
limitations due to the stability of elements, such as oscil-
lators.

By the use of noncoherent integration, operation
is possible to 100,000 km provided an additional sliding
range gate is used to view only 40,000-km intervals during
acquisition. This would initially determine the distance
within 40,000 km, after which operation would proceed as
described previously.

### b.   SOUNDING FREQUENCIES

The sounding frequencies should be derived from a
single crystal oscillator using frequency synthesis tech-
niques. The frequency synthesizer would allow the sounding
frequency to be changed in small or large increments while
still maintaining the accuracy and stability of the crystal.
These devices can be programmed to provide as many, or as few,
different frequencies as may be required by the dictates of
the mission and the operating modes.

### c.   ANTENNAS

The matching network losses indicated in Fig-
ures 15 and 16 illustrate the rapid degradation that occurs
as the operating frequency is lowered. A linear approxima-
tion was assumed for the cosmic noise power, and this approxi-
mation was used for the required energy data of Figure 7.
The cosmic noise actually decreases below 1.8 Mc. Due to
this decrease, the combined effects of the antenna matching
network loss and actual cosmic noise makes the signal to noise
ratio the lowest at about 1.5 Mc.

If a given set of operating conditions and antenna
pole length has been established and it is determined that a
shorter pole length must be used, the lowest operating fre-

quency will be increased by one octave for each halving of the antenna pole length, all other conditions remaining the same.

Pole lengths of 60 feet were assumed in the previous applications. These would be used over a range of about 0.5 to 4.0 Mc. Above the half wavelength of this dipole at 4.0 Mc, the antenna pattern would begin to degrade. For operation to 10 Mc, a 20-foot pole length would maintain its pattern while at 4.0 Mc the increasing matching losses would reduce the operating margin by about 5 db.

The matching networks must accommodate the frequency bands with minimum losses. The use of frequency synthesizers, as compared with swept oscillator, assists in this regard, since the frequencies may be selected.

d.    FOUR-MODE SYSTEM

A block diagram of a system having the performance characteristics described is shown in Figure 22. A brief description of the system is given below for the various modes of operation.

For acquisition (mode 1), the frequency synthesizer is programmed to a sounding frequency whose carrier is pulse modulated for 10 msec and applied to the power amplifier. The power amplifier provides a 500-watt peak pulse to the matching network and antenna. The transmit-receive (T/R) device prevents damage to the receiver at this time. The return echo picked up by the antenna passes through the matching network, T/R device, and is amplified by a broad-band preamplifier. After mixing, the echo is further amplified at the intermediate frequency, passed through a 2-kc filter, a limiter ( for high level signals), and a 100-cps band-pass filter.
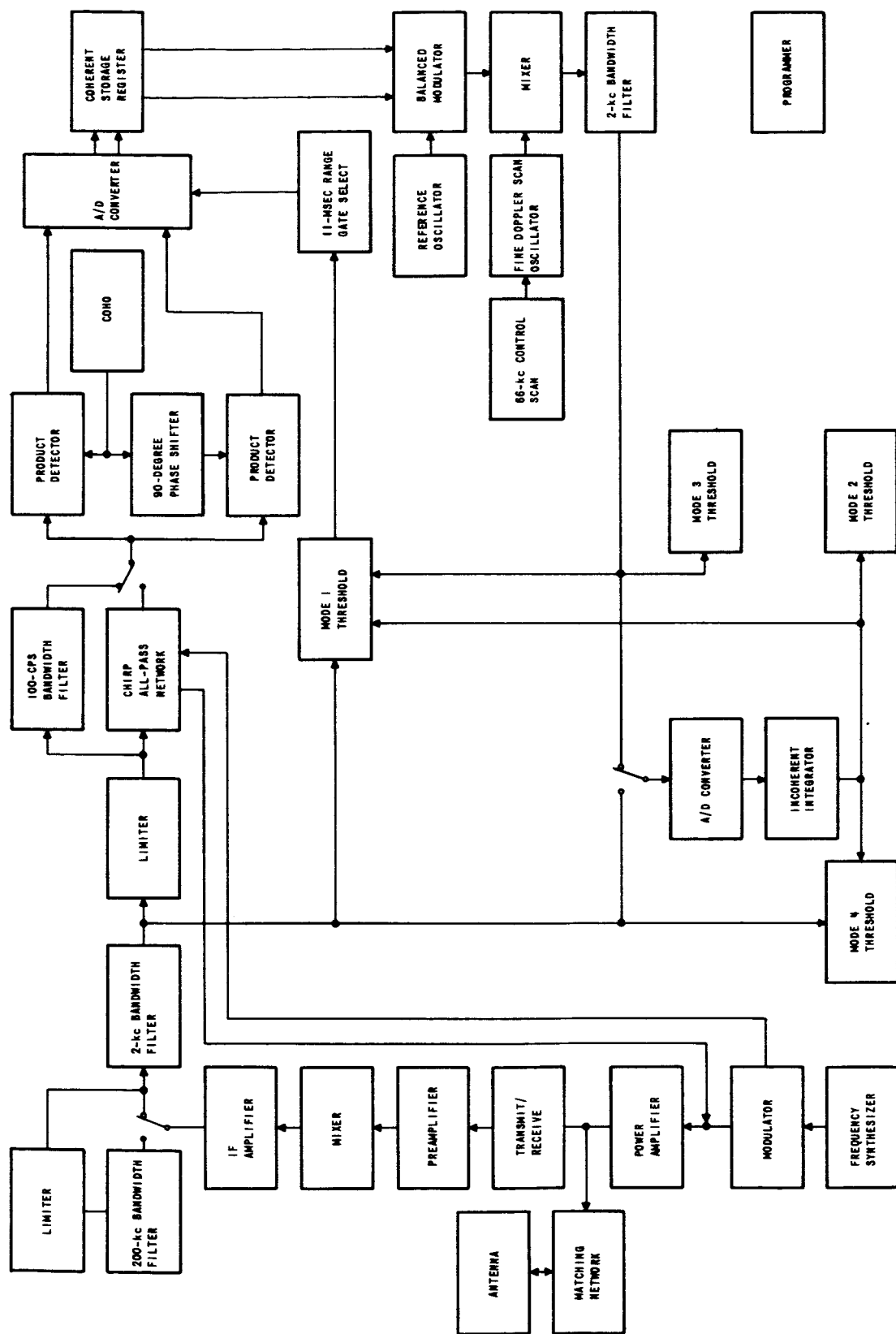
68

FIGURE 22. BLOCK DIAGRAM OF FOUR-MODE SYSTEM

The echo signal is split at this point to two product detectors of the coherent detector. A coherent oscillator feeds one detector directly and the other through a 90-degree phase shifter. The two detected outputs are the sine and cosine function of the echo signal. These waveforms are each amplitude digitized by 4 bits in an analog-to-digital converter.

The digital output is stored and processed in the coherent storage register/balanced modulator circuitry as described in Section 4-D and passed through a 2-kc filter. If the resultant signal level is sufficient, it exceeds the mode 1 threshold and is detected. If the signal level is insufficient to allow threshold detection with a single output pulse, a series of these output pulses will be passed through a second analog-to-digital converter and incoherently integrated in a second core matrix similar to the coherent storage register.

When enough pulses have been stored to provide detection, conversion from digital-to-analog information occurs and the mode 1 threshold is exceeded. One output of the mode 1 threshold is used by the programmer to start the next mode of operation and readout triggering. A second output from the mode 1 threshold is used to operate the 11 msec range gate select circuit which gates the analog-to-digital converter for the fine range intervals in subsequent modes.

If the spacecraft range is suitable for mode 2 operation, the output of the modulator provides an impulse in the reverse direction to the chirp all-pass network which stretches and frequency modulates the pulse in a 2-kc band. This signal is applied to the power amplifier and system operation is identical to mode 1 operation until the output of the receiver IF amplifier is reached. For all fine range

resolving modes, the output of the IF amplifier is switched
to pass the signal through a 200-kc filter and a first lim-
iter. This circuitry reduces the required dynamic range of
the second limiter with a minimum of phase distortion. After
passing through the 2-kc band-pass filter and second limiter,
the signal is compressed by the chirp all-pass network. The
output of this network is switched to the coherent storage
register in all fine ranging modes. The remainder of the
circuitry is identical to mode 1 except that the acquisition
detector is now disabled and the signal is incoherently inte-
grated and detected in the mode 2 threshold circuits.

Mode 3 operation is identical to mode 2 except
that, for the shorter ranges of this mode, the echo signal
level will be sufficient to allow detection by the mode 3
threshold circuits without incoherent integration.

When the near range conditions exist for mode 4
operation, the echo signal will have sufficient strength for
detection by the mode 1 threshold circuits without coherent
integration, and the system will be placed in mode 4 opera-
tion. The incoherent integrator circuitry will be switched
to the mode 4 signal path and detection will occur either
directly via the mode 4 threshold detector (if the echo sig-
nal strength is sufficient) or after integration in the
incoherent integrator.

All mode threshold outputs will be sent to the
programmer where this data will be converted to a digital
form and sent to the spacecraft telemetry system along with
appropriate timing and operational information.

e. ESTIMATED SIZE, WEIGHT, AND POWER

Table II gives a size, weight, and power estimate
for this system. The antennas are the furled-tape erectable-
type and may be extended early in the mission. To erect the

## TABLE II

### SIZE, WEIGHT, AND POWER ESTIMATE

| Unit | Volume (cubic inches) | Weight (pounds) | Average Power (watts) |
|---|---|---|---|
| Coherent Storage Register | 40 | 0.3 | 1.0 |
| Balanced Modulator | 30 | 0.2 | 0.2 |
| Mixer | 4 | 0.1 | 0.02 |
| Reference Oscillator | 16 | 0.1 | 0.04 |
| Doppler Scan Oscillator and Scan | 9 | 0.1 | 0.04 |
| 2-kc Bandwidth Filter | 12 | 0.2 | - |
| Analog-to-Digital Converter | 20 | 0.1 | 0.4 |
| Product Detector (2) | 20 | 0.4 | 0.2 |
| 90-Degree Phase Shifter | 6 | 0.1 | 0.05 |
| Coherent Oscillator | 9 | 0.1 | 0.05 |
| Range Gate Select | 6 | 0.1 | 0.02 |
| Detector-Acquisition | 4 | 0.05 | 0.01 |
| Mode 3 Threshold Detector | 3 | 0.05 | 0.01 |
| Analog-to-Digital Converter | 20 | 0.1 | 0.4 |
| Incoherent Integrator | 10 | 0.2 | 0.2 |
| Mode 4 Threshold | 3 | 0.05 | 0.01 |
| 100-cps Filter | 12 | 0.2 | - |
| Chirp Filter | 96 | 1.0 | - |
| Limiter (2) | 16 | 0.2 | 0.1 |
| 2-kc Filter | 12 | 0.2 | - |
| 200-kc Filter | 6 | 0.1 | - |
| Receiver | 60 | 0.8 | 0.25 |
| Transmit-Receive | 6 | 0.1 | - |
| Mode 2 Threshold | 3 | 0.05 | 0.01 |
| Power Amplifier | 96 | 1.3 | 10.00 |
| Modulator | 32 | 0.4 | 0.5 |
| Frequency Synthesizer | 40 | 0.5 | 1.0 |
| Matching Network | 108 | 1.5 | - |

TABLE II (cont)

| Unit | Volume (cubic inches) | Weight (pounds) | Average Power (watts) |
|------|------|------|------|
| Programmer | 72 | 0.7 | 0.5 |
| Switches | 3 | 0.3 | 0.1 |
| Cabling, Cover, and Mounting Space | 100 | 0.5 | – |
| Total | 874 | 10.30 | 15.11 |

antennas, power is required only once while erecting. Based on present practice, a 120-foot dipole requires 4 watts of power for 30 minutes and a 40-foot dipole requires 4 watts of power for 20 minutes.

Each nonerected pole takes 72 cubic inches of volume and is 3 by 4 by 6 inches for all lengths. The weight of the 120-foot dipole and 40-foot dipole combination is:

|  | Pounds |
|---|---|
| Two 60-foot poles | 4.5 |
| Two 20-foot poles | 2.8 |

The total weight of the complete instrumentation with a 60-foot and 20-foot dipole is 15.9 pounds.

# SECTION 4
## PROPAGATION STUDIES

Propagation properties in an ionospheric medium have been investigated in terms of parameters that may be instrumented by an ionospheric sounding experiment. The ionospheric electron density, magnetic field, constituents, and temperature of Mars and Venus are not well-known; an experiment using sounding techniques should be able to provide information on the electron content and profile of the upper ionosphere, the magnetic field in the region, the exospheric temperature, the scale height and the mean ion-electron temperature, the solar-planetary relationships, and perhaps, some crude information on upper atmospheric composition.

With the above physical parameters in mind, upper ionospheric models have been considered in terms of wave propagation characteristics. A uniform magnetic field was assumed in the study since it is assumed that a significant portion of the delay time occurs in the region of the reflection point.

At each altitude in the ionosphere, the delay time depends on the local group refractive index as well as on the electron density gradient; the group refractive indices are determined from the Appleton-Hartree relation. Collisions are considered negligible and will be ignored in all virtual depth computations. Since the group refractive index is solely a function of normalized plasma and gyro frequencies, this parameter was initially examined via computations on

the IBM 1620 computer. The tabulations and curves thus obtained are applicable for any ionospheric profile and, therefore, group refractive index computations are presented in this section prior to profile descriptions and virtual depth computations.

Ionospheric electron density profiles for a single and double layer ionosphere are presented in Section 4-B. The electron density, density gradient, and magnetic field are then applied in the virtual depth integral which was machine computed.

Planetary soundings may be made from great heights. Since the height of the sounder above the ionosphere on the planet is uncertain the usual procedure for calculating virtual depth was not followed. Rather, we have defined a differential virtual depth which is the incremental delay due to the medium, and represents the difference between the actual electron density profile and the virtual profile at a given sounding frequency. This incremental depth makes the mathematical approximation that the sounding vehicle is at infinity, although it may be at a finite but sufficiently large altitude. The approximation simplifies the analysis and can be corrected for finite heights. It is believed that it is well suited for planetary studies. It also brings out many interesting propagation properties of the medium of more general use. Differential virtual depths for both the ordinary (o) and extraordinary (x) waves in single-and double-layer profiles are presented in Section 4-C, which contain analyses and comparisons of integrands, high and low-frequency asymptotic limits of differential virtual depths, and modifications of differential virtual depths due to a finite rather than an infinite vehicle altitude.

The computed differential virtual depths were applied to the true profile to obtain the total virtual height relative to an assumed surface in Section 4-D.

## A. GROUP REFRACTIVE INDEX

The group refractive index, ($\mu'$) is defined as the free-space velocity divided by the group velocity of the wave. It is related to the phase refractive index ($\mu$) by

$$\mu' = \frac{\partial}{\partial f}(f\mu),\qquad (16)$$

where f is the wave or sounding frequency. Neglecting collisions, the refractive index[26] is

$$\mu^2 = 1 - \frac{X(1-X)}{D}\qquad (17)$$

where

$$D = 1 - X - \frac{1}{2}Y^2 \sin^2\theta \pm [\frac{1}{4}Y^4 \sin^4\theta + Y^2(1-X)^2 \cos^2\theta]^{\frac{1}{2}}\qquad (18)$$

and $\pm$ signs correspond to ordinary (o) for the upper and extraordinary (x) waves for the lower signs.

X, Y, and $\theta$ are the usual magneto-ionic quantities:

$$X = \frac{e^2 N}{4\pi^2 f^2 \epsilon_o m} = \frac{f_N^2}{f^2}, \text{ normalized plasma frequency parameter},\qquad (19)$$

77

$$Y = \frac{eB_o}{2\pi fm} = \frac{f_H}{f},$$

(20)

normalized gyro-frequency parameter

$\theta$ = angle between magnetic field and wave normal,
e = electronic charge,
m = electron mass,
$\epsilon_o$ = permittivity of free space
$B_o$ = magnetic field in gauss, and
N = electron density as determined from density profile.

Applying equations 16 and 17, Budden finds the group refractive index to be

$$\mu' = \frac{1}{D\mu}\left\{1-X-\mu^2 \pm \frac{\frac{Y^2}{2}\cos^2\theta(1-X^2)(1-\mu^2)}{[Y^2\cos^2\theta(1-X)^2 + \frac{Y^4}{4}\sin^4\theta]^{\frac{1}{2}}} + D\right\}$$

(21)

This expression was used to compute $\mu'$ in the general case. For comparison and as a check on the calculations, computations were also made for the angle $\theta = 23^o$ 16' which was used by Shinn and Whale[27].

Reflection of the longitudinal wave, when $\theta = 0^o$ and the plus sign is used, occurs when X = 1 + Y rather than at X = 1. In this case, the equation for $\mu'$ is greatly simplified;
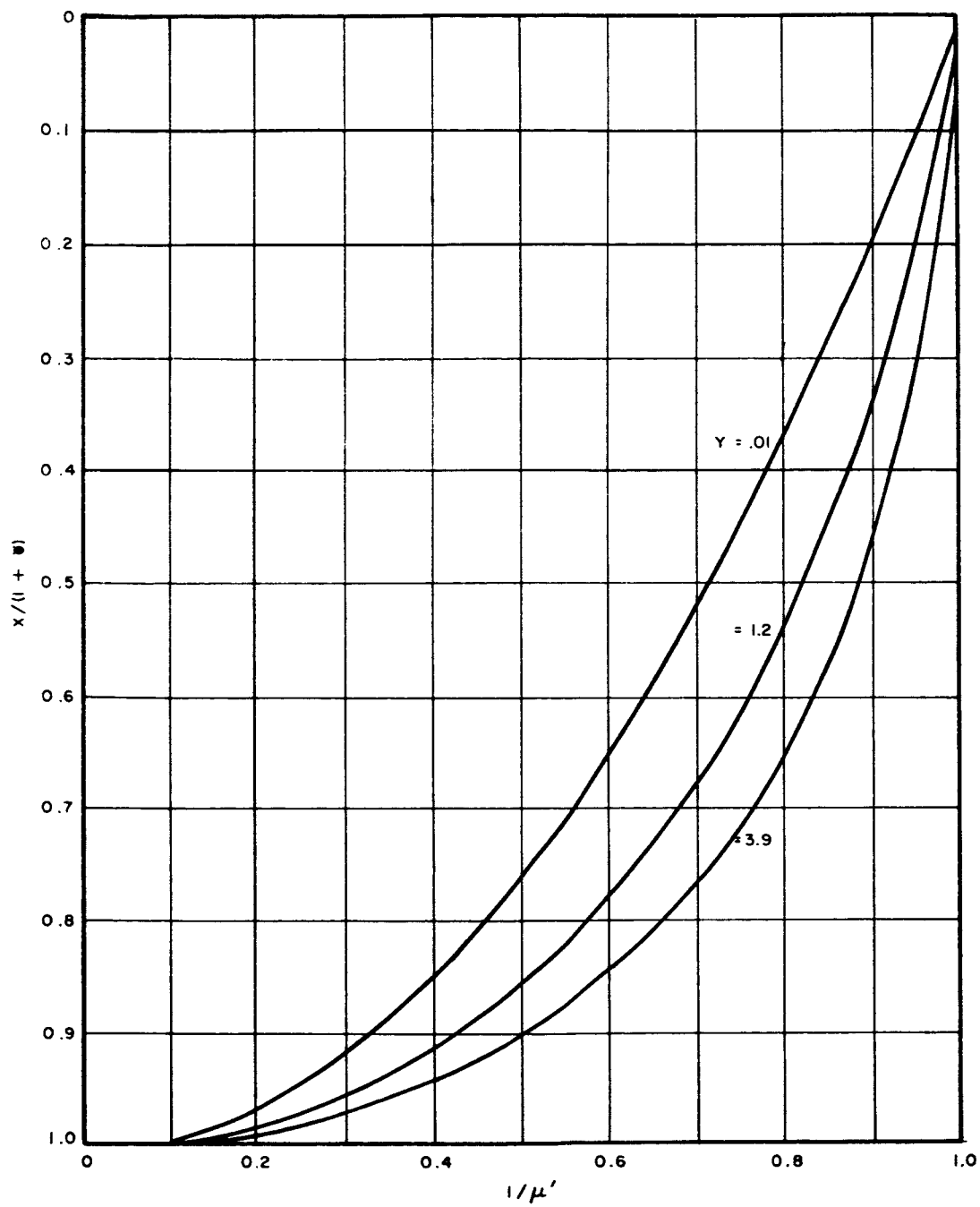
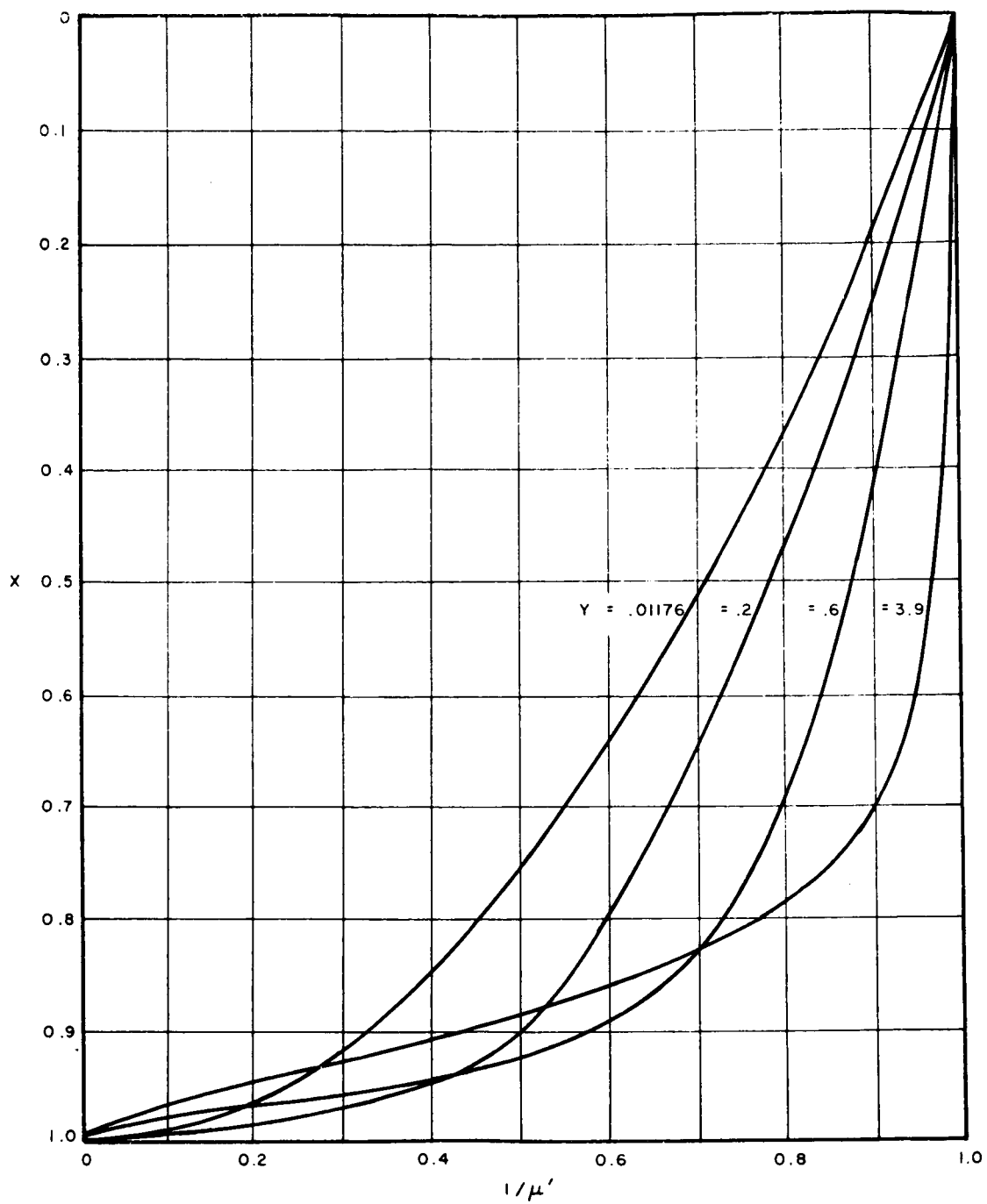78

FIGURE 23.   GROUP REFRACTIVE INDEX (LONGITUDINAL WAVE)
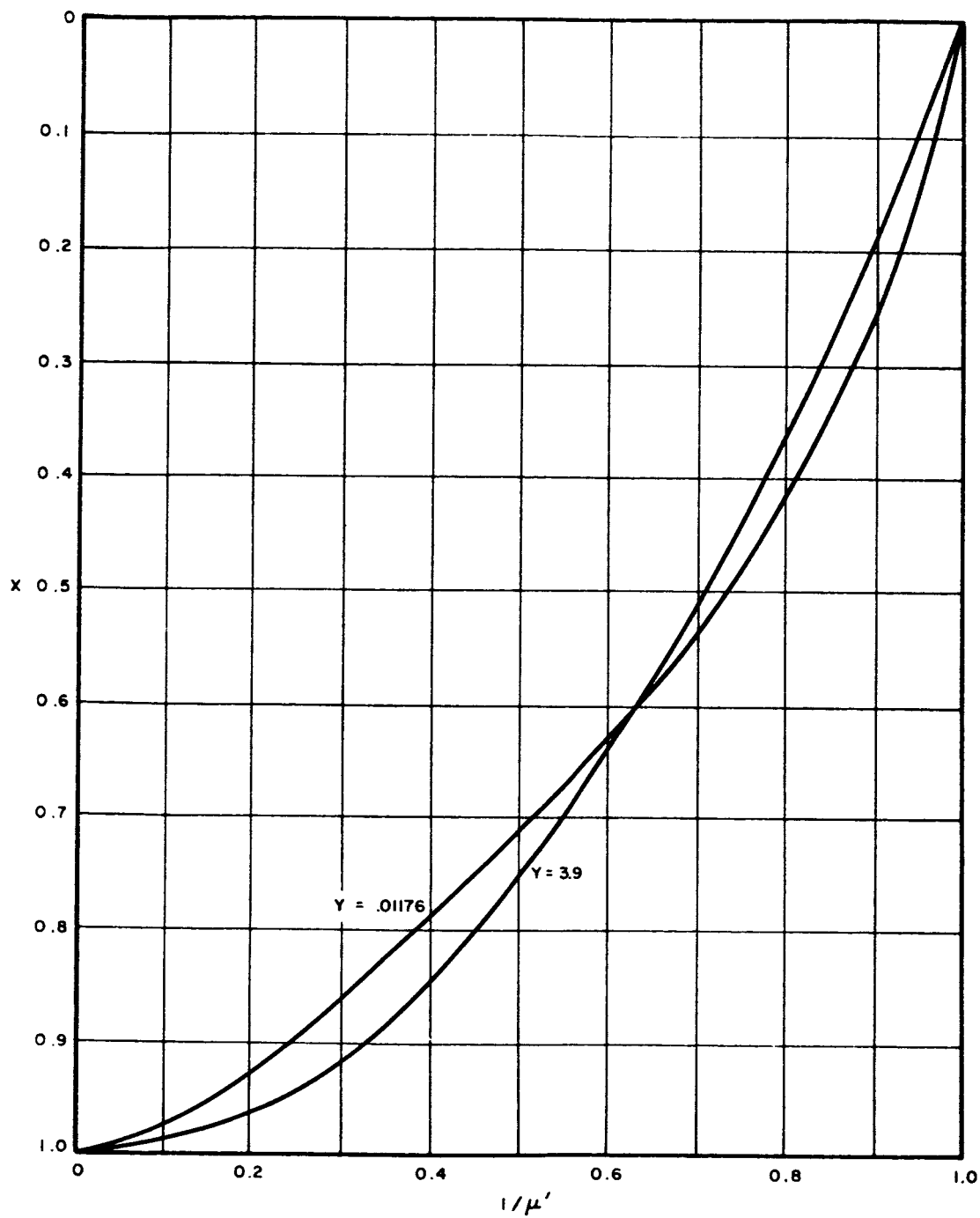
FIGURE 24. GROUP REFRACTIVE INDEX ( o–WAVE, ϴ = 10)
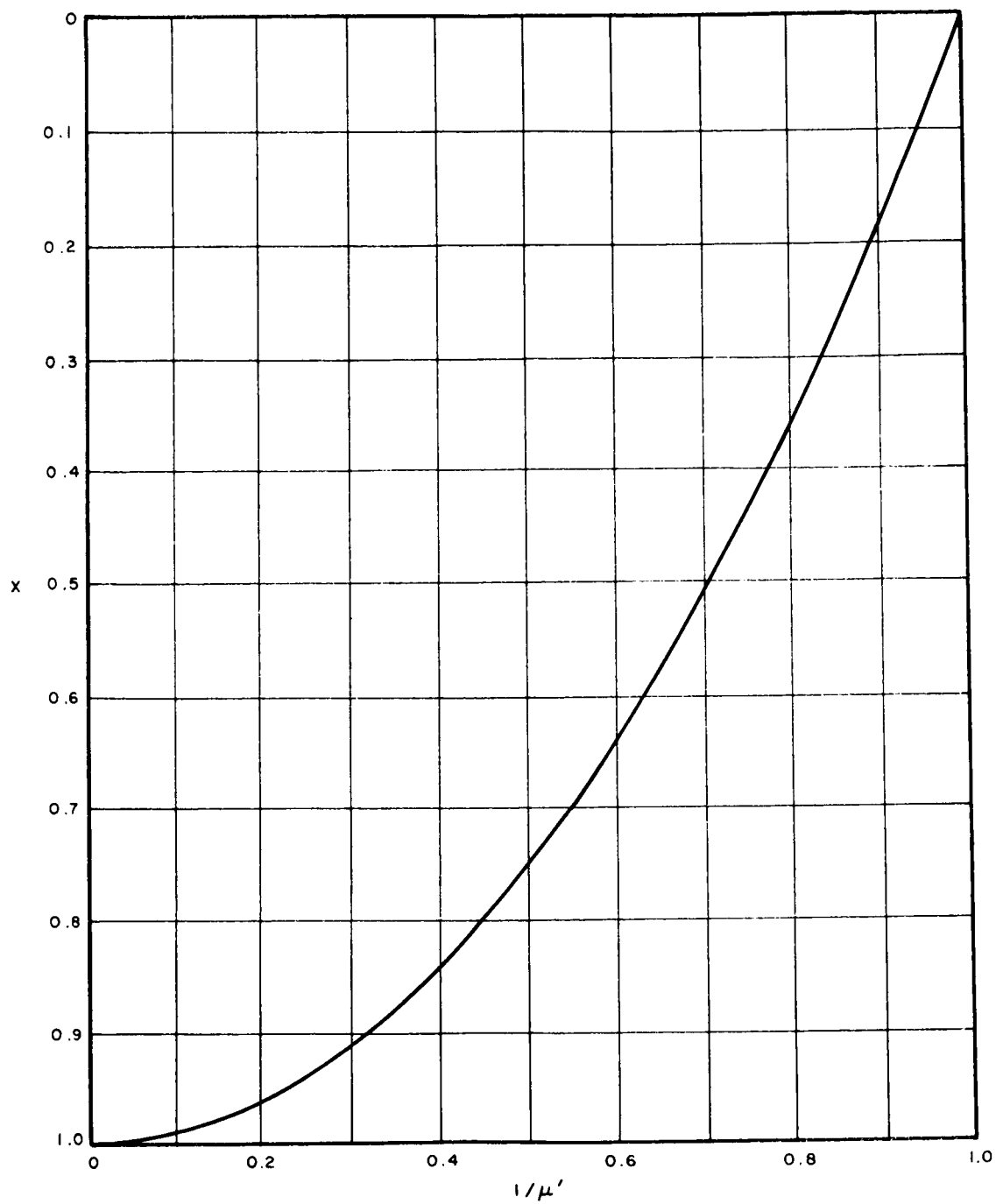
FIGURE 25. GROUP REFRACTIVE INDEX (o-WAVE, $\Theta = 45$)

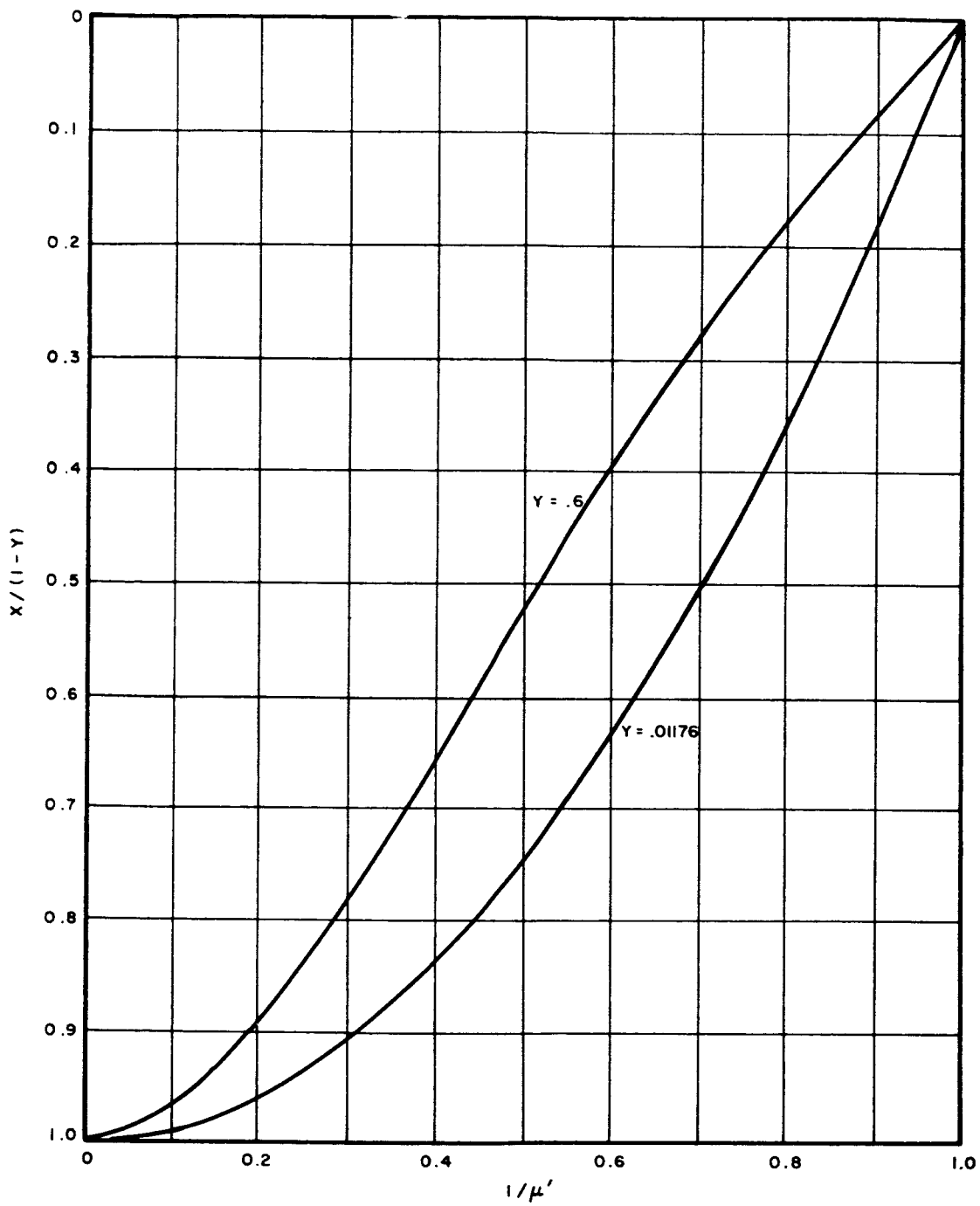FIGURE 26.   GROUP REFRACTIVE INDEX (o-WAVE, $\Theta = 90$)

FIGURE 27.   GROUP REFRACTIVE INDEX (x-WAVE, Y < 1, θ = 0)

83

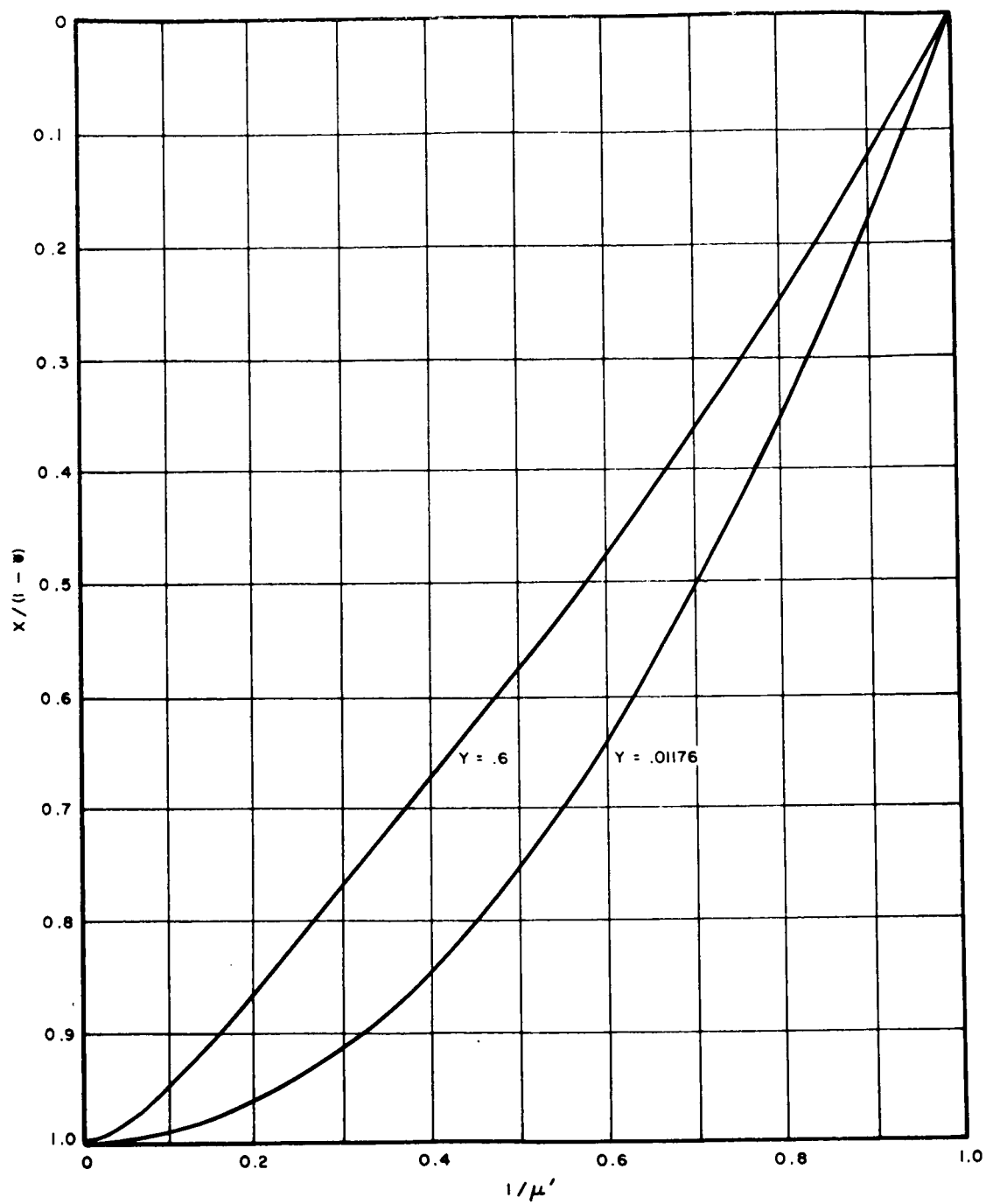FIGURE 28.  GROUP REFRACTIVE INDEX (x-WAVE, Y < 1, θ = 90)
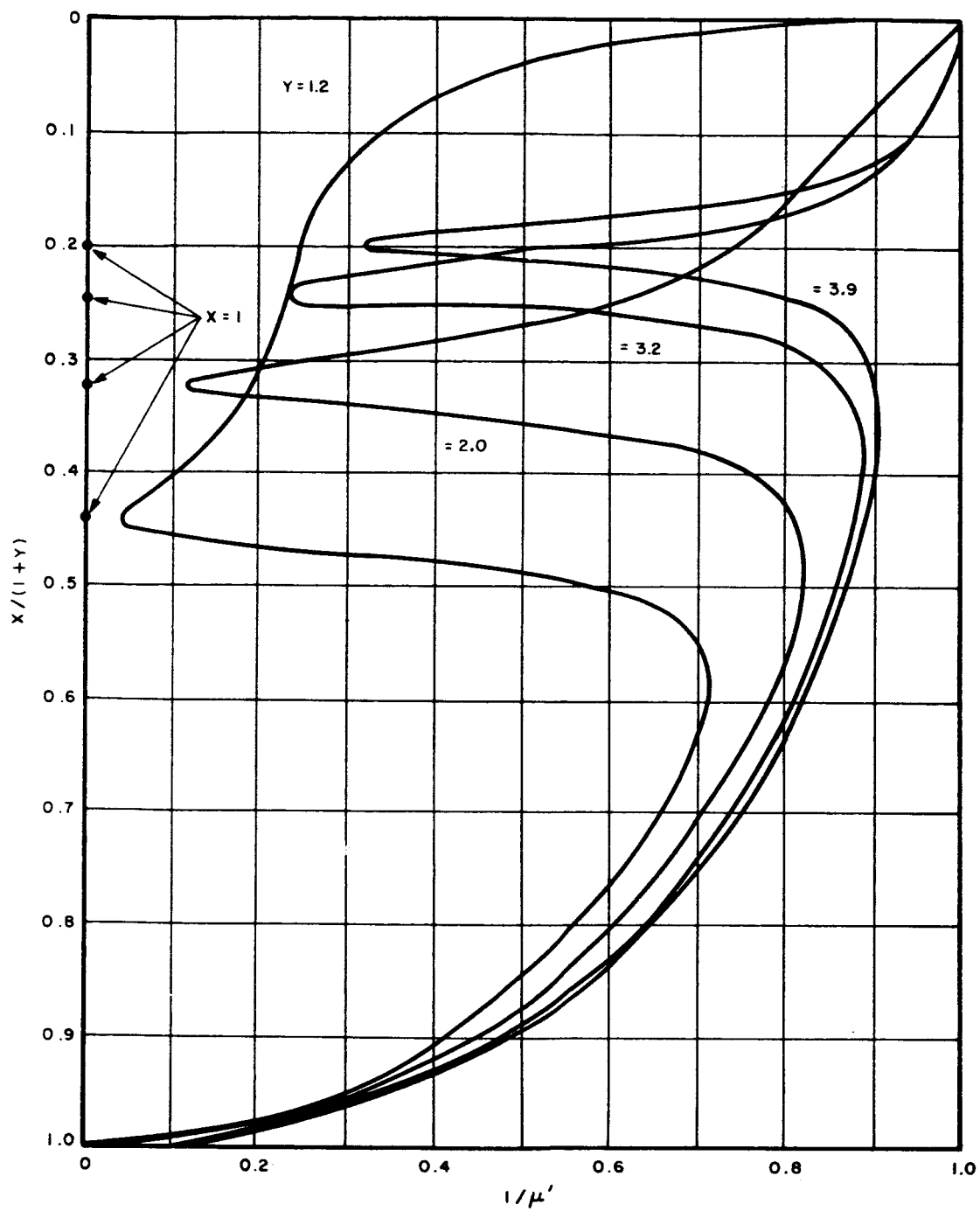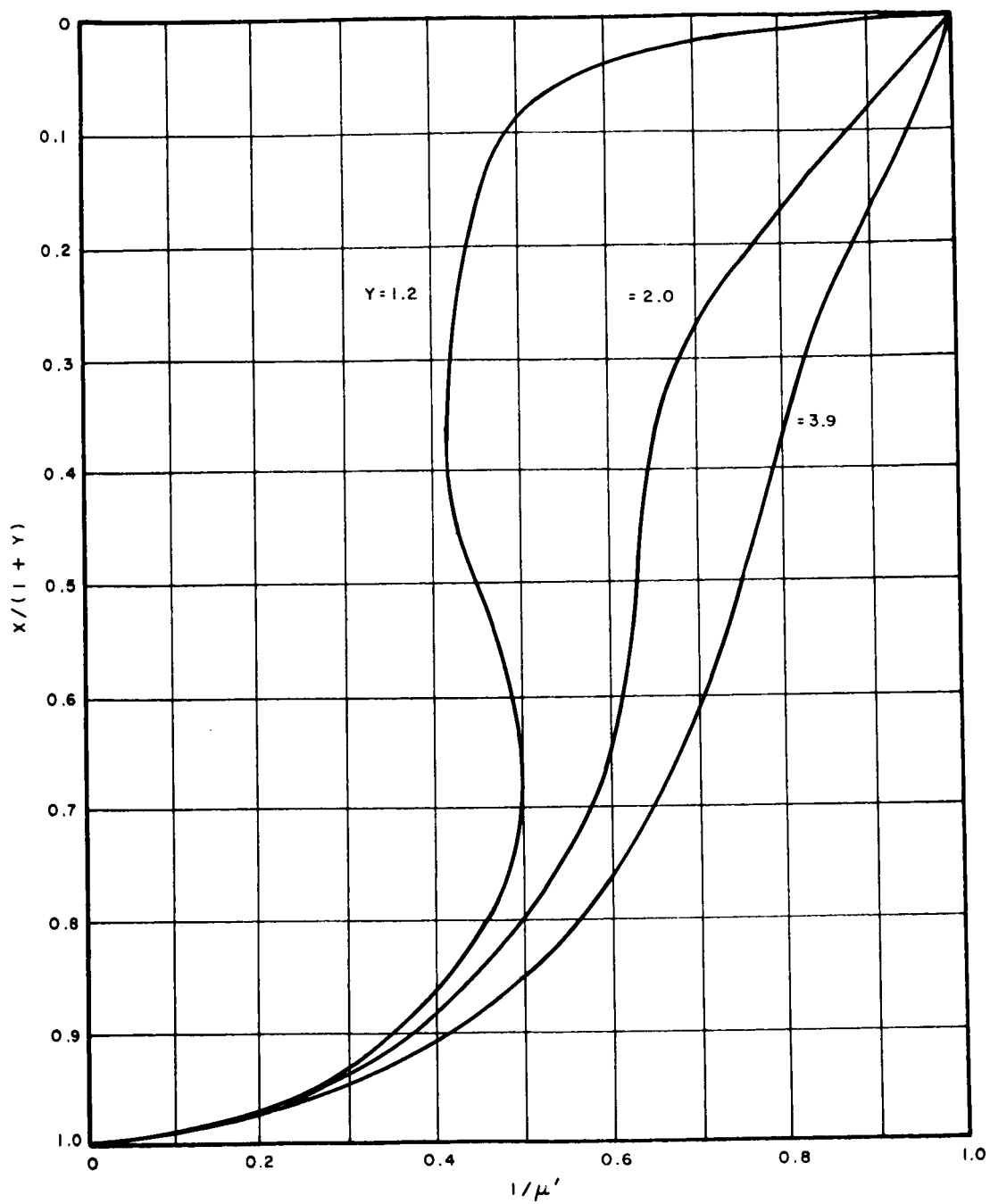
FIGURE 29.   GROUP REFRACTIVE INDEX (x-WAVE, Y > 1, θ = 10)
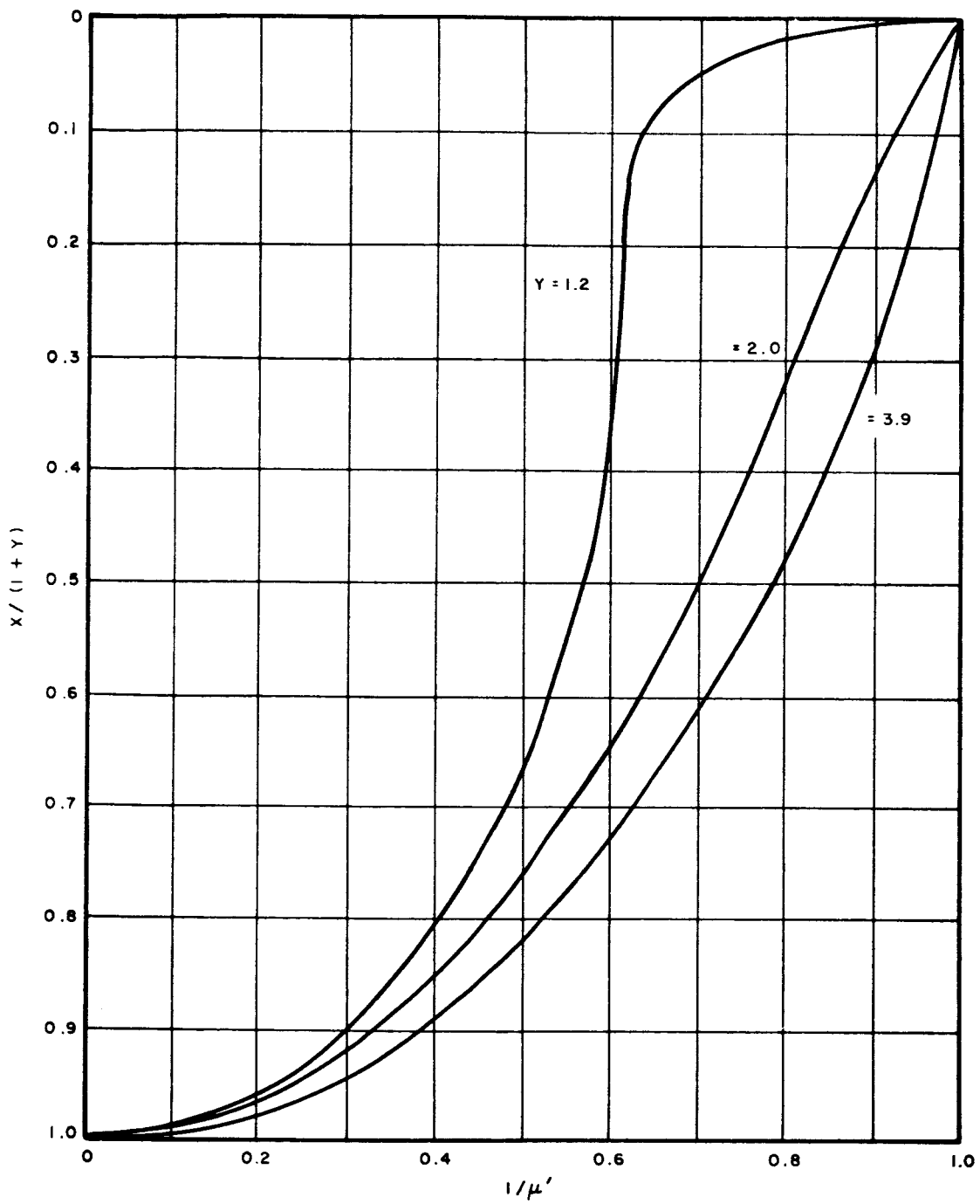
85

FIGURE 30. GROUP REFRACTIVE INDEX (x-WAVE, Y > 1, θ = 45)

FIGURE 31. GROUP REFRACTIVE INDEX (x-WAVE, Y > 1, θ = 90)

$$\mu' = \frac{-X + \frac{X}{1+Y}\left(1 + \frac{Y}{2}\right) + (1+Y)}{(1+Y)\left[1 - \frac{X}{1+Y}\right]^{\frac{1}{2}}}, \quad \theta = 0° \tag{22}$$

At reflection points the refractive index is identically zero and the group refractive index infinite thus causing significant wave delay in this region. Asymptotic expressions near the turning point are given in Appendix I. Although $\mu'$ assumes an infinite value at the turning point, the integrand of the virtual depth integral remains finite.

Figures 23 through 31 show the computed results with the group refractive equation 21 for various parametric values. The angles considered are 0, 10, $23°16'$, 45, and 90 degrees for both the o-and x-waves. The curves are plotted for $1/\mu'$ versus X or $X/(1 \pm Y)$ so that both ordinates and abscissae take on values between zero and unity.

B.   IONOSPHERIC ELECTRON DENSITY PROFILES

Wave delays in a localized region for both components are functions of the region's magnetic field, electron density and electron density gradient. To determine the propagation time delay, it is necessary to specify electron density models to be used for calculating delay times. In the following section, three ionospheric profiles are described. For numerical calculation it was necessary to specify scale heights. The general results nevertheless, are presentable in terms of a general scale height for a single exponential profile and interpretable for more complex profiles.

Two basic electron density profiles, single exponential layer and double exponential layer ionospheres, are considered in order to compute characteristic virtual depth

profiles. The single-layer ionosphere, as well as the lower
layer of the double-layer ionosphere, is assumed to be pro-
duced by ionized oxygen with a scale height of 120 km. A
scale height of eight times that of the lower layer has been
chosen for the upper layer of the double profile. This factor
of eight is obtained by considering a 4 to 1 mixture of ion-
ized hydrogen and helium, respectively.

We will adopt the following designations; $O^+$ for
the single-layer ionosphere and $O^+$, $H_+^+$ for the double-layered
profile. $H_+^+$ represents the ionized mixture assumed for the
upper layer.

The $O^+$, $H_+^+$ ionosphere is considered with and with-
out a region of maximum density, whereas a peak density is
not assigned to the single-layer $O^+$ ionosphere. In the vicin-
ity of a peak density, where used, a parabolic variation is
assumed. Figure 32 shows these profiles plotted as plasma
frequency, rather than density, versus altitude. The dashed
line is the ⊕ ionosphere and the solid line, the $O^+$, $H_+^+$ pro-
file with a region of maximum density. In the computations
the peak density of the $O+$, $H_+^+$ profile is initially neglected
and the plasma frequency is extended exponentially.

These three profiles are described by the following
equations for the electron density N as a function of altitude:

$O^+$ Profile

$$N = 1.22 \times 10^7 \epsilon^{-z/120} \text{ electrons/cc} \qquad (23)$$

$O^+$, $H_+^+$ Profile

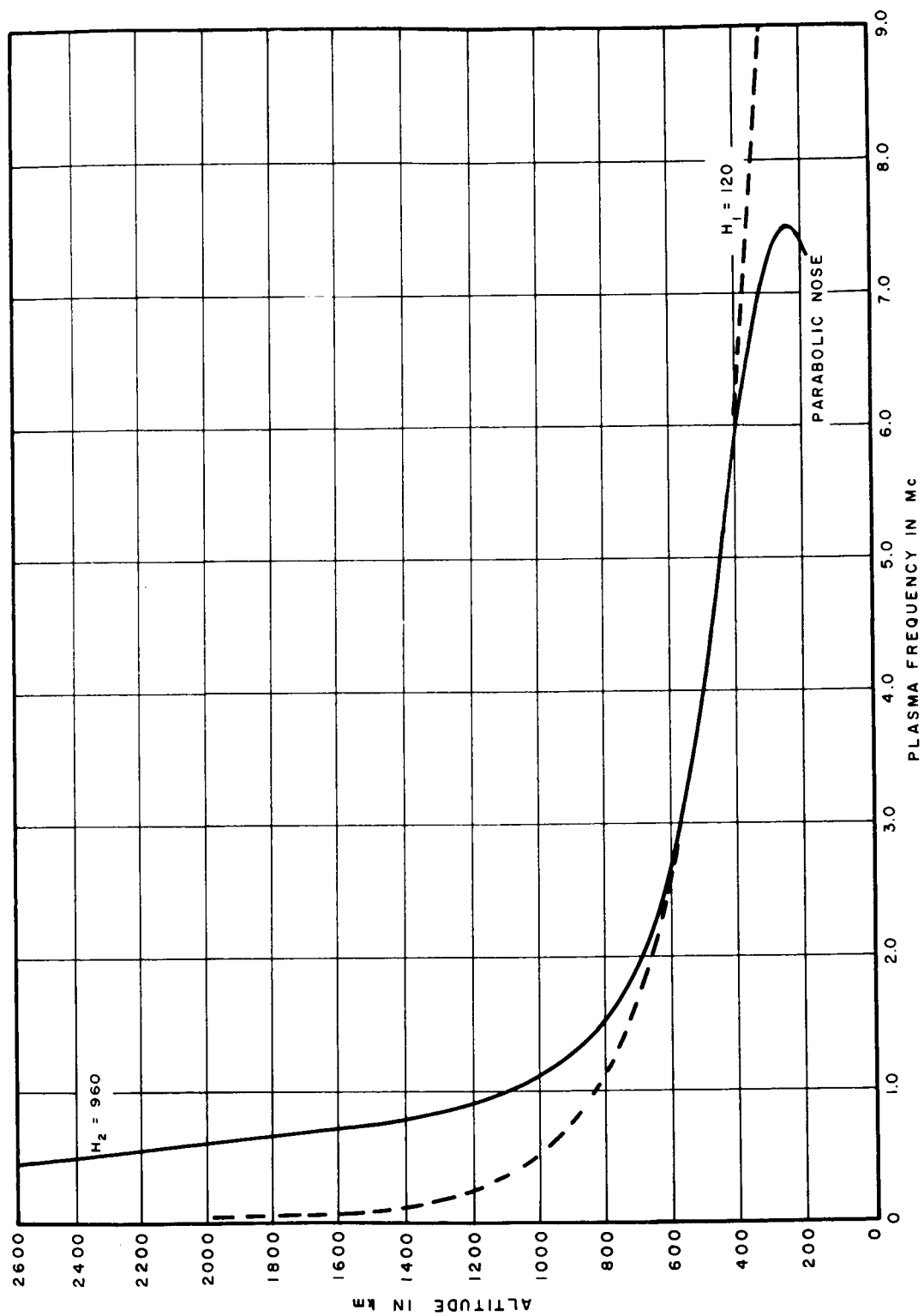$$N = 1.18 \times 10^7 \epsilon^{-z/120} + 3.54 \times 10^4 \epsilon^{-z/960} \text{ electrons/cc} \qquad (24)$$

FIGURE 32.   IONOSPHERIC ELECTRON DENSITY PROFILES

90

for z ≥ 398 km when the peak density is used or for all z
when the peak is not imposed.  For z < 398 km the region of
maximum density is represented by

by

$$N = 6.9 \times 10^5 \left\{ 1 - \left( \frac{z - 250}{240} \right)^2 \right\} \text{electrons/cc} \qquad (25)$$

In the above, z is the altitude in kilometers and 120 and 960
are the electron scale heights for oxygen and the hydrogen
and helium mixture, respectively.

## C.  DIFFERENTIAL VIRTUAL DEPTH

### 1.  DEFINITION OF DIFFERENTIAL VIRTUAL DEPTH

Initially the sounding vehicle is taken as infi-
nitely distant from a planetary ionosphere.  For this con-
figuration, the virtual depth equation for vertical propaga-
tion is given by

$$h'(f) = \int_\infty^{z_t} \mu' dz, \qquad (26)$$

where $\mu'$ = group refractive index, $z_t$ = altitude at which
wave is reflected, z = altitude from planet's surface.
This equation is ambiguious due to the infinite lower limit.
To make the integral tractable, we wish to calculate the
incremental delay due to the ionosphere, which is called the
differential virtual depth.  It is defined as the virtual
depth less the actual profile depth, that is,

$$\Delta h'(f) = \int_\infty^{z_t} (\mu' - 1) dz \qquad (27)$$

91

The lower limit presents no difficulty since it corresponds to free space where the integrand goes to zero. A singularity exists at the upper limit, since it is a turning point, at which point the integrand is infinite. By a suitable transformation of variables, however, the resulting integrand remains finite throughout the integration interval, including the end points.

Equation 27 has been computed numerically by an IBM 1620 computer for both ordinary waves (o-waves) and extraordinary waves (x-waves) propagating vertically through the single- and double-layer ionospheres described in Section 4-B. The form of equation 27 is unsuitable for numerical integration and must be cast into a desirable form by suitable transformations of variables. The transformation that was used defines a variable $\emptyset$ by the relation

$$\sin \emptyset \equiv \frac{f_r}{f}, \tag{28}$$

where $f_r$ is the reflection frequency at any given altitude for the particular wave component under consideration, and f is the sounding frequency. This transformation changes the lower limit to a finite value. The following integrals result from this transformation:

For the o-wave with $\theta \neq 0^{\circ}$, reflecting at X = 1,

$$\sin \emptyset \equiv \frac{f_N}{f} \tag{29}$$

and

$$\Delta h'(f) = \int_0^{\pi/2} (\mu_0' - 1)\frac{dz}{df_N} f \cos \emptyset d\emptyset \tag{30}$$

For the longitudinal wave at $\Theta = 0°$, reflecting at $X = 1 + Y$,

$$\sin \phi \equiv \frac{f_o}{f}, \qquad (31)$$

where $f_o$ is given by

$$f_o = \frac{1}{2}\left[(f_H^2 + 4f_N^2)^{\frac{1}{2}} - f_H\right], \qquad (32)$$

and

$$\Delta h'(f) = \int_o^{\pi/2} (\mu'_o - 1)\frac{dz}{df_N}\frac{\sqrt{f_H^2 + 4f_N^2}}{2f_N} f \cos \phi d\phi. \qquad (33)$$

For the x-wave with $Y<1$, reflecting at $X = 1 - Y$,

$$\sin \phi \equiv \frac{f_x}{f}, \qquad (34)$$

where

$$f_x = \frac{1}{2}\left[(f_4^2 + 4f_N^2)^{\frac{1}{2}} + f_H\right], \qquad (35)$$

and

$$\Delta h'(f) = \int_{\sin^{-1}\frac{f_H}{f}}^{\pi/2} (\mu'_x - 1)\frac{dz}{df_N}\frac{\sqrt{f_H^2 + 4f_N^2}}{2f_N} f \cos \phi d\phi. \qquad (36)$$

For the x-wave with $Y > 1$, reflecting at $X = 1 + Y$,

$$\sin \phi \equiv \frac{f_x'}{f}, \tag{37}$$

where

$$f_x' = \frac{1}{2}\left[(f_H^2 + 4f_N^2)^{1/2} - f_H\right], \tag{38}$$

and

$$\Delta h'(f) = \int_0^{\pi/2} (\mu_x' - 1)\,\frac{dz}{df_N}\,\sqrt{\frac{f_H^2 + 4f_N^2}{2f_N}}\,f\cos\phi\,d\phi. \tag{39}$$

The indices of refraction $\mu_o'$ and $\mu_x'$, for the o- and x-waves respectively, are computed from equations 21 and 22. The derivative $dz/df$ is determined by differentiating the plasma frequency altitude distribution function. For a single exponential profile, equation 23, with an electron scale height H, the derivative is

$$\frac{dz}{df_N} = -\frac{2H}{f_N(z)} \tag{40}$$

The double-layer expression gives

$$\frac{dz}{df_N} = \frac{-2f_p(z)}{\dfrac{f_1^2(z)}{H_1} + \dfrac{f_2^2(z)}{H_2}} \tag{41}$$

where

$$f_1(z) \doteq 31 \times 10^3\,\epsilon^{-z/2H_1}\ \text{Mc}, \qquad H_1 = 120$$

$$f_2(z) \doteq 1.69\,\epsilon^{-z/2H_2}\ \text{Mc}, \qquad H_2 = 960$$

and

$$f_p(z) = \sqrt{f_1^2 + f_2^2}$$

94

In the vicinity of the peak density at heights above the peak level

$$\frac{dz}{df_N} = -\frac{4H_1^2}{f_{nm}^2} \frac{f_N(z)}{(z - z_m)}$$

where

$$f_{nm}^2 = 81N_m \ (kc)^2$$

$$f_N(z) = 9\left[ N_m \left\{ 1 - \left|\frac{z - z_m}{2H_1}\right|^2 \right\} \right]^{\frac{1}{2}} kc \qquad (42)$$

$$N_m = \frac{2N_o}{\sqrt{5} - 1} \ \epsilon \frac{-z_m}{H_1} - (\sqrt{5} - 1) \ electrons/cc$$

$$N_o = 1.2 \times 10^7 \ electrons/cc$$

$$z_m = 250 \ km$$

At the lower limits, where $\emptyset$ is either 0 or $\sin^{-1} \frac{f_H}{f}$, depending on wave type, the sounder is at infinity and hence $dz/df_N$ is infinite. This infinity is removed when the group refractive index is defined to be unity ($\mu' = 1$) at this point. Another infinity is introduced at the upper limit $\emptyset = \pi/2$, the turning point, where $\mu'$ is infinite for both o- and x-waves. However, $\cos \emptyset$ is zero at the upper limit and the product of $\mu' \cos \emptyset$ remains finite.

Appendix I shows that $\mu'$ cos $\emptyset$ is finite at the reflection point. The expressions also provide checks for computer programs to perform the integration. The integrands of equations 30, 31, 36, and 39 are finite within the entire integration interval and the integrals converge.

Figure 33 shows $(\mu'_x - 1)$ cos $\emptyset$ versus $\emptyset$ for an x-wave propagating at angles of 10 and 90 degrees with respect to the magnetic field for $Y = 2$. Finite end points are displayed at $\emptyset = \pi/2$. The peaking of the 10-degree curve corresponds to the peak in $\mu'$ shown in Figure 29.

2. INTEGRANDS OF DIFFERENTIAL VIRTUAL DEPTH INTEGRALS

It is instructive to examine the integrands prior to performing the integration. Figure 34 shows two integrands for an o-wave in an $O^+$, $H_+^+$ ionosphere for two different sounding frequencies. Both curves have zero values at $\emptyset = 0$ and possess a spike in the vicinity of $\emptyset = \pi/2$. These results are typical. The rapid increase in $\mu'$ near the turning point causes a spike at $\emptyset = \pi/2$ in all integrands for o- and x-waves in all the ionospheric models. Since a wave will spend an appreciable amount of delay time near a turning point this result is not unexpected.

Figure 35 compares integrands for the single- and double-layer profiles. Several aspects are interesting. First, the $O^+$, $H_+^+$ curve has a peak within the transistion region between exponentials. Following this peak the $O^+$, $H_+^+$ integrand approaches the $O^+$ curve and then finally merges with it. The intermediate peak in the $O^+$, $H_+^+$ profile results from the greater scale height at higher altitudes. For sufficiently high altitudes, the $O^+$, $H_+^+$ profile may be described by the hydrogen-helium mixture, which has a derivative $dz/df$
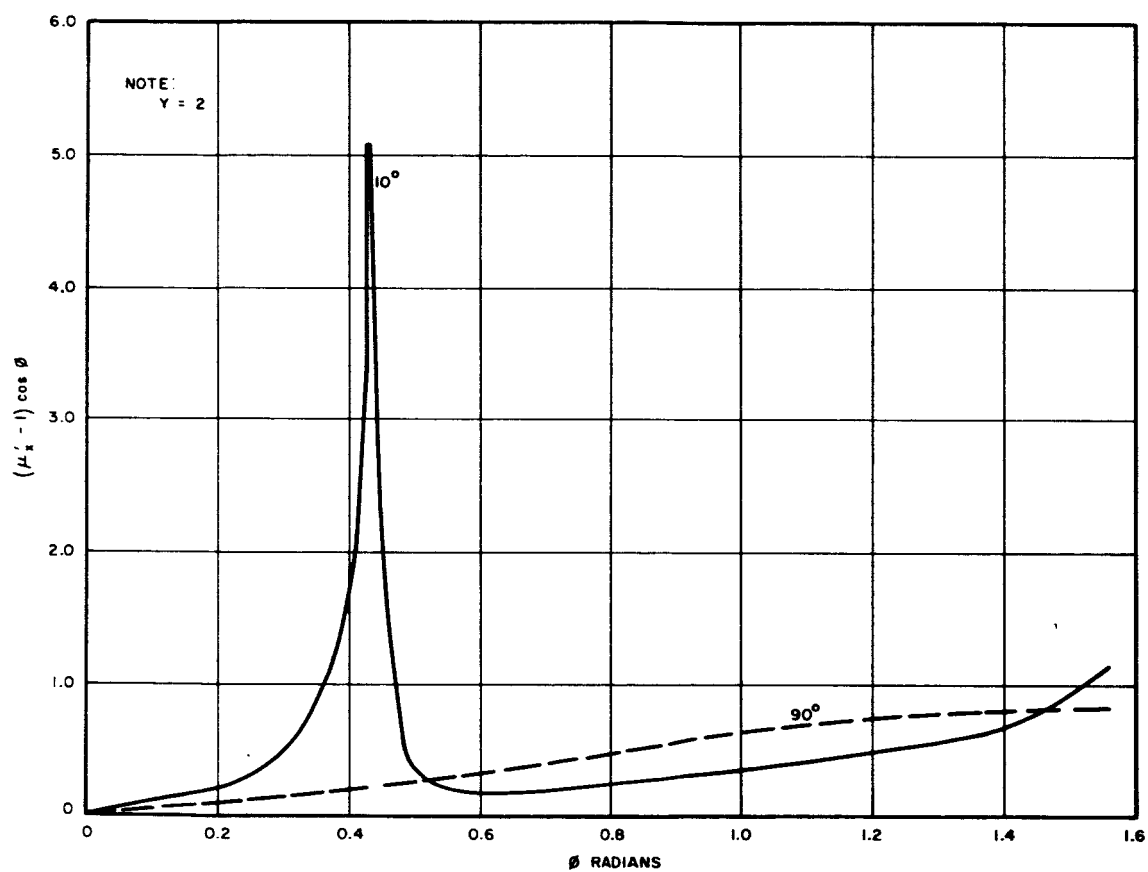
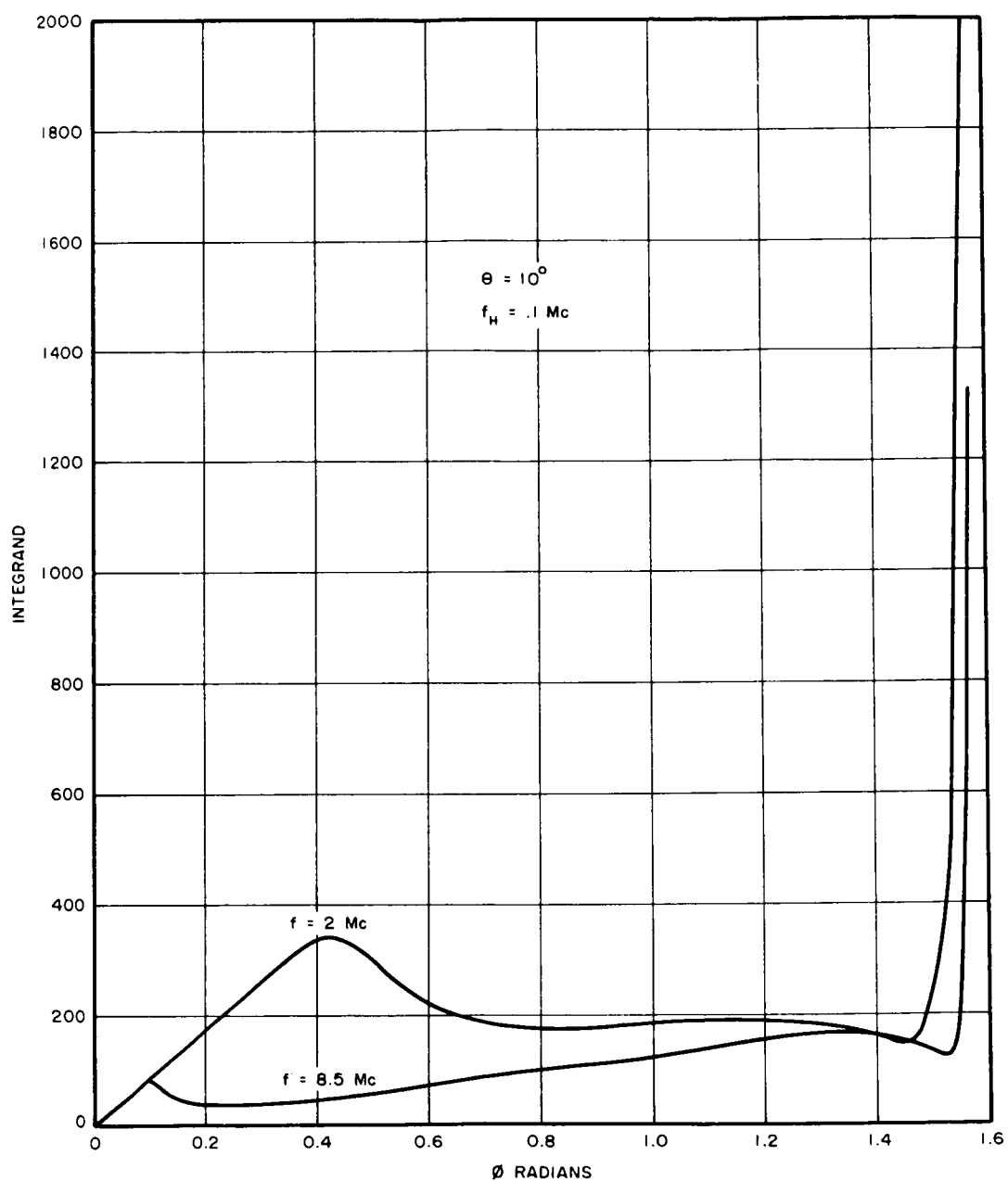FIGURE 33.   FINITE BEHAVIOR OF $(\mu'_x - 1) \cos \theta$

FIGURE 34.   COMPARISON OF INTEGRANDS FOR o-WAVE
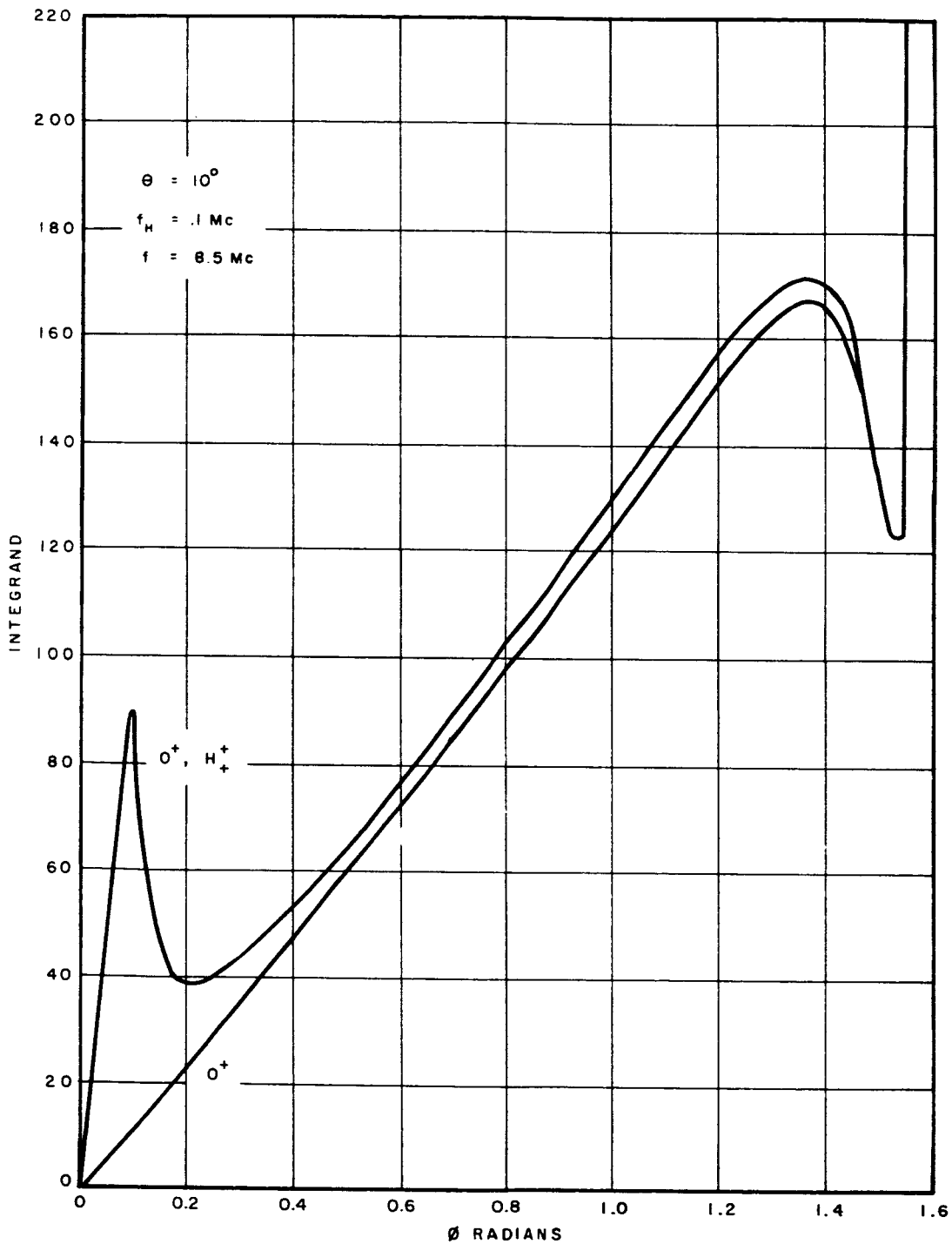PROPAGATING IN DOUBLE-LAYER IONOSPHERE

98

FIGURE 35.  COMPARISON OF INTEGRANDS FOR o-WAVE
PROPAGATING IN SINGLE AND DOUBLE-LAYER
IONOSPHERES

99

eight times greater than the $O^+$ profile at a given altitude. Furthermore, $\mu'$ is increased due to the greater electron density of this profile. When the o-wave has descended through the transition region between both layers, the behavior corresponds to that of the $O^+$ ionospheric profile.

Integrands for the x-wave path shown in Figure 36 are quite different from the previous o-wave integrands, especially for the case where Y>1. This condition creates a large spike in the integrand at the point X ≈ 1 which coincides with a maximum of $\mu'$ (i.e. large delay time). As before, the differences between the single and double profile may be accounted for by increases in $\mu'$ and profile slope for a given altitude. The spikes for the case Y = 3.9 are large and have peak values of about 1000.

The differential virtual depth thus calculated for the o- and x-waves must be added to the actual electron density profile in order to obtain the virtual depth profile.

### 3. DIFFERENTIAL VIRTUAL DEPTHS

Differential virtual depths were computed for various conditions and the results are presented and discussed in this section. For the single exponential ionosphere, low- and high-frequency limits are simply relatable to the scale height. In a double-layer ionosphere, waves are delayed in the upper region almost as though that were the only region. In the lower region they are similarly delayed as by a single layer. The complete curve lies between the single exponential curves corresponding to the scale heights of the two regions ($O^+$ and $H_+^+$ layers).

Results are first given for infinitely extending single- and double-layer profiles. These serve as basic models upon which comparisons may be made. A peak density region is then added and the results that are obtained are contrasted with the infinite profiles.
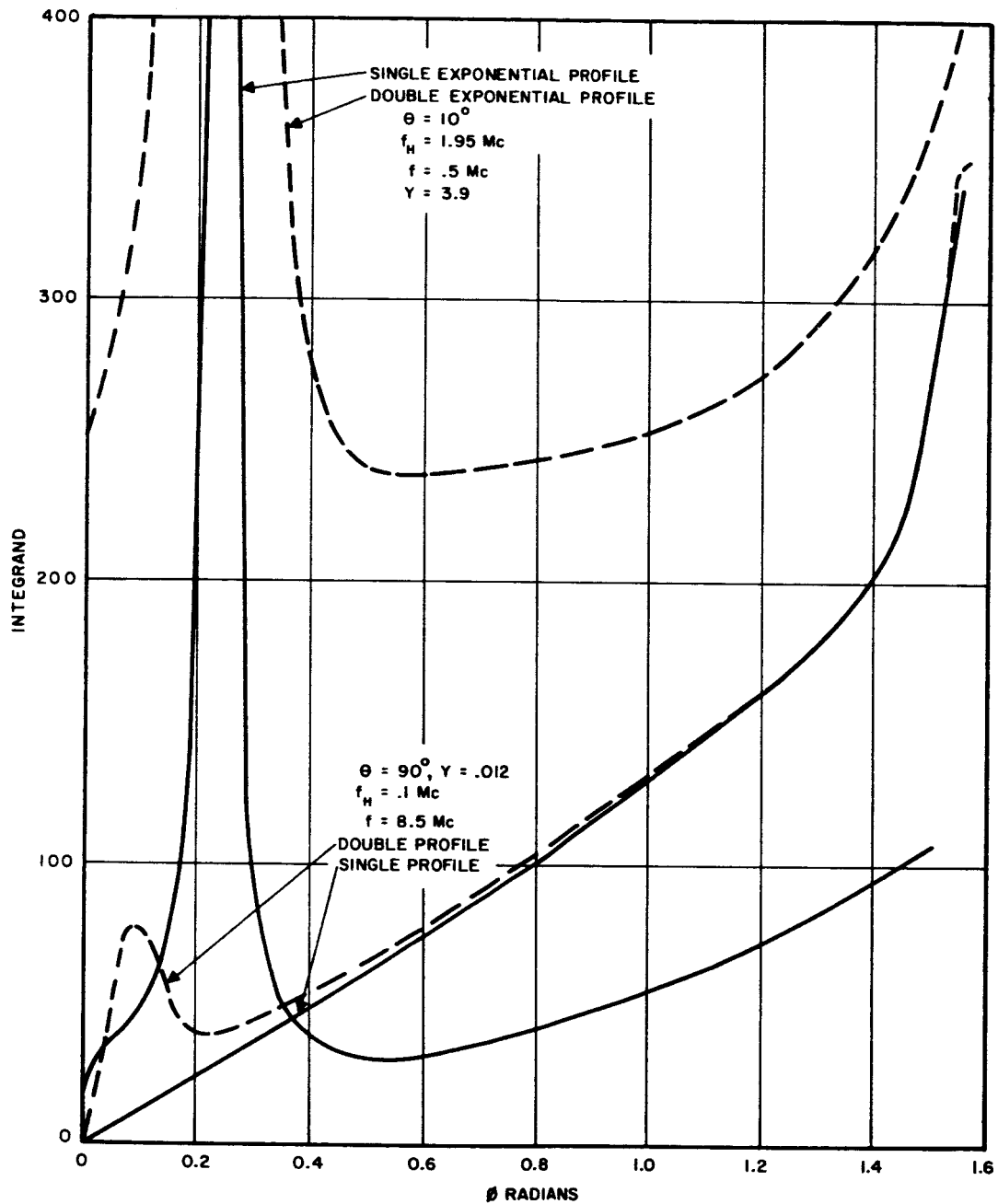
FIGURE 36. COMPARISON OF INTEGRANDS FOR x-WAVE PROPAGATING IN SINGLE AND DOUBLE-LAYER IONOSPHERES

### a.   O-WAVE IN SINGLE-LAYER PROFILE ($\theta \neq 0^{\circ}$)

For a single-layer profile, equation 30 may be
rewritten by substituting equation 40 for the derivative
$dz/df_N$

$$\frac{\Delta h'(f)}{H} = -\int_{0}^{1} \left[ \mu_0'(X,Y,\theta) - 1 \right] d\,(\ln X). \tag{43}$$

43 is independent of X upon integration and for a
given angle ($\theta$) is only a function of Y.

Figure 37 summarizes the results showing $\frac{\Delta h'(f)}{H}$
versus Y for four different angles--10, 25, 55, and 90 degrees.
Figures 38 and 39 provide examples of differential virtual
depth versus sounding frequency for the two gyro-frequencies
0.1 Mc and 1.95 Mc for a scale height of 120 km.

At $\theta$ = 90 degrees, the differential virtual depth
can be shown to have a constant value -2H ln 2 which in terms
of the virtual depth means that it will have exactly the same
shape (same scale height) as the actual electron density pro-
file but displaced by $\Delta h'$ km.  This is to be expected since
an o-wave propagating transversly to the magnetic field prop-
agates as if in an isotropic plasma.  The plasma becomes
isotropic also in the high-frequency limit (Y = 0).  There-
fore, the $\Delta h'/H$ curves in Figure 37 terminate at the trans-
verse value of -2 ln 2 and in Figures 38 and 39 they are shown
to approach this value asymptotically.

Figure 40 is a plot of the low-frequency asymptotic
limit as a function of $\theta$.  The results are normalized to the
scale height.  The appropriate relationships are derived in
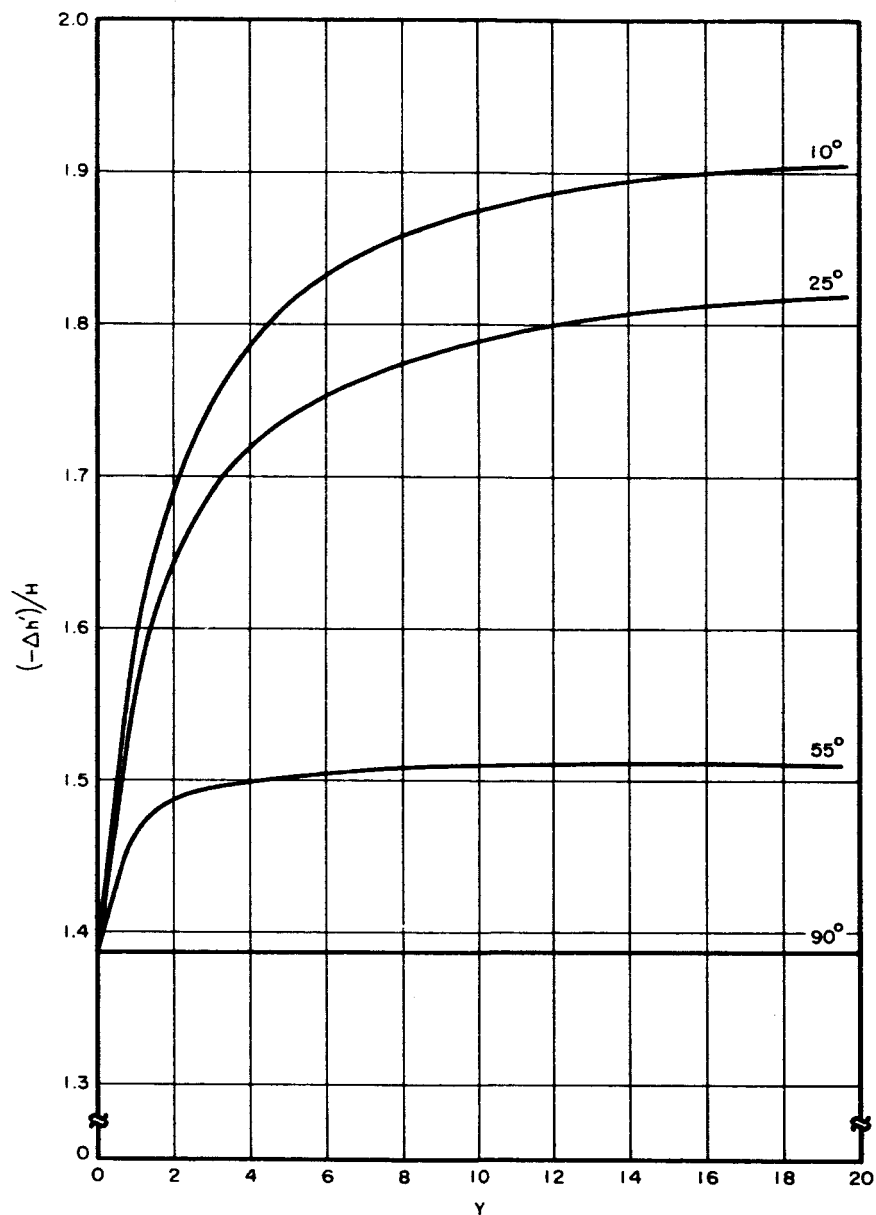Appendix II.  The low-frequency asymptotic limits for all

FIGURE 37.  DIFFERENTIAL VIRTUAL DEPTH OF o-WAVE IN
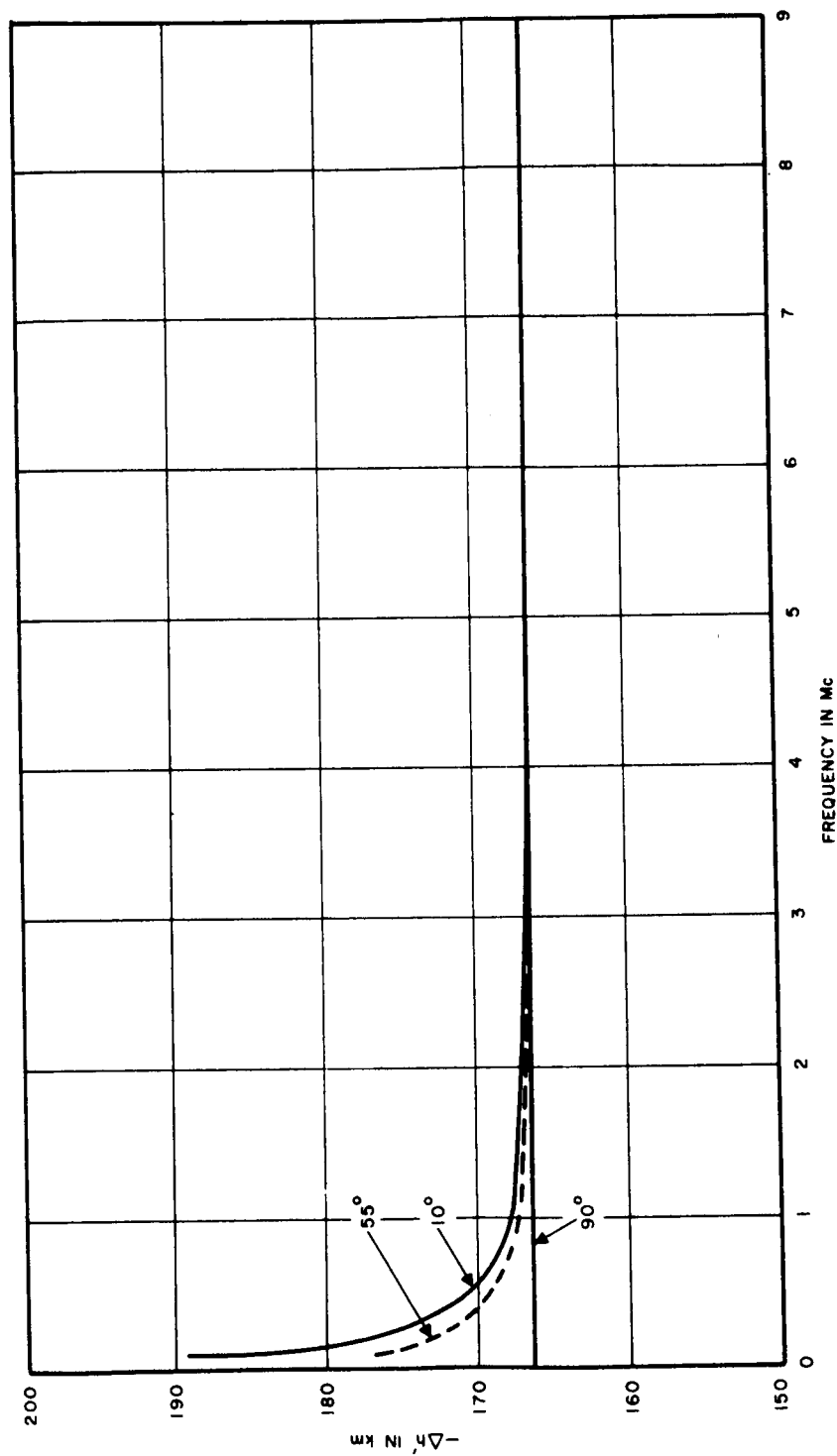            SINGLE-LAYER IONOSPHERE WITH SCALE HEIGHT  H

FIGURE 38.   DIFFERENTIAL VIRTUAL DEPTH OF o-WAVE IN
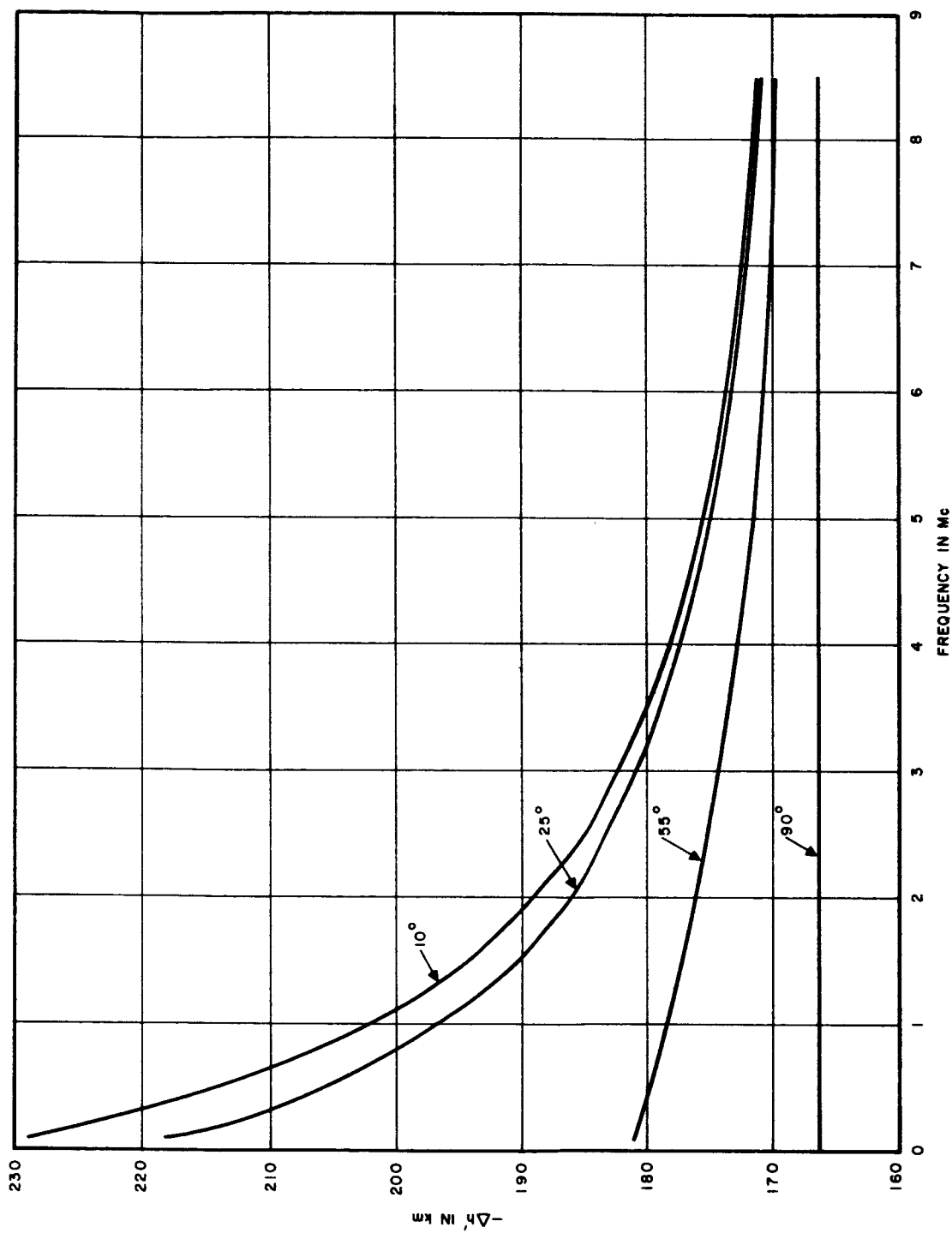SINGLE-LAYER IONOSPHERE WITH $f_H = 0.1$ Mc

FIGURE 39. DIFFERENTIAL VIRTUAL DEPTH OF o-WAVE IN SINGLE-LAYER IONOSPHERE WITH $f_H = 1.95$ Mc
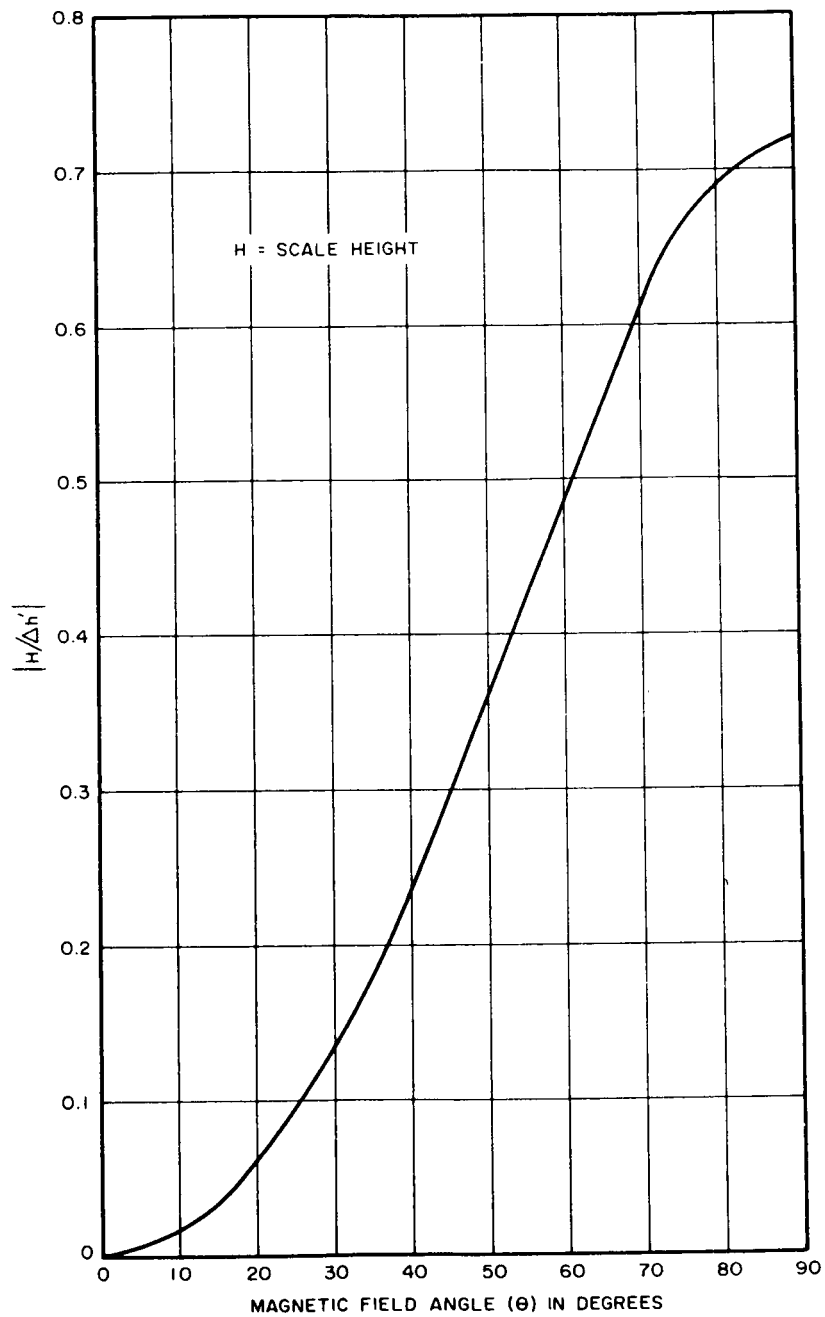
105

FIGURE 40.   ASYMPTOTIC LOW-FREQUENCY LIMIT OF DIFFERENTIAL
VIRTUAL DEPTH FOR o-WAVE

106

angles are also shown in Figure 37. When $\theta = 0$ degree, the longitudinal wave reflection is taken at $X = 1 + Y$, and a separate evaluation of the asymptotic limit of $\Delta h'(f)$ must be made. The derivation for this angle is presented in Appendix III.

b. X-WAVE IN SINGLE-LAYER PROFILE

The differential virtual depth for an x-wave propagating through a single exponential profile is given by

$$\frac{\Delta h'(f)}{H} = \int_0^{1 \pm Y} \left[\mu'_x(X,Y,\theta) - 1 \quad d\right](\ln X) \qquad (44)$$

where the plus sign in the upper limit is used when $Y > 1$ and the minus sign when $Y < 1$. As in the previous action, the differential virtual depth depends only on Y and $\theta$.

Figure 41 shows $\Delta h'/H$ plotted against Y for various values of $\theta$. When $Y < 1$, the variation with $\theta$ is very small as exhibited by the 0 and 90-degree curves. For $Y > 1$, the angular dependence is more pronounced; $\theta = 0$ has been omitted for $Y > 1$ because there is no ionospheric reflection of this wave $(1 - Y < 0)$. When $Y = 0$, $\Delta h'$ takes the isotropic value $-2H \ln 2$. As the sounding frequency approaches zero $(Y \longrightarrow \infty)$ asymptotic limits are found. The relationships are derived in Appendix IV and $\Delta h'/H$ is plotted versus $\theta$ in Figure 42.

Figures 43 and 44 exhibit these results as plots of $\Delta h'$ versus sounding frequency for various values of the gyrofrequency. Figure 43, which is for $Y < 1$, is labeled $\theta = 0 - 90$ degrees, since there is very little variation of $\Delta h'$ with angle in this range. When $Y > 1$ the angular dependence is significant. Only $\theta = 90$ degrees is shown in Figure 44.
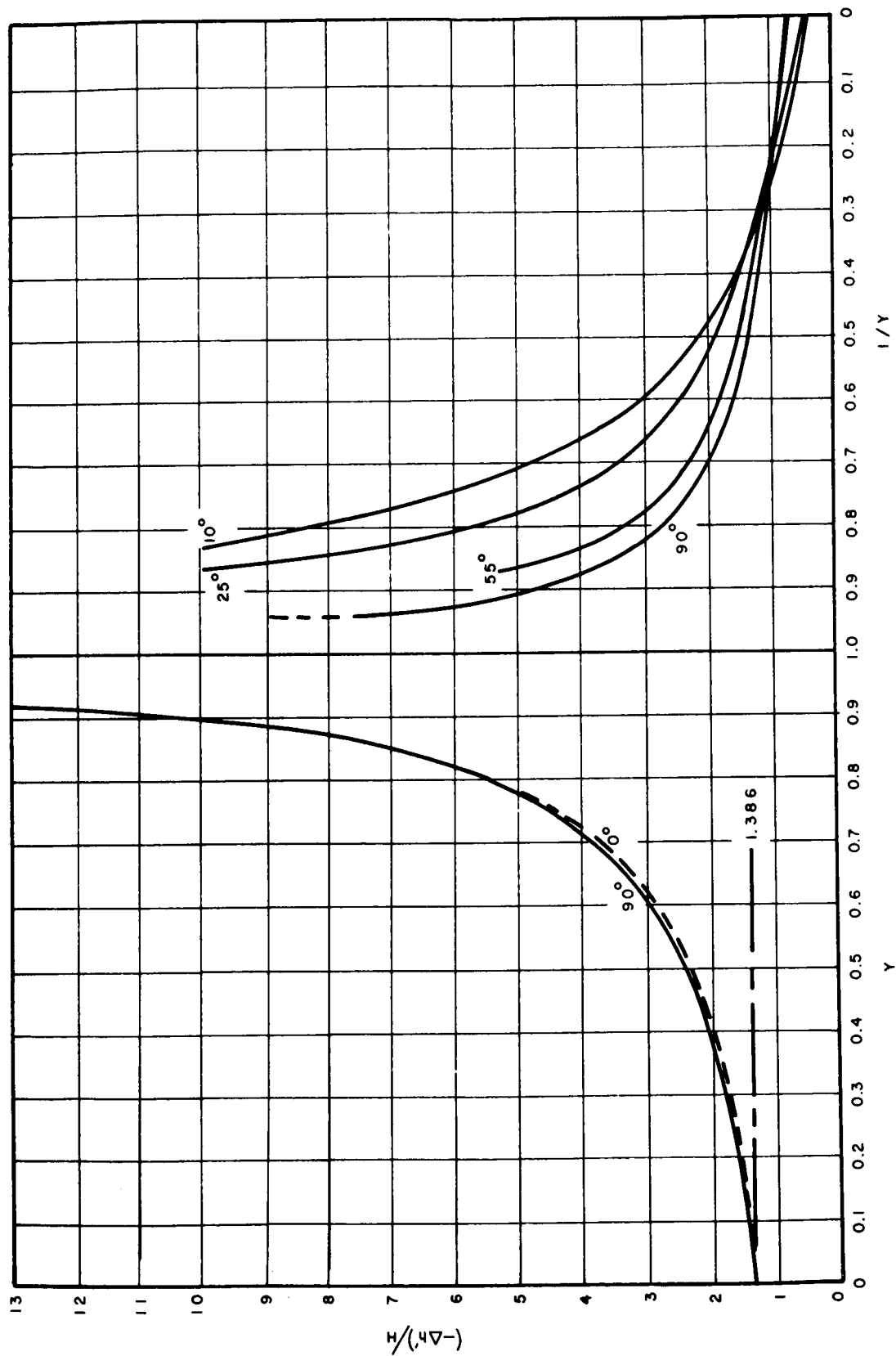
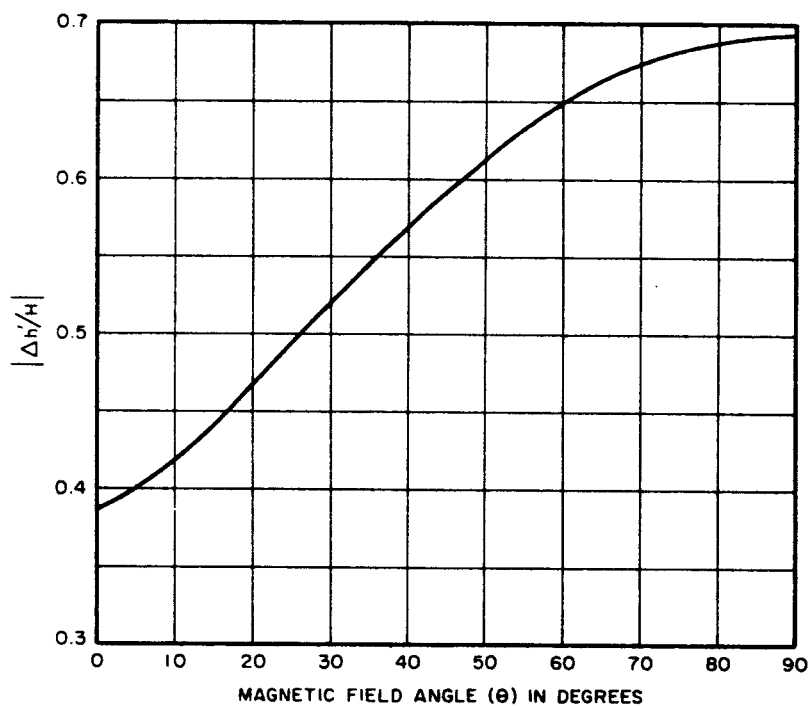FIGURE 41. DIFFERENTIAL VIRTUAL DEPTH OF x-WAVE IN SINGLE-LAYER IONOSPHERE WITH SCALE HEIGHT H

FIGURE 42.   ASYMPTOTIC LOW-FREQUENCY LIMIT OF DIFFERENTIAL
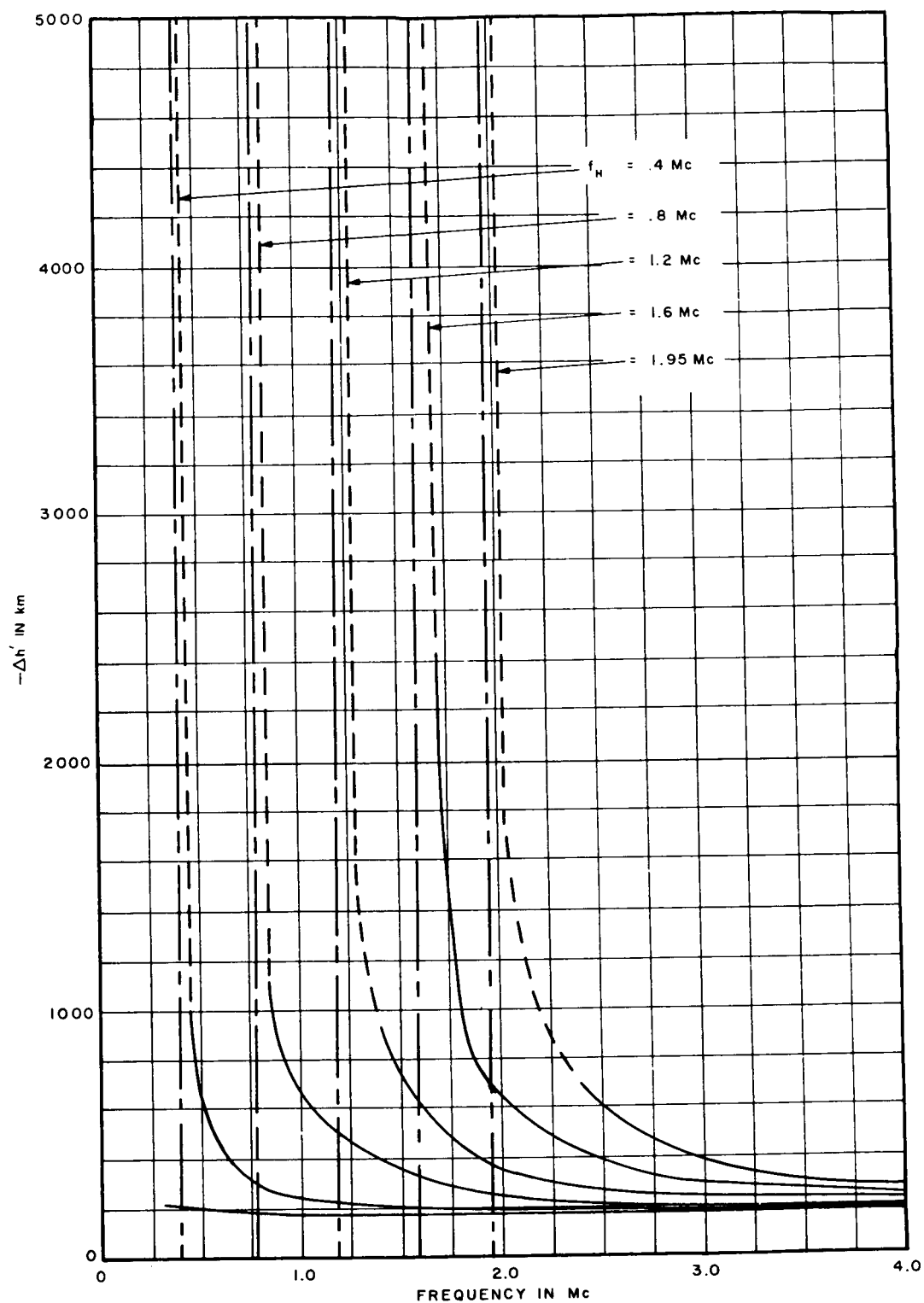VIRTUAL DEPTH FOR x-WAVE

FIGURE 43. DIFFERENTIAL VIRTUAL DEPTH FOR x-WAVE IN
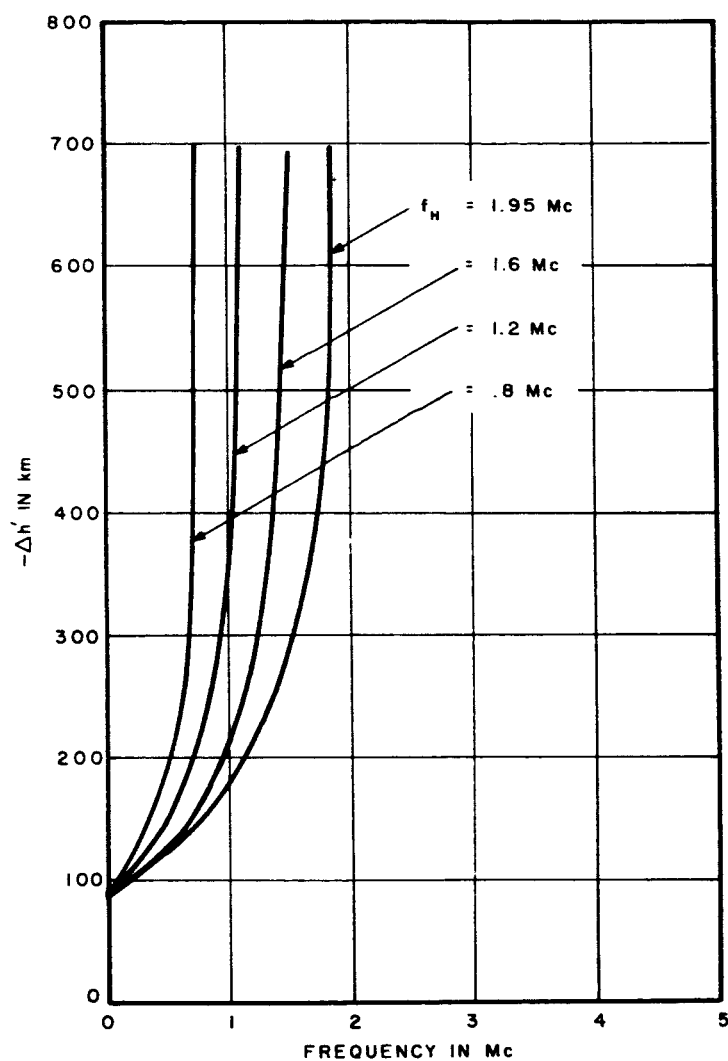SINGLE-LAYER IONOSPHERE ($\theta = 0 - 90$, $Y < 1$)

110

FIGURE 44.    DIFFERENTIAL VIRTUAL DEPTH FOR x-WAVE IN
SINGLE-LAYER IONOSPHERE ($\theta$ = 90, Y > 1)

### c. O-WAVE IN DOUBLE-LAYER PROFILE

Differential virtual depths for the double-layer profile described in Section 2 have been computed to demonstrate the manner in which each layer affects wave delay time. The scale heights considered are 120 and 960 km for the lower and upper layers, respectively. The double-layer results are compared with the single-layer behavior of each region using the results of the previous section.

Figures 45, 46, and 47 display the manner in which double-layer differential virtual depths are bounded by the single-layer results which are shown as dashed lines in the figures. The transition region between the two single exponential extremes actually corresponds to the transition region of the true electron density profile.

The differential virtual depth transition region is greatly accentuated in the case of a longitudinal wave as shown in Figure 48. Curves for gyro-frequencies of 0.5 and 1.95 Mc are shown. Peak amplitude decreases with increasing gyro-frequency and no peaking would occur in the limiting case of an infinite gyro-frequency. The terminating value of $\Delta h'$ at $f = 0$ corresponds to the infinite Y parameter value derived in Appendix III.

### d. X-WAVE IN DOUBLE-LAYER PROFILE

The differential virtual depths plotted in Figures 49 through 53 resonate at the various gyro-frequencies shown in the figure. Values from 0.1 to .95 Mc are considered for propagation angles of 0, 10, 25, 55, and 90 degrees.

For longitudinal propagation there is no reflection for an x-wave when $Y > 1$. In an actual sounding experiment, penetration and surface reflections from the planet would be expected. However, planetary surface reflections have not been considered as part of this propagation study, and,

112

FIGURE 45.   DIFFERENTIAL VIRTUAL DEPTH FOR o-WAVE IN
DOUBLE-LAYER IONOSPHERE ($\Theta$ = 10)

FIGURE 46. DIFFERENTIAL VIRTUAL DEPTH FOR o-WAVE IN DOUBLE-LAYER IONOSPHERE ($\theta = 25$)

114

FIGURE 47.    DIFFERENTIAL VIRTUAL DEPTH FOR o-WAVE IN
DOUBLE-LAYER IONOSPHERE ($\theta$ = 90)

FIGURE 48.  DIFFERENTIAL VIRTUAL DEPTH FOR LONGITUDINAL
WAVE IN DOUBLE-LAYER IONOSPHERE

116

FIGURE 49.    DIFFERENTIAL VIRTUAL DEPTH FOR x-WAVE IN
DOUBLE-LAYER IONOSPHERE ($\theta = 0$)

117

FIGURE 50. DIFFERENTIAL VIRTUAL DEPTH FOR x-WAVE IN DOUBLE-LAYER IONOSPHERE ($\theta$ = 10)
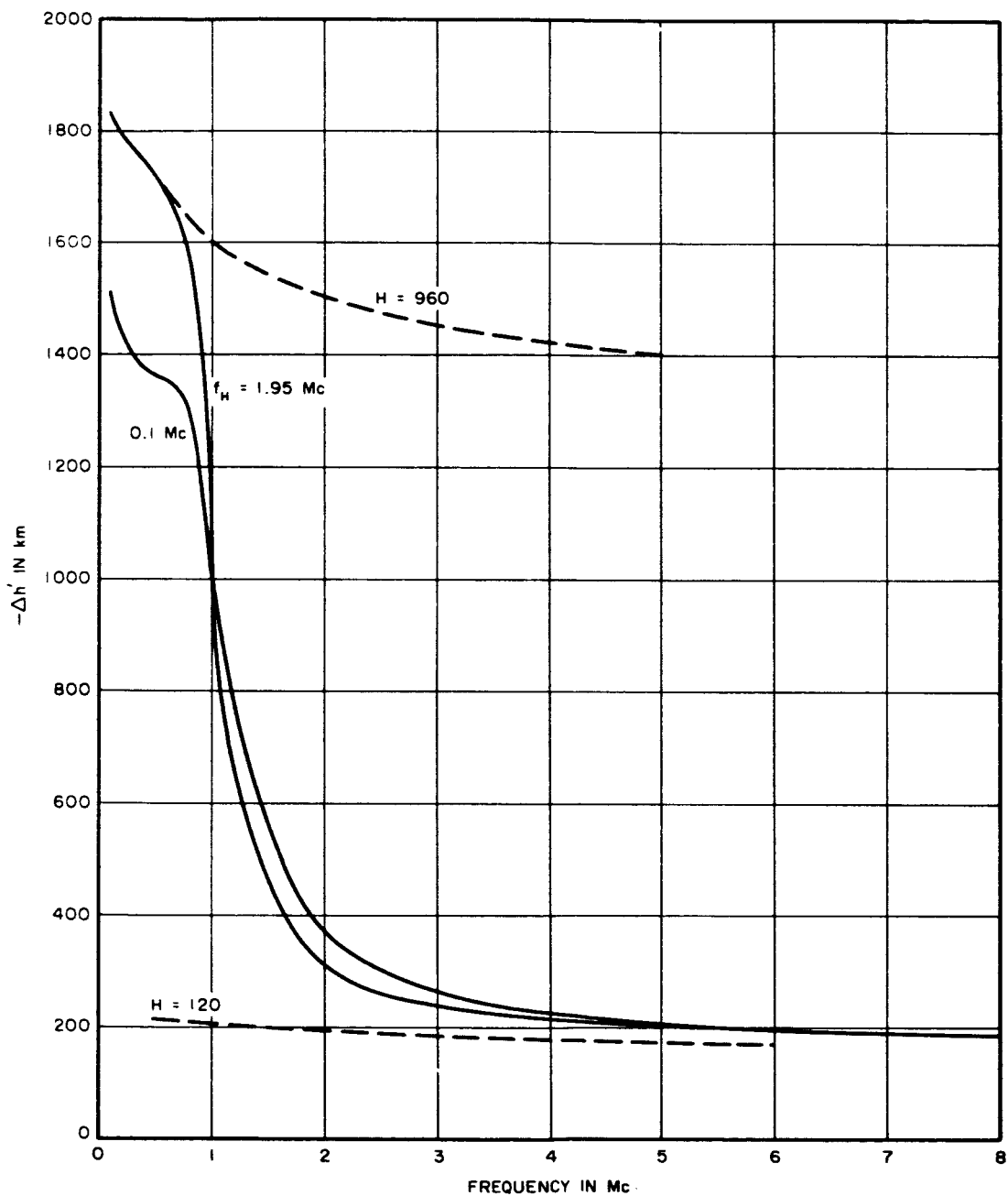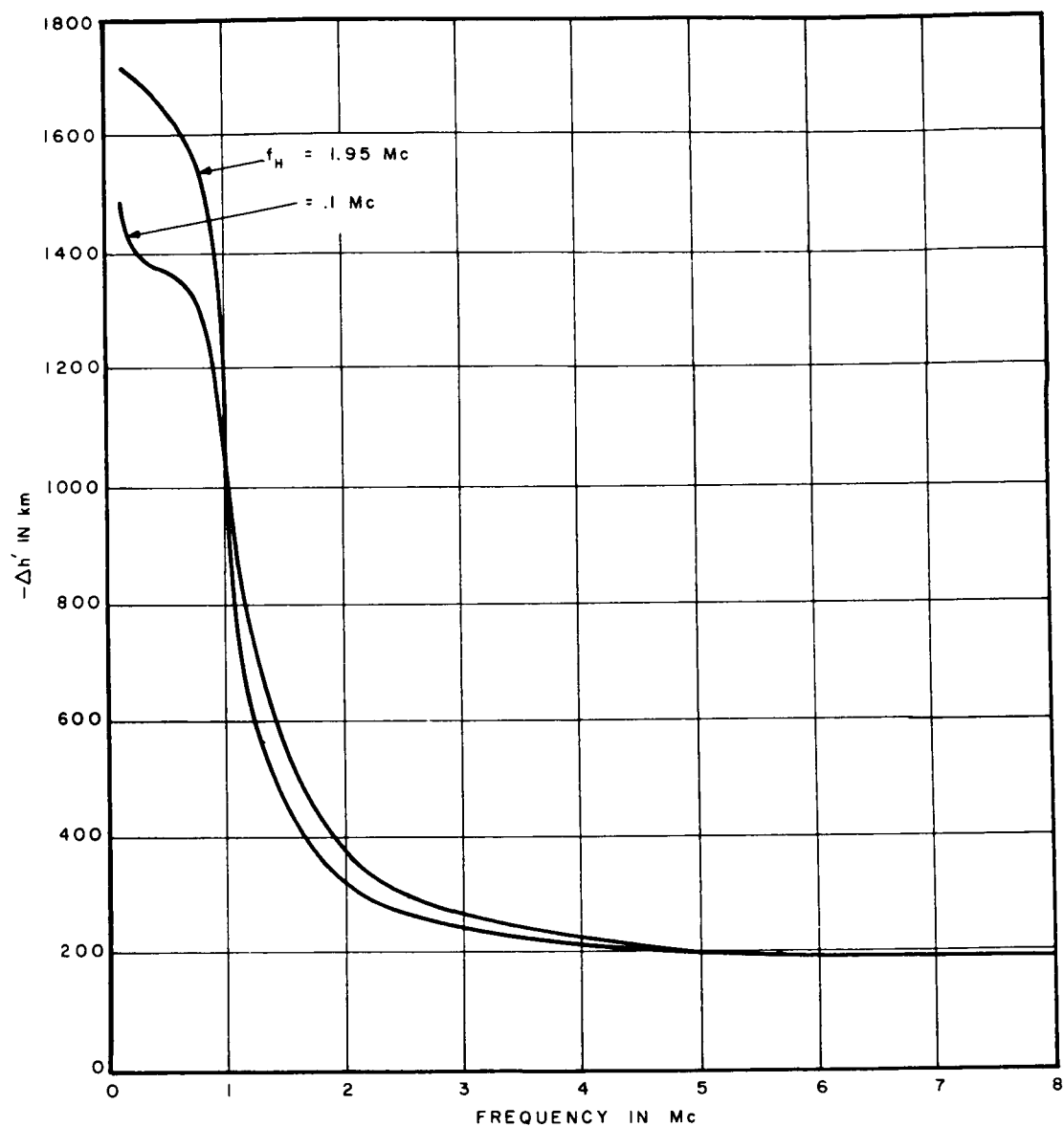
118

FIGURE 51.   DIFFERENTIAL VIRTUAL DEPTH FOR x-WAVE IN
             DOUBLE-LAYER IONOSPHERE ($\theta$ = 25)

FIGURE 52. DIFFERENTIAL VIRTUAL DEPTH FOR x-WAVE IN
DOUBLE-LAYER IONOSPHERE ($\theta = 55$)

120

FIGURE 53. DIFFERENTIAL VIRTUAL DEPTH FOR x-WAVE IN
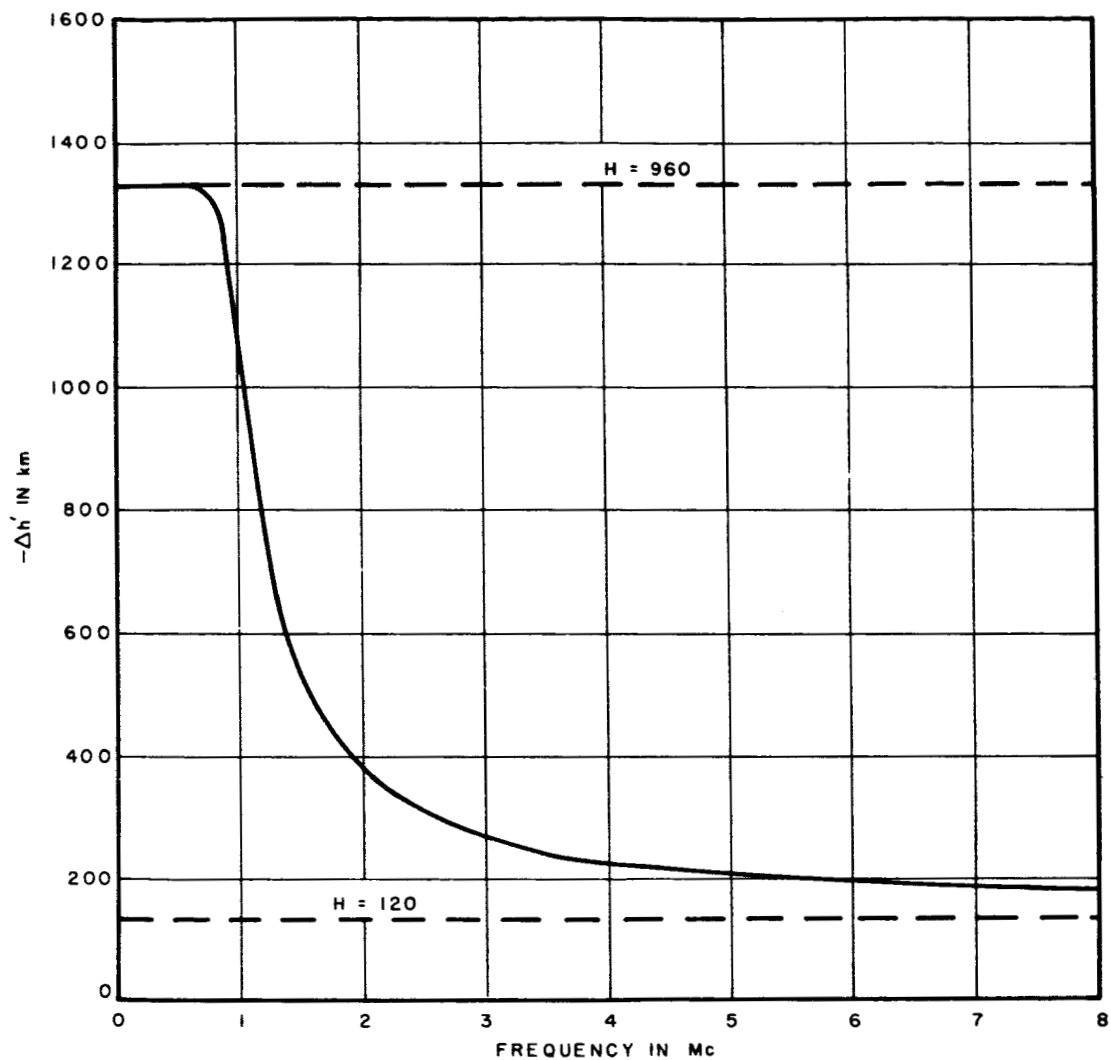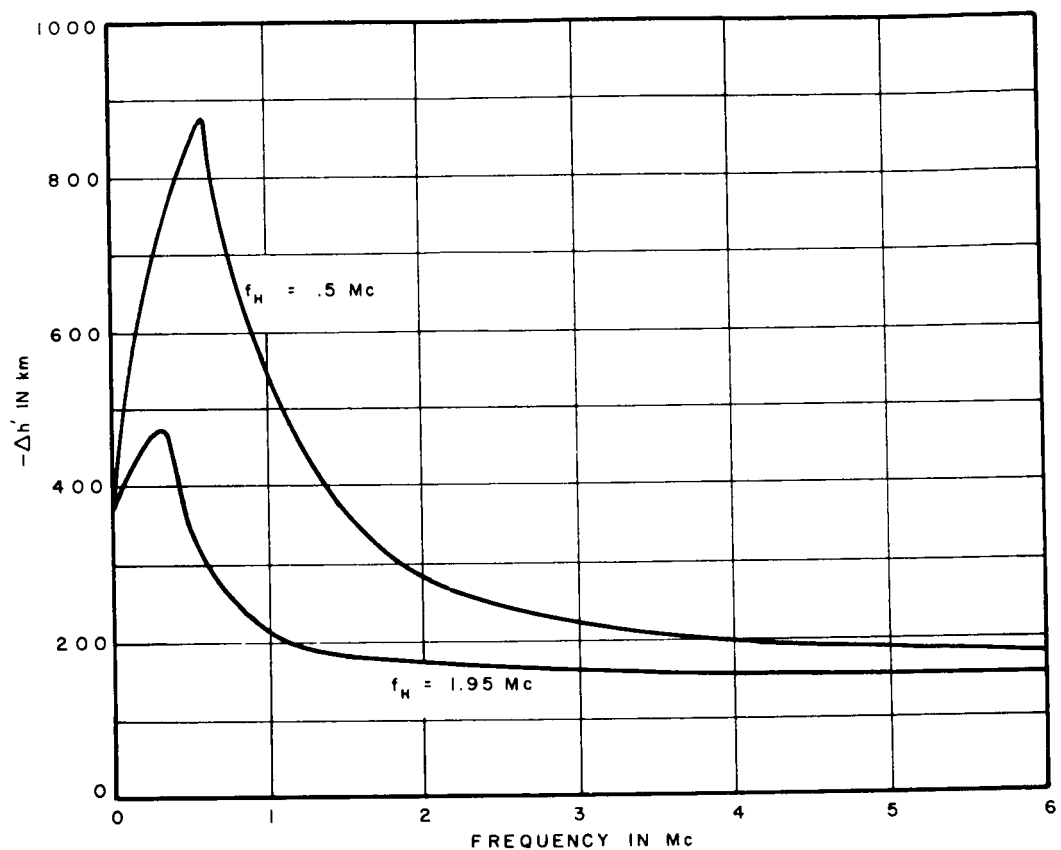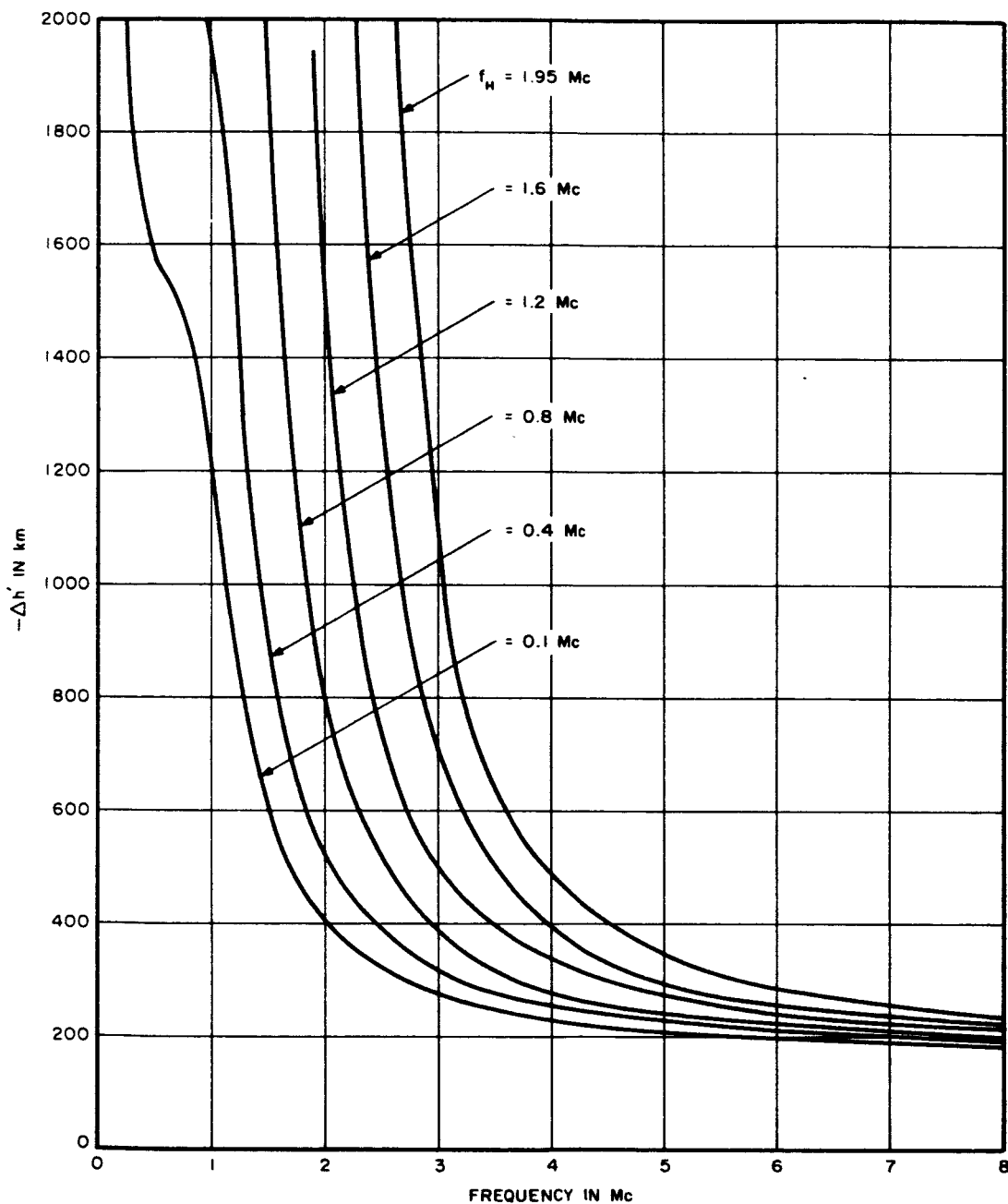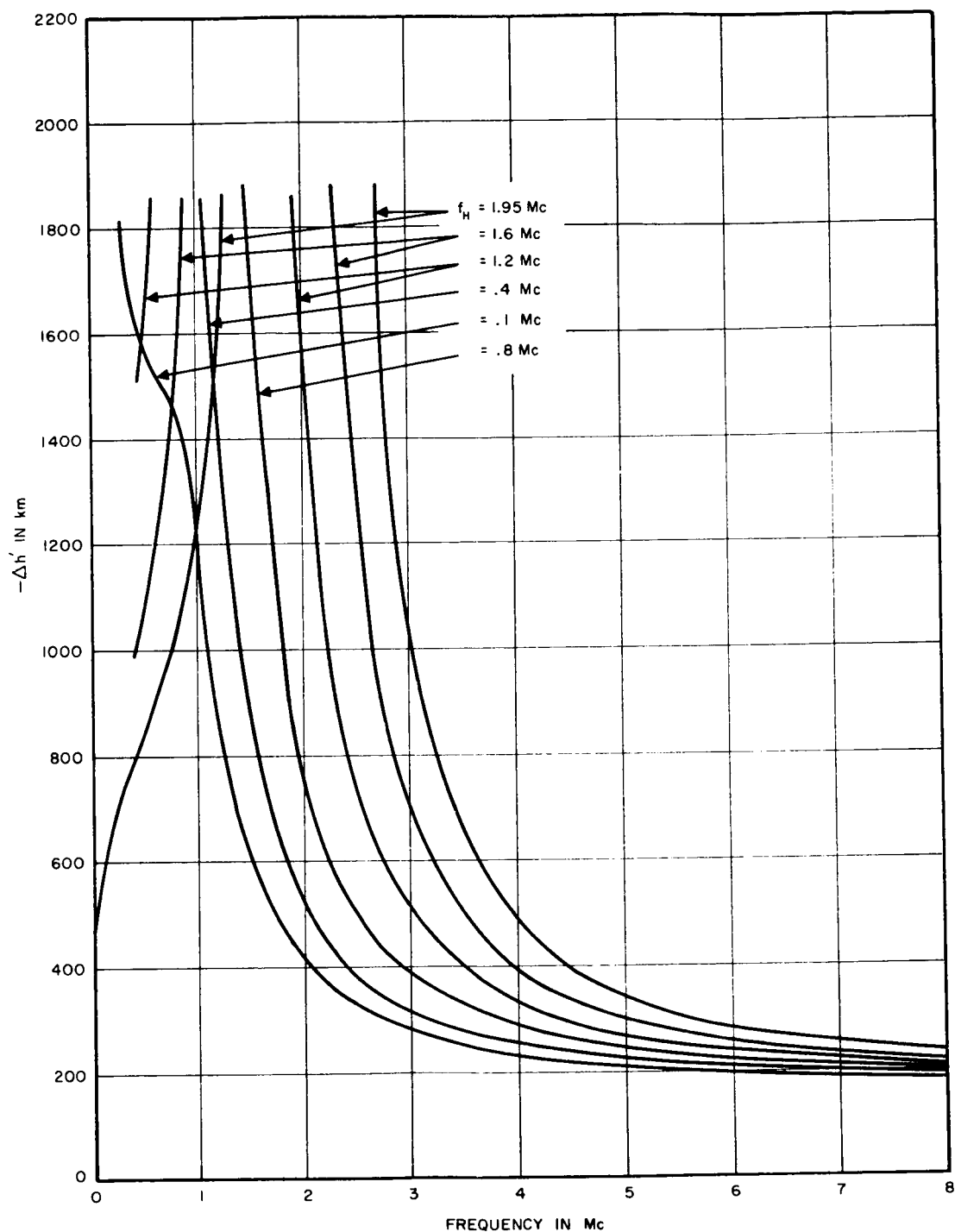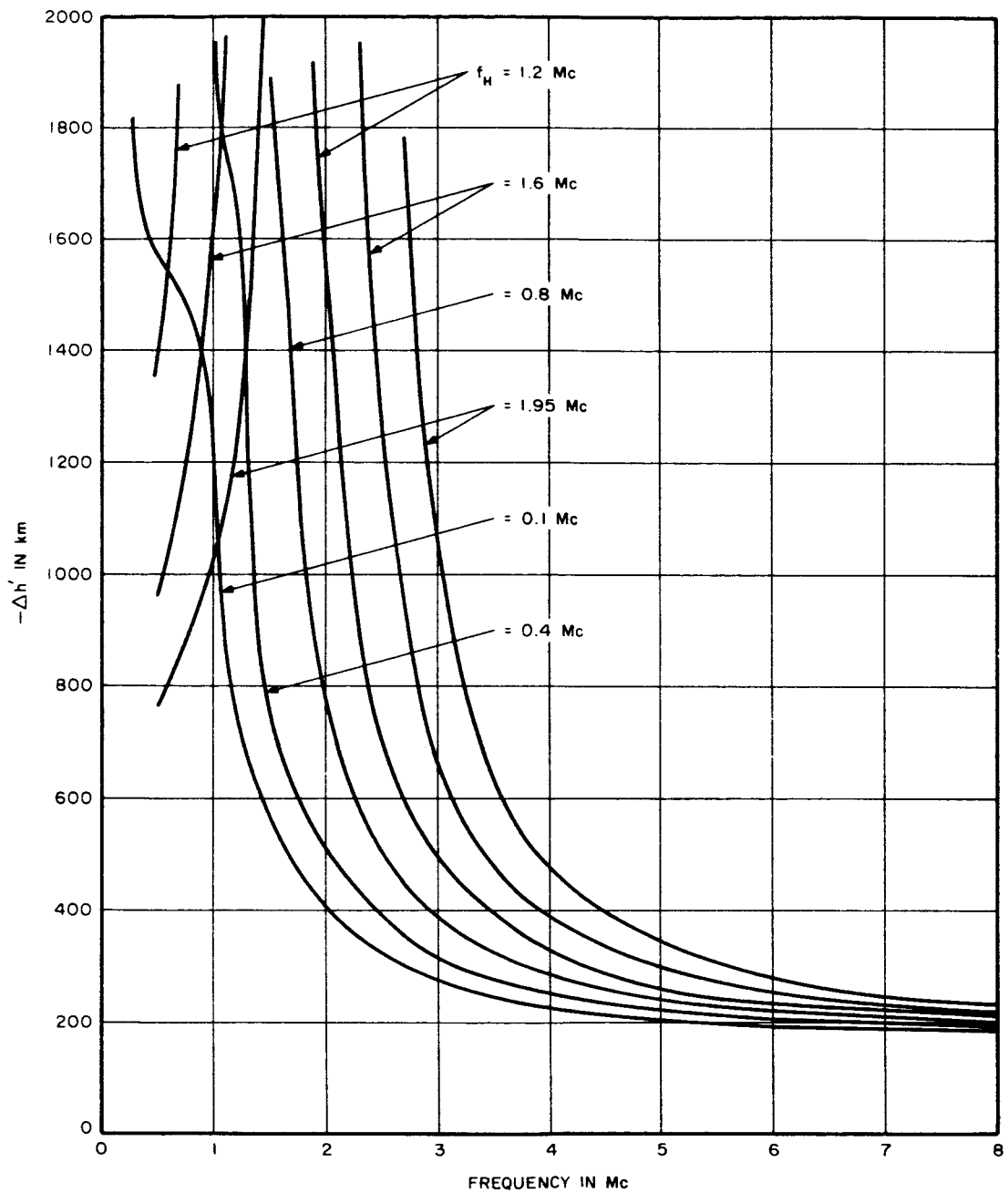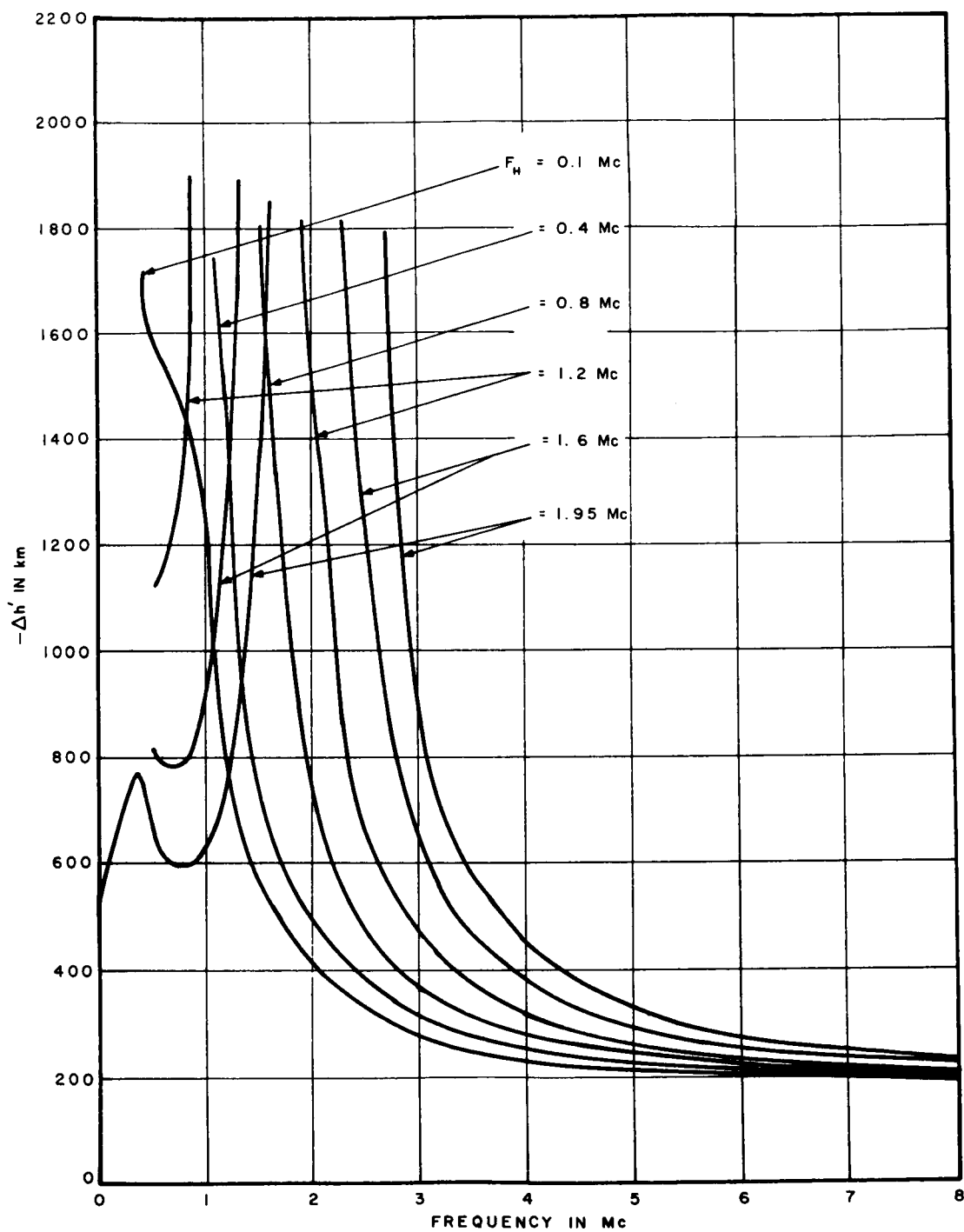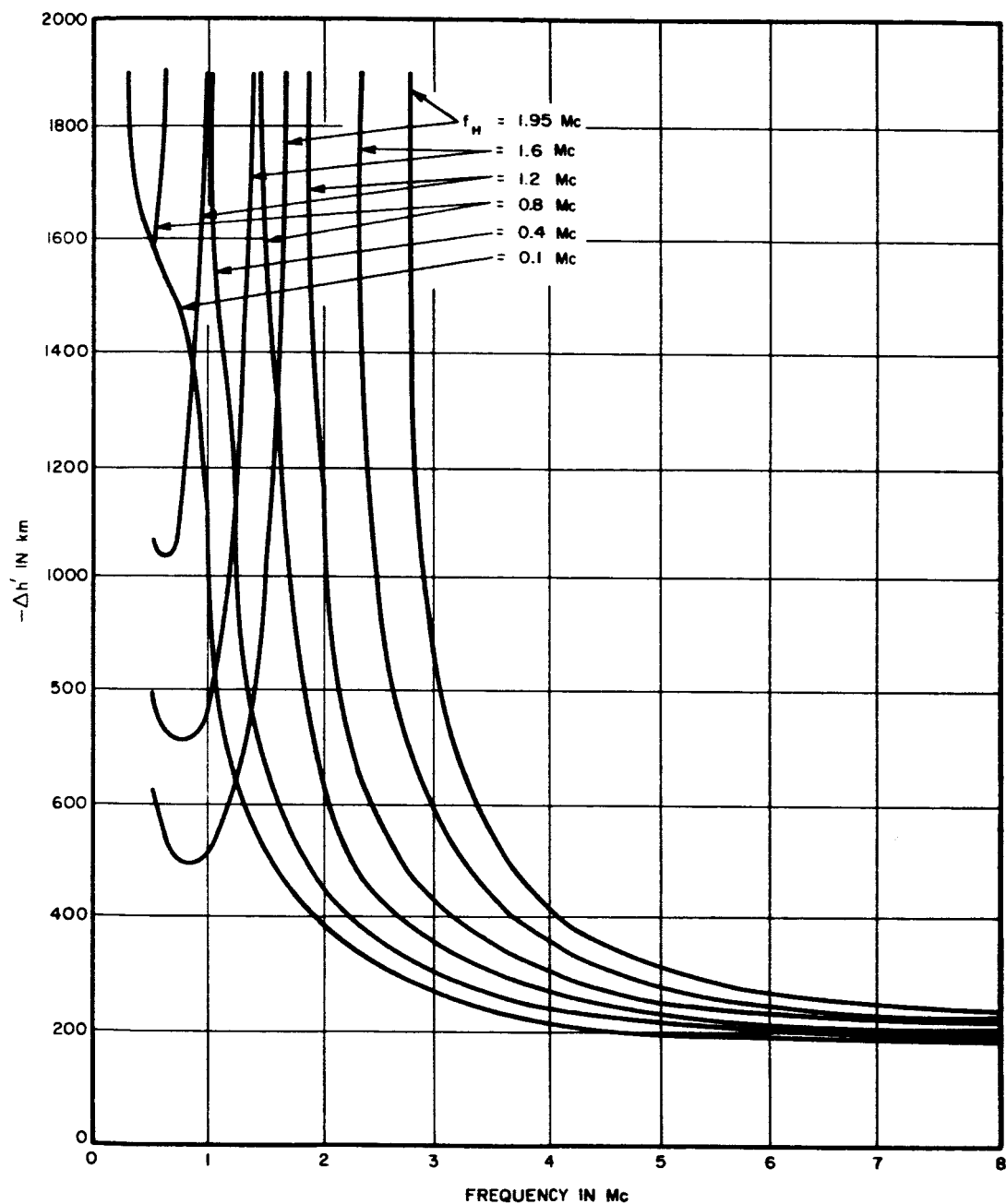DOUBLE-LAYER IONOSPHERE ($\Theta = 90$)

therefore, $\theta = 0$ degree, $Y > 1$ is excluded. Propagation angles of 55 and 90 degrees have minimums between 0.5 and 1.0 Mc created by the transition region between the two ionospheric layers. Figure 52 for $\theta = 55$ degrees, shows one completed curve including the zero frequency limit. The portion of the curve lying between 0 and 0.2 Mc is determined only by the upper layer (greater scale height) whereas, for large frequencies, $\Delta h'$ is influenced greatly by the lower layer. When the gyro-frequency is low enough, the transition effect is seen as an inflection of the $Y > 1$ portion of the curve, as shown in Figures 40 through 53.

The influence of the individual layers on the behavior of $\Delta h'$ is demonstrated by Figure 54, which is an expanded portion of Figure 52. Curves labeled $H_1$ and $H_2$ are the differential virtual depths obtained by evaluating $\Delta h'$ for scale heights of 120 and 960 respectively. The composite curve labeled $H_1 + H_2$ is for the double layered ionospheric model. The latter curve lies between the two former curves. It merges with $H_2$ at low frequencies and is asymptotic to $H_1$ at higher frequencies.

e. <u>$\Delta h'$ WITH PARABOLIC MAXIMUM DENSITY</u>

The addition of a peak density to the profile introduces an infinity in the differential virtual depths at the penetration frequency (Figures 55, 56, and 57). In actuality, reflections above the penetration frequency are to be expected due to surface returns from the planet. The previous $\Delta h'$ values must be modified only in the region in the vicinity of the peak density. Penetration frequencies are determined from $X = 1$ for an o-wave and $X = 1 \pm Y$ for an x-wave.
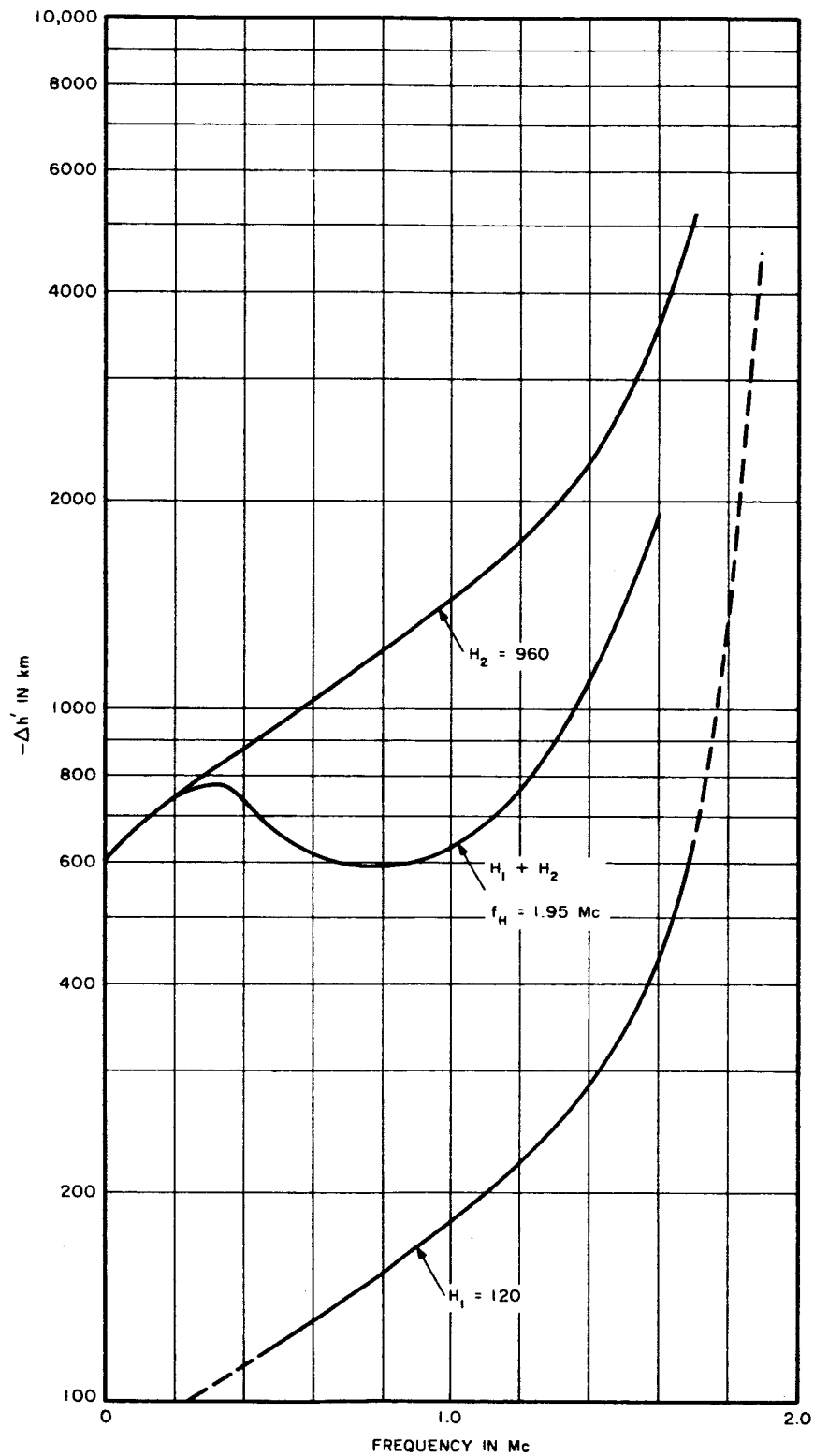
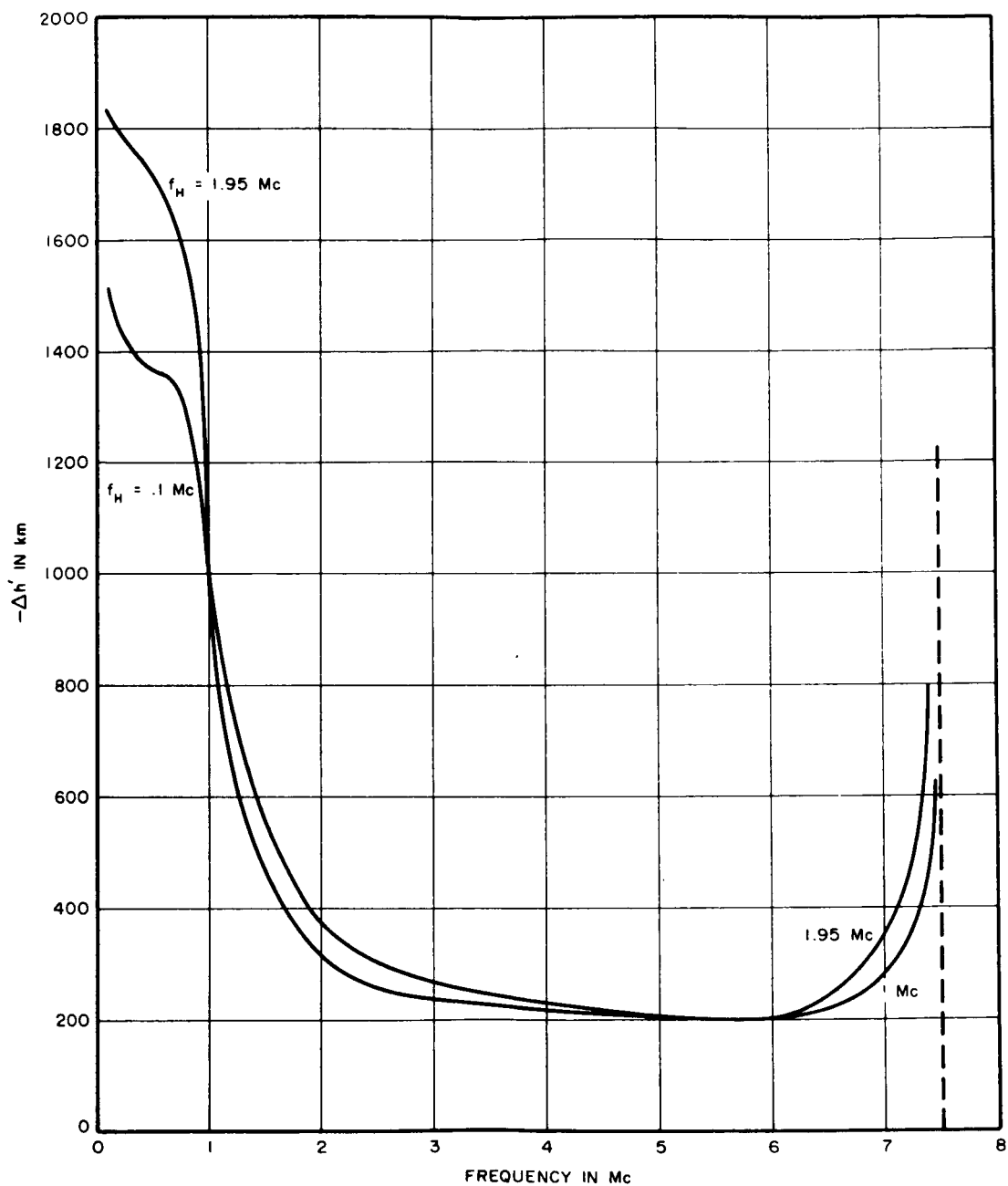FIGURE 54. EFFECT OF LAYERS ON BEHAVIOR OF Δh'

FIGURE 55. DIFFERENTIAL VIRTUAL DEPTH FOR o-WAVE IN
DOUBLE-LAYER IONOSPHERE WITH MAXIMUM
PARABOLIC DENSITY

124

FIGURE 56. DIFFERENTIAL VIRTUAL DEPTH FOR o-WAVE IN
DOUBLE-LAYER IONOSPHERE WITH MAXIMUM
PARABOLIC DENSITY

125
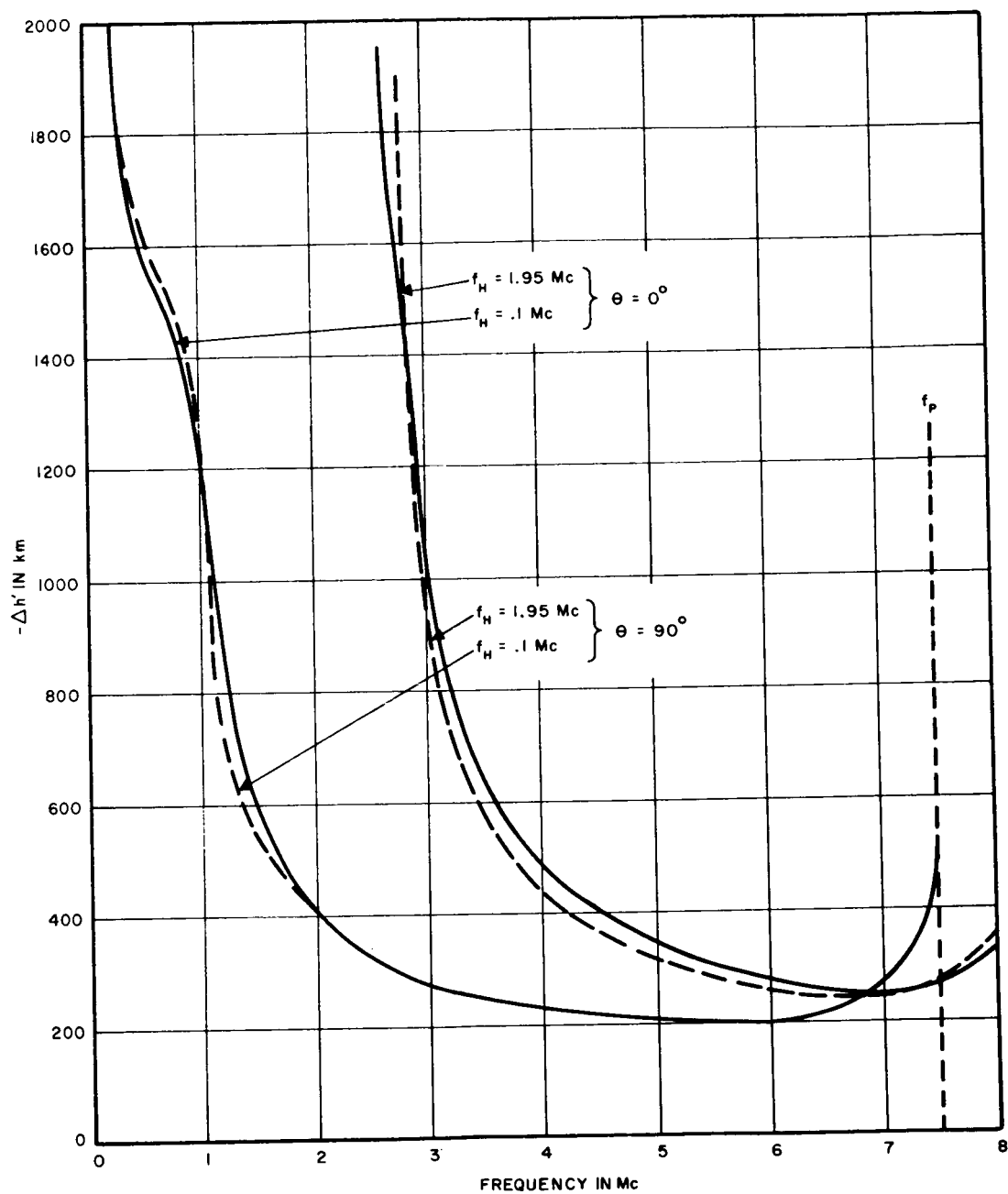
FIGURE 57. DIFFERENTIAL VIRTUAL DEPTH FOR x-WAVE IN DOUBLE-LAYER IONOSPHERE WITH MAXIMUM PARABOLIC DENSITY

## 4.    CALCULATION OF $\Delta h'$ FOR FINITE ALTITUDES

In a sounding from a flyby vehicle or orbiter, $\Delta h'$ has a zero value at the local cutoff frequency, which is finite and not zero, in contrast to the infinite altitude case.  It is appropriate then, at this juncture, to ascertain the applicable frequency range and the error introduced by using results based on an infinite altitude assumption.

Generically, the differential virtual depth for a sounding vehicle at a finite altitude is written as

$$\Delta h'_v = \int_{\phi_v}^{\phi_r} (\mu' - 1) \frac{dz}{df_N} F\ (f_H,\ f_N) f\ \cos \phi d\phi \tag{45}$$

Where $\phi_v$ = value of $\phi$ at the vehicle, $\phi_r$ = value at the reflection point, $F\ (f_H,\ f_N)$ = function which makes the integrand suitable for an o- or x-wave, $\mu'$ = corresponding group refractive index.  Let us define a correction term to the infinite altitude differential virtual depth as

$$\Delta h'_c = \Delta h' - \Delta h'_v = \int_{\phi_\infty}^{\phi_v} (\mu' - 1) \frac{dz}{df_N} F\ (f_H,\ f_N) f\ \cos \phi d\phi \tag{46}$$

where $\phi_\infty$ is the lower limit at $z = \infty$.  From equation 46, $\Delta h'_v$ may be determined by subtracting $\Delta h'_c$ from $\Delta h'$.

An altitude of 3,840 km (32 times the scale height of the lower layer) is chosen to demonstrate the correction to $\Delta h'$ necessary for a finite sounding altitude.  Figures 58 and 59 summarize some results obtained from equation 46.  At the cutoff frequency corresponding to this altitude, $\Delta h'_c$ is equal
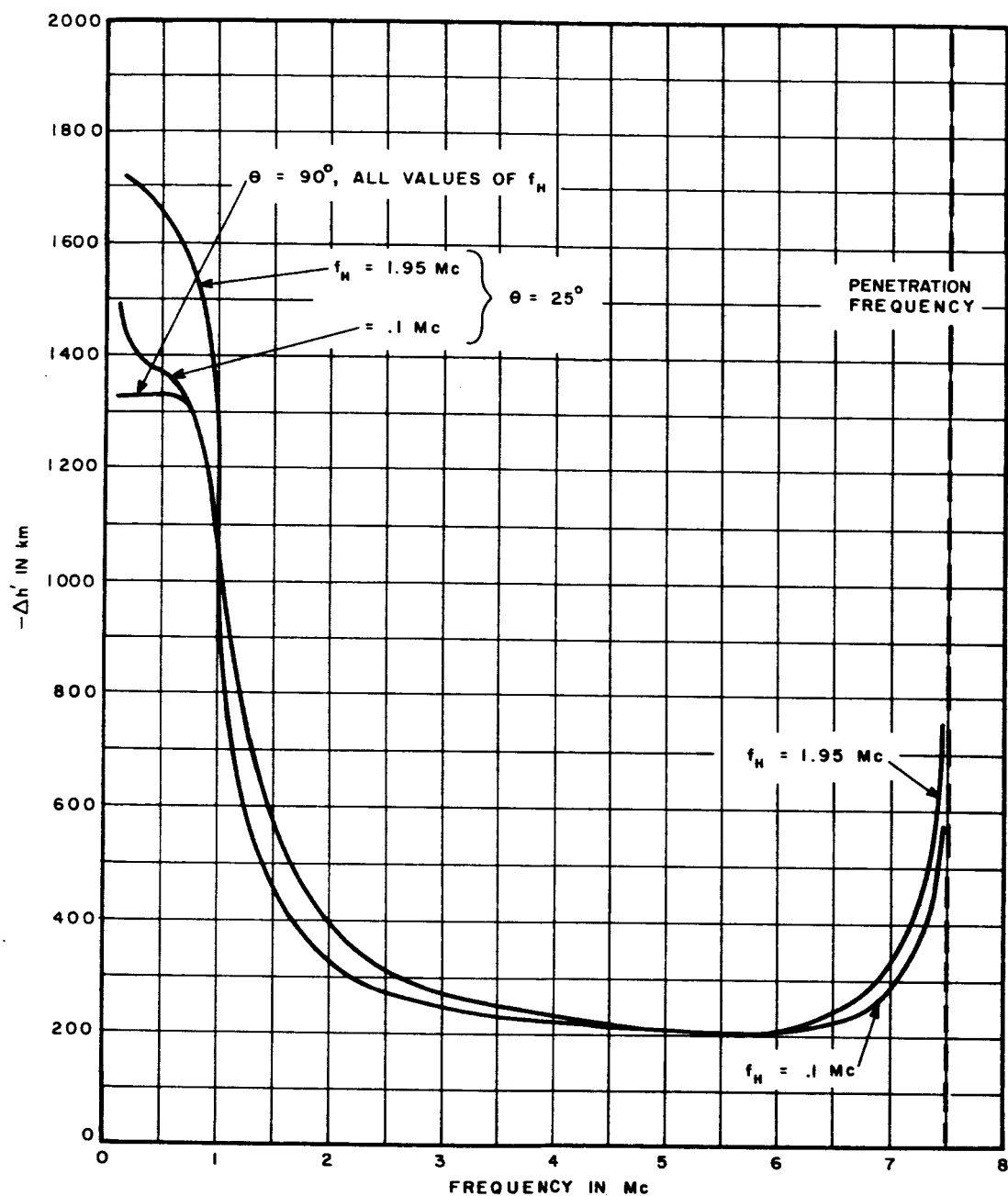
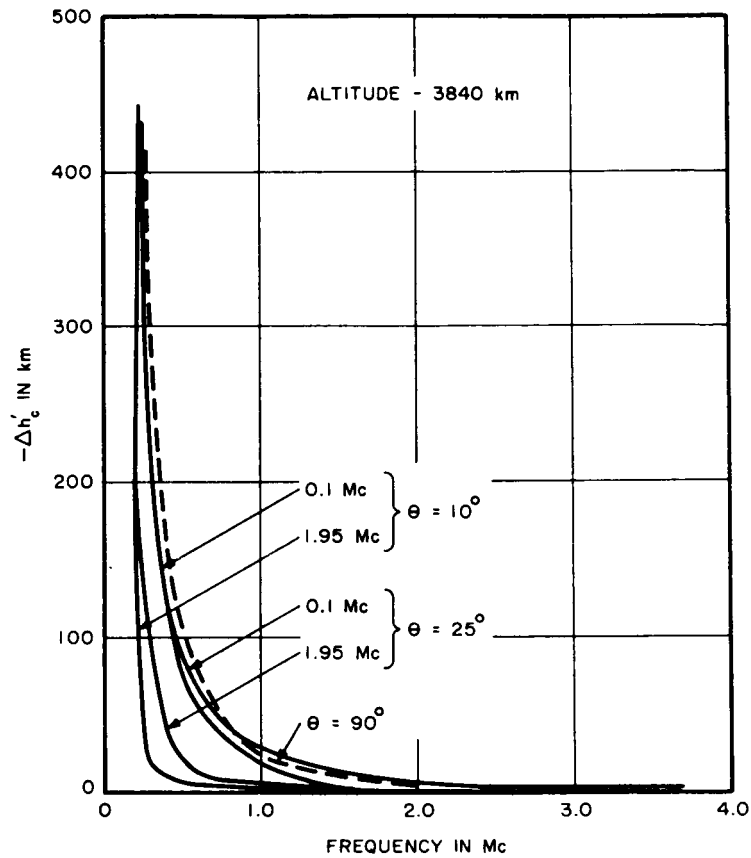FIGURE 58.  DIFFERENTIAL VIRTUAL DEPTH FOR o-WAVE IN
DOUBLE-LAYER IONOSPHERE AT FINITE SOUNDER
ALTITUDE

128
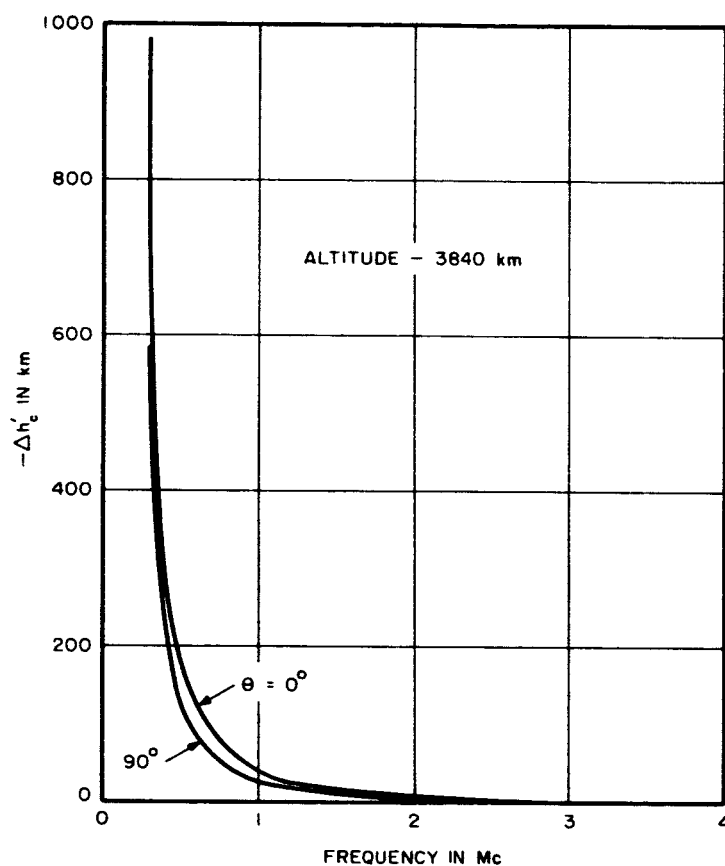
FIGURE 59. DIFFERENTIAL VIRTUAL DEPTH FOR x-WAVE IN DOUBLE-LAYER IONOSPHERE AT FINITE SOUNDER ALTITUDE

to $\Delta h'$ and $\Delta h'_v$ is identically zero.  From these curves we
can determine the frequency range over which the infinite
altitude calculations are valid approximations to solutions
for a finite altitude.  It can be seen from Figures 58 and 59
that the correction is negligible over most of the sounding
frequency range.

## D.  VIRTUAL HEIGHT PROFILES FOR INFINITE SOUNDER ALTITUDE

A sample of some of the resulting virtual height
profiles obtainable from the differential depths of Sec-
tion 4-C are given in Figures 60 through 66.  The manner in
which $\Delta h'$ is added to the actual electron density profile to
obtain the virtual height profile is shown in the first fig-
ure.  Figures 60 and 61 show the dependence upon gyro-fre-
quency and propagation angle for a simple single layer iono-
sphere.  At high frequencies, all virtual profiles are asymp-
totic to $\theta = 90$ degrees which is displaced at all frequencies
by a constant value proportional to the scale height.  In the
case of an o-wave, the frequency scale represents both the
plasma and sounding frequencies.

Figure 62 has results for a double-layer ionosphere
possessing a peak density.  These virtual heights show dips
that are typical of much data observed by the Alouette sat-
ellite.  The dip occurs mainly from the change in the scale
height in the transition region between the layers.  The
extent of the dips of these virtual height curves are related,
in a complicated fashion, to the magnetic field strength.  For
the example shown, the 1.95-Mc gyro-frequency curve is 250 km
deeper than the 0.1-Mc curve.

The x-wave virtual profile is obtained from the elec-
tron density true height curve and $\Delta h'$ in a more complex fashion
than the o-wave.  A so-called reflection profile is required.

FIGURE 60.   VIRTUAL HEIGHT PROFILES FOR o-WAVE IN
             SINGLE-LAYER IONOSPHERE (θ = 10)

FIGURE 61.  VIRTUAL HEIGHT PROFILES FOR o-WAVE IN
SINGLE-LAYER IONOSPHERE ($f_H$ = 1.95 Mc)

132
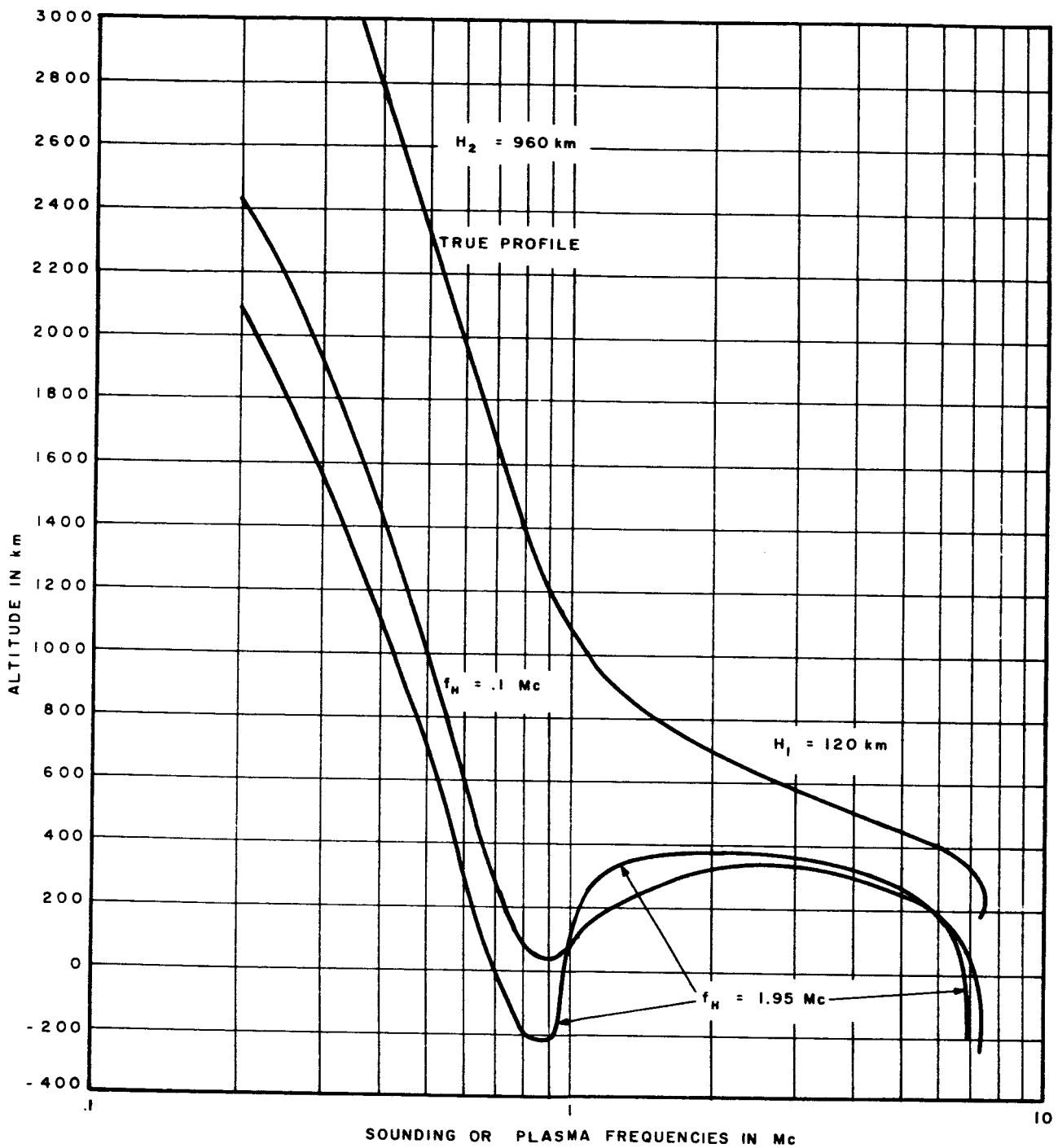
FIGURE 62.  VIRTUAL HEIGHT PROFILES FOR o-WAVE IN
DOUBLE-LAYER IONOSPHERE ($\theta$ = 10)
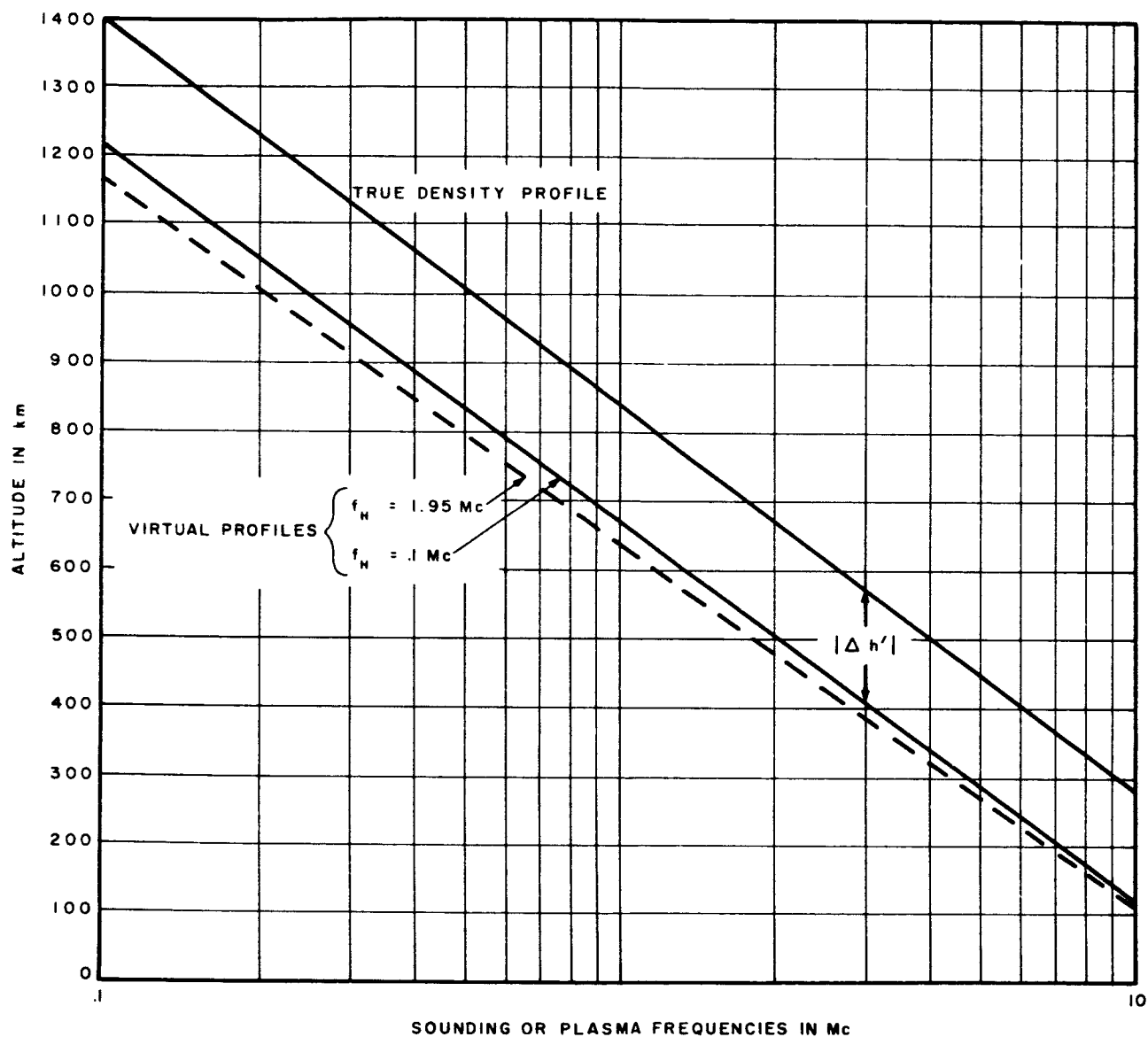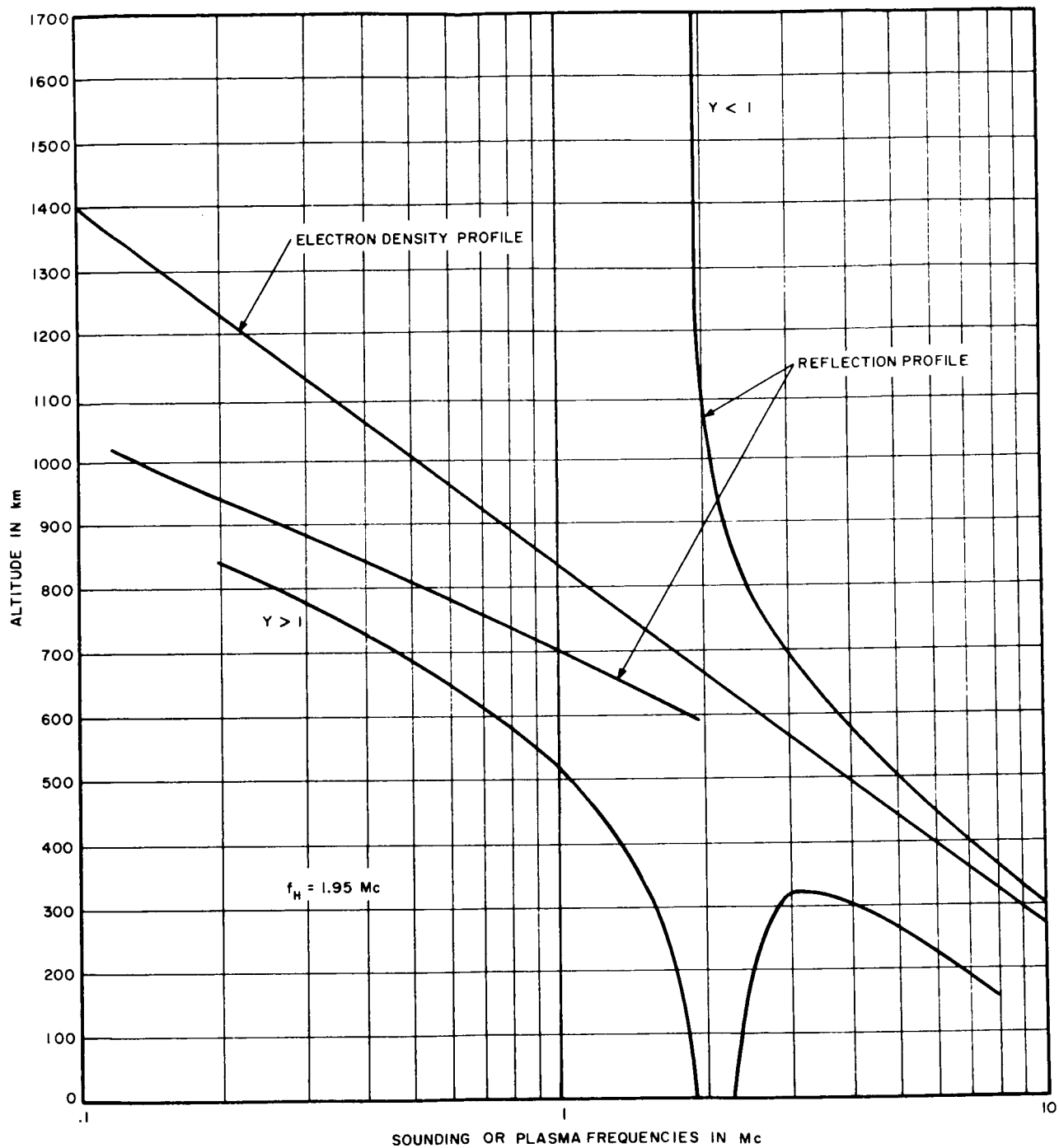
FIGURE 63. VIRTUAL HEIGHT PROFILES FOR x-WAVE IN
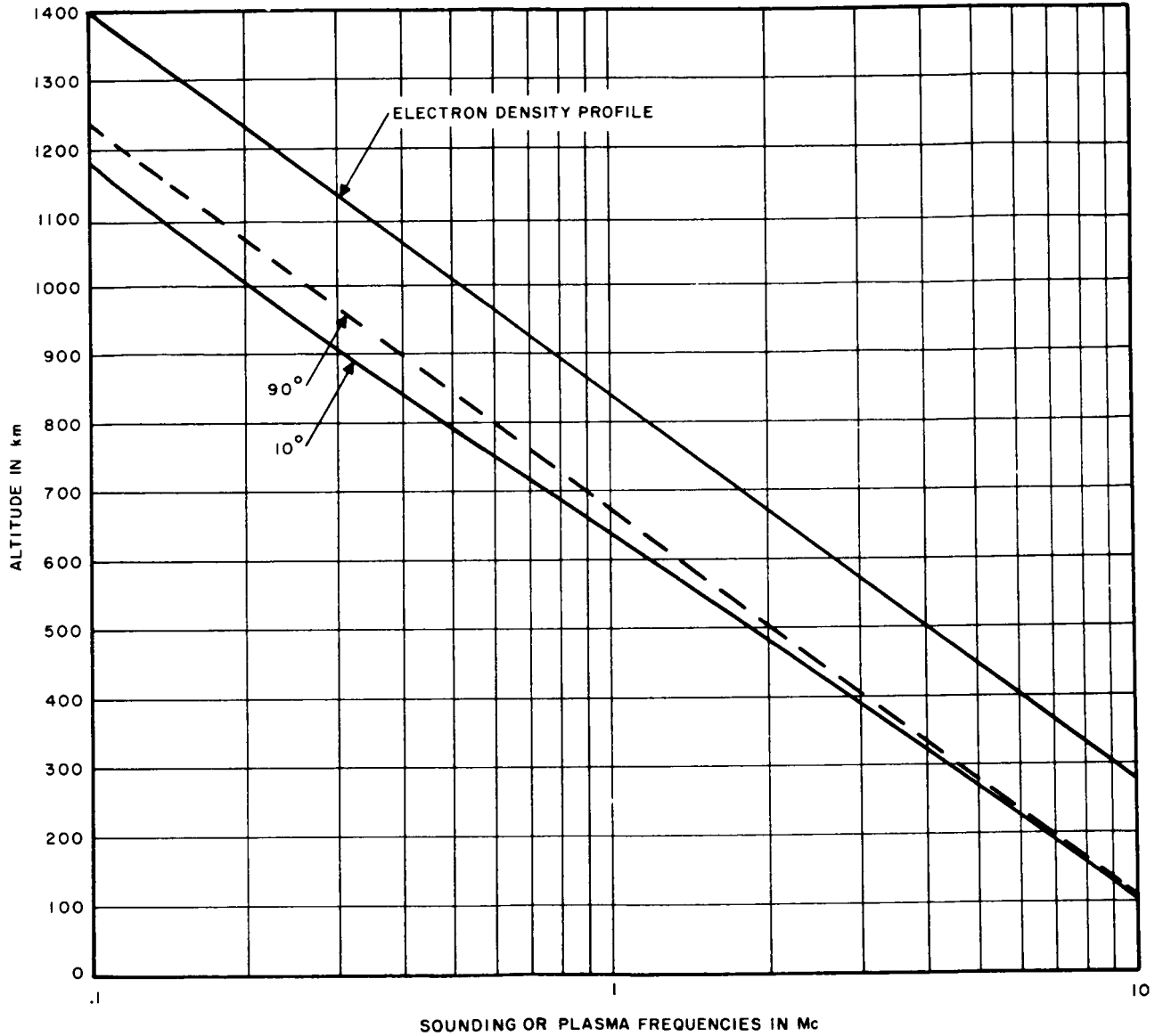DOUBLE-LAYER IONOSPHERE ($\theta$ = 90)
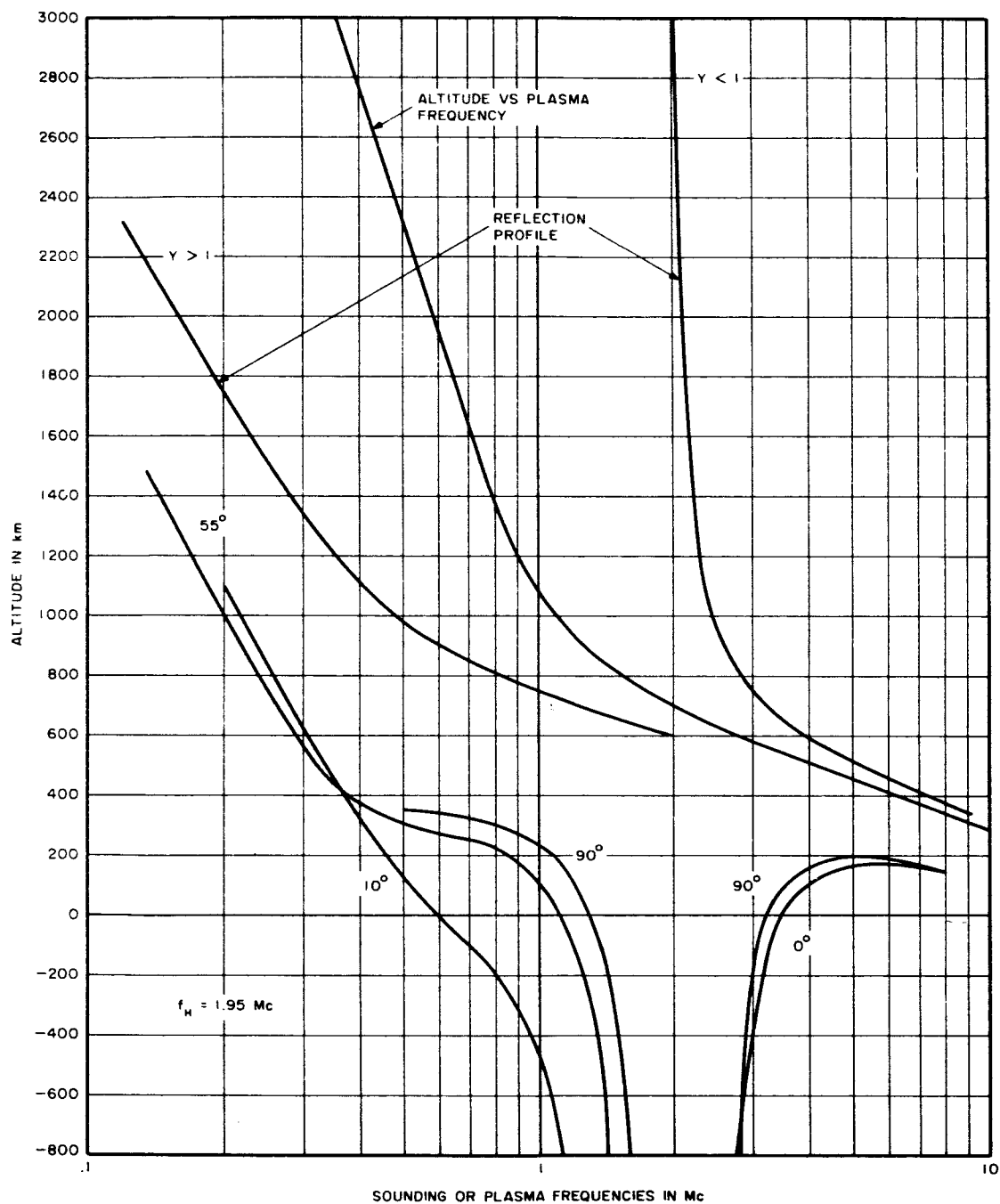
FIGURE 64. VIRTUAL HEIGHT PROFILES FOR x-WAVE IN DOUBLE-LAYER IONOSPHERE ($f_H = 1.95$ Mc)

135
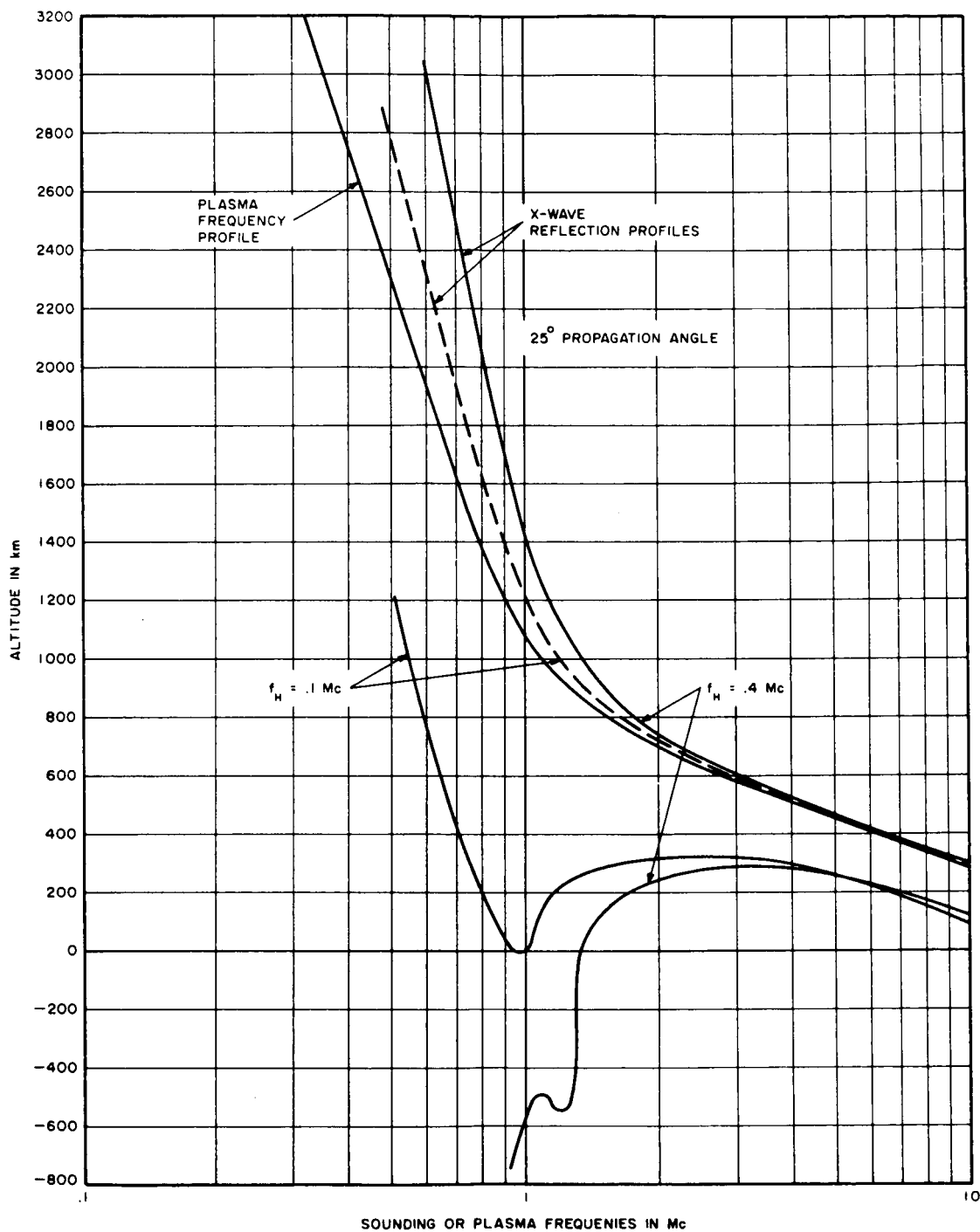
FIGURE 65.  VIRTUAL HEIGHT PROFILES FOR x-WAVE IN
DOUBLE-LAYER IONOSPHERE ($f_H = 0.1$ Mc)

136
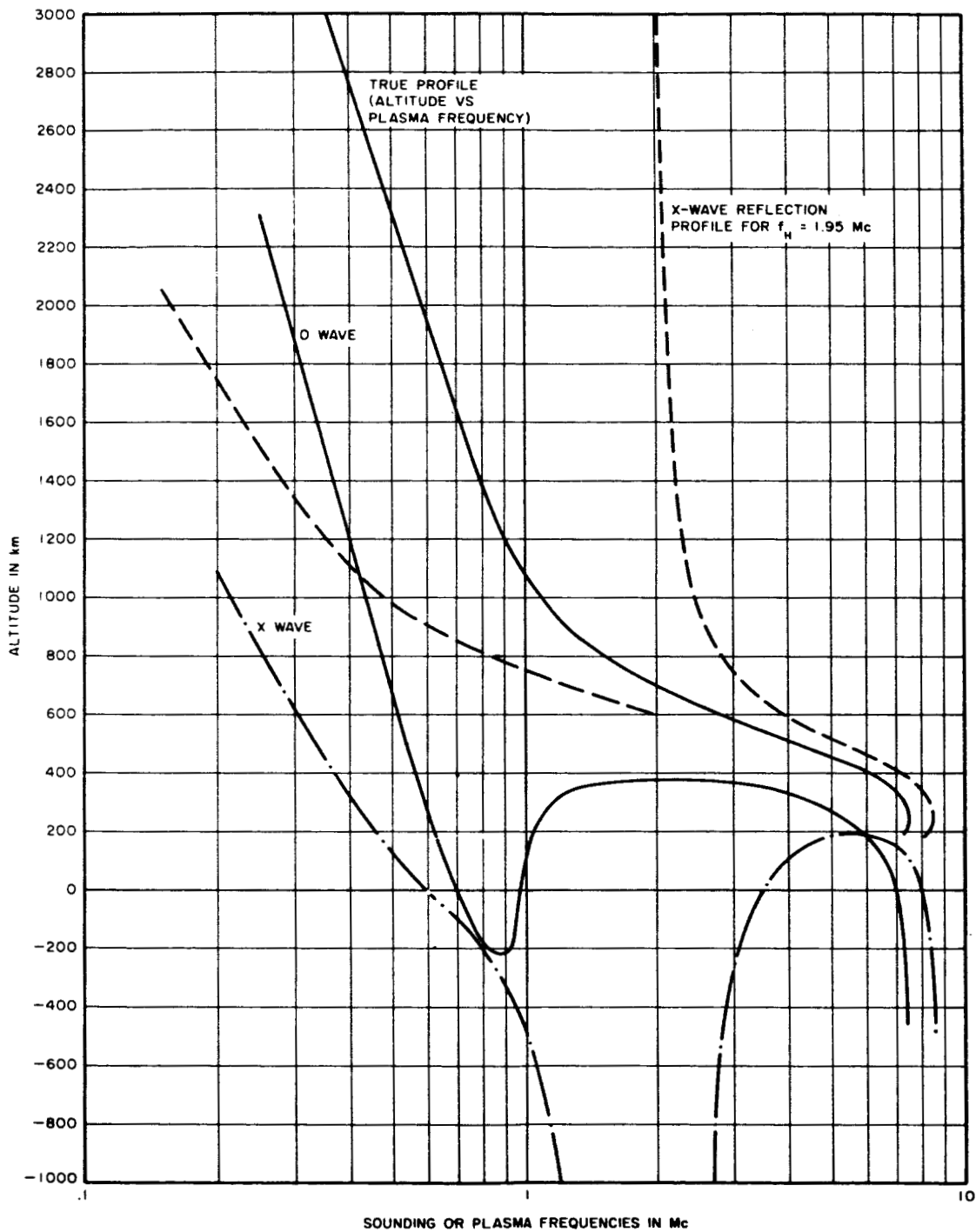
FIGURE 66.   VIRTUAL HEIGHT PROFILES FOR o- AND x-WAVES
IN DOUBLE-LAYER IONOSPHERE

137

This profile is constructed by plotting the x-mode reflection frequency corresponding to the plasma frequency and gyro-frequency at each altitude. Reflection and true height profiles are shown in Figures 63 and 64 along with x-wave virtual height curves. Abscissa, representing frequency in these figures, are interpreted as either plasma frequency for the true electron density profile, or as sounding frequency for the reflection profile. Figure 63 is an example of results obtained for a single layer. The gyro-resonance at $Y = 1$ is relatively narrow compared to the resonance for the double layer of Figure 64. Gyro-resonance broadening for the double layer occurs as a result of increased delay time which is due to the larger electron densities and density gradients.

If the gyro-frequency were sufficiently lower than the sounding frequencies for the transition region, then the x-wave virtual height dip will occur as for the o-wave (Figure 65, $f_H = 0.1$ Mc). When the gyro-resonance occurs in the vicinity of the transition region, the resonance predominates and the dip is reduced. It is also possible to have an inflection as shown in Figure 65 for $f_H = 0.4$ Mc.

Figure 66 compares virtual heights for both an o-wave and a x-wave in a double-layer profile with a peak density region for $f_H = 1.95$ Mc. One important feature in this comparison is, of course, the difference between the respective penetration frequencies of the waves 28. Note also the dip in the o-wave and the resonance of the x-wave.

For finite sounding heights, virtual depth profiles will start at zero depth for the local sounding frequencies and then rapidly increase demonstrating many of the features

of the curves referred to in this section. Dips are char-
acteristic of transition regions between layers. Straight
slope sections are characteristic of constant scale height
regions when the slope on a semi-log plot is relatable to the
scale height of the true electron density profile. Many of
these features are well exampled by data from the Alouette
satellite.

E.   INTERPRETATION OF DATA

The measurement of the ionosphere of a planet other
than Earth is somewhat different from topside sounding the
Earth's ionosphere. In the latter case, prior to the first
topside sounding, there was a considerable amount of informa-
tion which greatly simplified the problem of reducing data.
The magnetic field was known, the lower part of the ionosphere
and atmosphere below the peak density was known, and some
information for the region above the peak was available from
rocket flights. Furthermore, a satellite could be placed in
an orbit which could be precisely known with respect to the
Earth, and all measurements made with respect to the satellite
could be readily interpreted relative to the Earth.

On the other hand, little is known about other plan-
ets. In general, the magnetic field is not known, there is
little information about the atmosphere, and there certainly
is no bottomside data. The orbit relative to the planet is
uncertain and depends on the mission, and even in this case
there is always the possibility of large errors considering
the difficulties in guiding a spacecraft to a planet. These
differences, as well as others of a purely engineering nature
(such as data transmission rates and storage), result in some-
what modified considerations relative to data interpretation
and reduction.

The purpose of this section is to outline and discuss some of these aspects and their relationship to the theoretical studies previously described.

## 1. DETERMINATION OF ELECTRON DENSITY AND MAGNETIC FIELD PROFILES

Transmission time delay measurements result in data consisting of virtual depth versus frequency. If the magnetic field is known at each point along the propagation path and if the sounder position relative to the planet is known, then the true height of the electron density profile can be derived from these measurements. The profile is unambiguous provided that the electron density varies monotonically, as is expected above the maximum density level.

For a planetary sounder then, either independent measurements must be made of the magnetic field and height of the spacecraft above the planetary surface, or the sounding experiment must be fully comprehensive and permit the evaluation of these important data. Some information may be gained from other sources, since it is highly likely that magnetometers will be on board providing local magnetic field measurements, and since Earth-based radio measurements will provide orbit data. The local magnetic field measurements would require extrapolation by assuming a model, such as a dipole field, to obtain the field along the propagation path. However, if the spacecraft were far enough from the planet to be either outside a magnetosphere or just inside, there may be considerable difficulty in extrapolating to the much lower altitudes where ionization is significant. Also the orbital information may not be sufficiently accurate with respect to the planet's surface.

In any event, the best experiment would be one which was completely self-contained, and other independent sources of information could supplement the experiment. Then, in the

event of the failure of these outside sources, or for such
other difficulty as could arise, the self-contained, com-
prehensive sounder experiment would still provide data to
determine the true height profile.

As previously noted, the experiment could detect
the surface by sounding at a high enough frequency to pene-
trate the ionosphere. This measurement, in conjunction with
the virtual depth data, could provide the location of the
ionosphere with respect to the planet. The measurement of
virtual depth to and beyond penetration could also provide
magnetic field information at the level of the peak density,
since the difference in penetration frequencies of the o- and
x-modes is related to the gyro-frequency[28]. This informa-
tion together with magnetometer measurements of the local
field, or gyro-frequency resonances in the sounder data,
could be used with a dipole field model to provide the field
along the propagation path.

It should be noted that specification of the mag-
netic field strengths from the measurements is not sufficient
to establish the field model. The dip angle must be known
as well. Magnetometer measurements may provide the local dip
angle. If this is not complicated by a magneto-pause, the
effective dipole orientation can then be found. The penetra-
tion frequencies do not provide this data and local gyro reso-
nances probably cannot be used with any reasonable accuracy
to provide this angular data. The presence of z-mode type
propagation also can yield bounds on the dip angle, partic-
if the z-mode frequency for the peak level can be identified
as well as in the o- and x-modes. Nevertheless, without such
dip angle sources, the desired data is contained within the
virtual depth measurements, but must be extracted by methods
that have not been necessary to apply to Earth sounding data.

Fortunately, the dip angle is not necessary to provide electron density information when $Y < 1$, since the x-mode virtual depth information is not very sensitive to this angle, as shown by Figure 41. Given the magnitude of the field strength, standard procedures can be used to reduce data.

Some sense of the magnetic field strength may also be drived from the extent of the dip of the virtual depth in a multilayer ionosphere (as shown in Figures 62 and 65). However, the relationships are complex and involve several variables, in particular, transition gradients. They have not been fully treated as yet and further study is required. The gyro frequency infinities shown in Figures 63, 64, and 65 are typical of a constant field independent of altitude. For a field that varies with altitude, the virtual height has an infinity at the gyro-frequency but varies in a somewaht different manner, as discussed further in Section 4-E.

Using a dipole field mode, the electron density profile may be obtained by a lamination method[29]. Since x-trace data is usually more complete than o-trace data, the electron density profile may be found from x-wave reflections. When $Y < 1$, dip angle errors do not significantly effect profiles derivable from the x-trace data. If limited, on-board magnetometer measurements do not yield dip angle then the x-trace data reduction is that much more desirable.

Magnetic field profile corrections may be made by computing the o-wave virtual profile from the postulated magnetic field and x-wave derived electron density profile. Comparison of the measured and computed o-wave virtual profiles gives then a notion of profile accuracy.

When agreement is not within experimental errors, alterations of the magnetic field model may be made, new electron densities obtained, and hence a new computed o-wave virtual depth profile found. This cycle is repeated until sufficient self-consistency is achieved between profiles and data.

If insufficient data, either from magnetometer or penetration measurements, are available to establish an initial magnetic field model, the electron density and magnetic field may be roughly determined using the differential virtual depth single-layer characteristics as shown in Figures 37 and 41. The magnetic field may then be used in a lamination analysis for further refinement as previously described. Assuming an exponential electron density profile and that time delay occurs mainly in the vicinity of a reflection point, the virtual depth may be written as

$$h'(f) = Z_s - Z_r + Hg(Y, \Theta) \tag{47}$$

where $Z_s$ = spacecraft altitude, $Z_r$ = reflection altitude, $g(Y, \Theta)$ = functional relationship between magnetic field parameters $Y$, $\Theta$ and the ratio of the differential virtual depth $\Delta h'$ and the electron scale height $H$ (such as Figures 37 and 41). The value of $Y$ is a mean value weighted according to time delay, and if significant time delay occurs near the reflection point the value of $Y$ is close to that of the reflection point. Using the sounder altitude as the reference point, it is easily seen that

$$X = \frac{bN_s}{\omega^2} \epsilon^{-\frac{Z - Z_s}{H}}, \tag{48}$$

where $N_s$ is the local electron density and b is the constant $\epsilon^2/(\epsilon_o m)$. The x-wave reflects at X = 1 - Y. Therefore,

$$Z_r - Z_s = - H \ln \frac{\omega^2}{bN_s} (1 - Y).$$   (49)

Substituting equation 49 into 47, replacing Y by its defini-tion, we obtain

$$h'(\omega) = H \left[ g(\omega_H, \omega, \Theta,) + \ln \frac{\omega^2}{bN_s} (1 - \frac{\omega_H}{\omega}) \right].$$   (50)

which is the x-mode virtual depth, and contains H, $\omega_H$, and $N_s$ as unknowns. When Y < 1, g(Y, $\Theta$) is nearly independent of dip angle $\Theta$ and is a function which analytically approximates Figure 21. Choosing three frequencies close together at which vertical depth data have been obtained, we may solve for a scale height, gyro-frequency, and the electron density at the sounder. If the local density is estimated or measured, only two frequencies are required. An approximation, therefore, of the scale height and magnetic field of a particular region is obtained, the region corresponding to the reflection level of the three frequencies. Applying the above analysis to a number of frequencies gives a rough approximation to the elec-tron density and magnetic field profiles with an accuracy that is probably reasonable as a first cut at a planetary ionosphere. Furthermore, the magnetic field may then be used for a finer treatment in a lamination analysis as described. In particular, the procedure would be to apply equation 50 to the lowest set of frequencies which define a first layer nearest the sounder, and, then, to subsequent layers for higher groups of frequen-cies. In carrying this procedure to lower level layers the delay contributed by the higher levels may be accounted for in equation 50 to provide a more refined model.

Having obtained scale height, magnetic field strength, and local density in this fashion for x-wave virtual depths when Y < 1, we can apply equation 50 to o-wave data and estimate the dip angle which should be constant for a dipole model. The appropriate function $g(Y, \theta)$ must be used for the o-mode.

For a planet with a large field, such as Jupiter, the assumption Y < 1 may not be valid. In this case $g(Y, \theta)$ varies considerably with $\theta$ even for the x-mode, as shown in Figure 41, and a fourth frequency may have to be used to find $\theta$. The check on the $\theta$ value is its consistency for a vertical path in a dipole field. Complications such as propagation along the field lines may be apparent in attempting this type of analysis. Therefore, it should be noted that ducting and scattering cannot be treated this way. However, the experience with Explorer XX and Alouette ionograms may aid in the interpretation of such complications.

There are other applications of the results of the differential virtual depth analysis that may be applied, such as the high- and low-frequency asymptotic limits and their relationships to scale height. The possibility of their application depends on the frequency range and the nature of the ionograms. All of these aspects, including the above method of reduction, require further study and elaboration. In particular, the application to Alouette data would be most fruitful, as well as an extension of the analysis to a dipole field.

For a planet with no significant magnetic field, the analysis is greatly simplified. The relationships between the true and virtual height profiles may be treated directly without the complications described. Furthermore, approximations by exponential sections relate scale heights directly with the results, as may be seen from Figures 47 and 41 for Y = o.

## 2.    PROPAGATION CHARACTERISTICS OF THE x-WAVE

The x-wave traces which appear in Figures 63, 64, 65, ($f_H$ = 0.4 Mc ), and 66 are not entirely observable since the magnetic field strength is variable and not a constant value as was assumed in the computation.  This section discusses the effects of a magnetic field and electron density, which varies with height in a qualitative fashion.  It is shown that only half of the gyro-resonance effect of Figures 63 through 66 occur.  Also, that stop or forbidden frequency bands exist.  The analysis is restricted to x-wave propagation characteristics, but a corresponding discussion may be developed for z-mode propagation as well.  The high-frequency limit of the z-mode propagation band involves the dip angle, and the procedure described would be modified by inclusion of this additional variable.

Consider the three possible density and magnetic field configurations in Figure 67 which present plasma or gyro-frequency versus depth.  The zero point corresponds to the spacecraft.  In each configuration, the electron density is taken as exponential and the magnetic field is assumed linear.  These configurations do not cover all possibilities but they do illustrate basic features which are independent of profile details.  The three cases shown in Figure 67 are:

Case 1--The local plasma frequency at the sounder is less than the local gyro-frequency. The plasma frequency increases with depth from the sounder until it equals the gyro-frequency, beyond which it is the higher of the two.
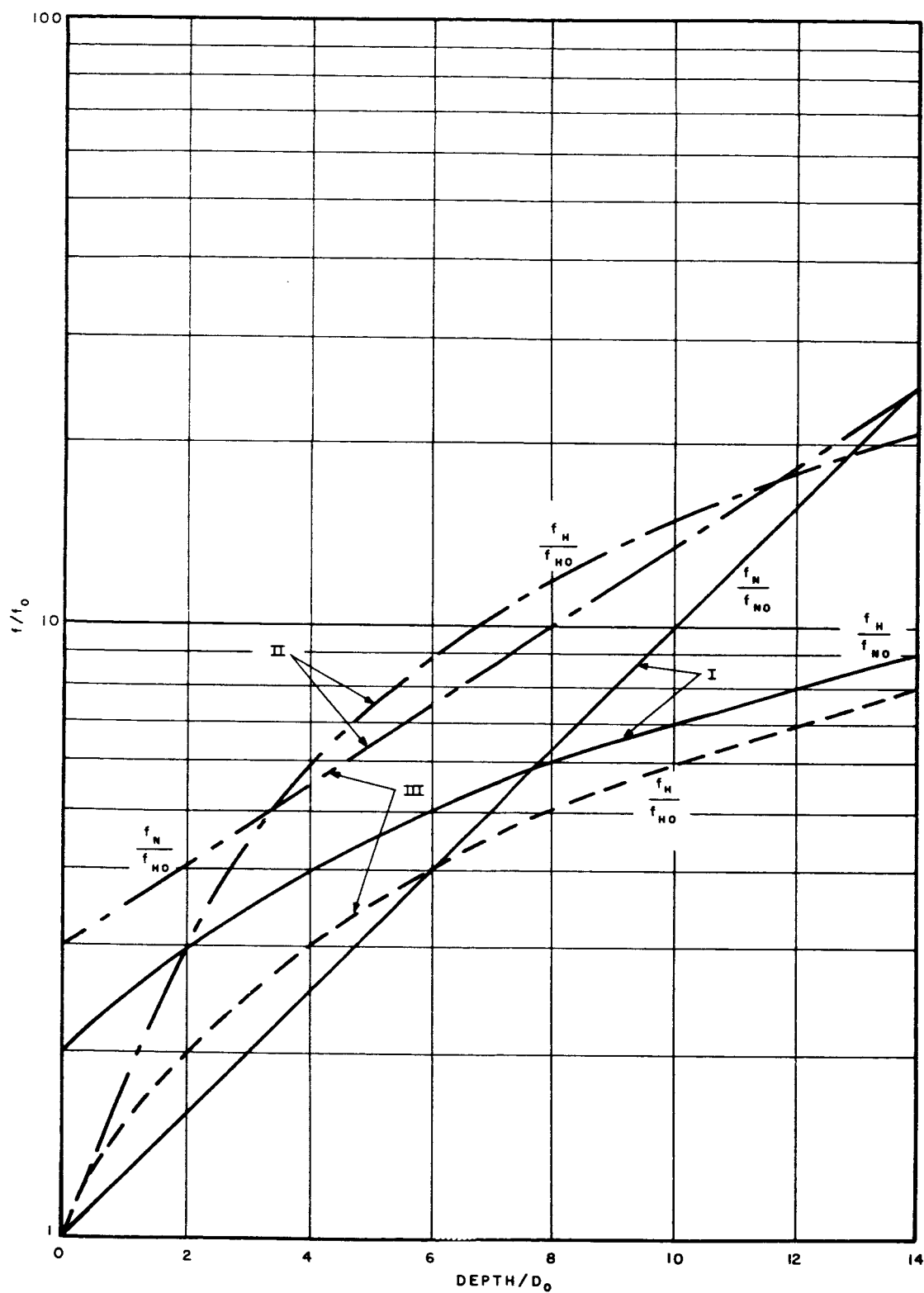
FIGURE 67.   THREE POSSIBLE ELECTRON DENSITY AND
MAGNETIC FIELD CONFIGURATIONS

Case 2--Local plasma frequency is higher than
the local gyro-frequency. Plasma fre-
quency decreases below the gyro-fre-
quency with depth, but decreasing less
rapidly than the gyro-frequency once
again becomes the greater of the two.

Case 3--Gyro-frequency is everywhere lower than
the plasma frequency.

Frequency $f_{HO}$ and $f_{NO}$ are the local gyro and plasma
frequencies at the vehicle; $D_O$ is an arbitrary normalization
number for the depth.

Figures 68, 69, and 70 are generated by normalizing
all frequencies to the plasma frequency at each altitude.
$F^+ = f^+/f_N$ and $F^- = f^-/f_N$ are normalized x-wave reflection
frequencies $f^+$ and $f^-$, corresponding to $Y < 1$ and $Y > 1$,
respectively. $F_H = f_H/f_N$ is the normalized gyro-frequency
and $F_1$, $F_2$, and $F_3$ are selected normalized sounding frequencies.
In the discussion, F is any normalized frequency.

The three cases behave similarly for frequencies so
that $F(0) > F^+(0)$ at the vehicle ($F_1$ is a frequency which
satisfies these criterion). Under the circumstances, down-
ward vertical propagation of the x-wave in a $Y < 1$ domain is
possible, for all cases, down to a depth defined by $F = F^+$.
At this level, $X = 1 - Y$ and reflection occurs. In our exam-
ple, $F_1 = F^+$ at the reflection level. Local gyro resonance
is also possible in all cases.

Starting at zero frequency and increasing the fre-
quency up to $F^+(0)$, the following x-wave propagation char-
acteristics are obtained:

Case 1--Propagation at normalized frequencies
below $F^-(0)$ is not possible since $X > 1 + Y$.
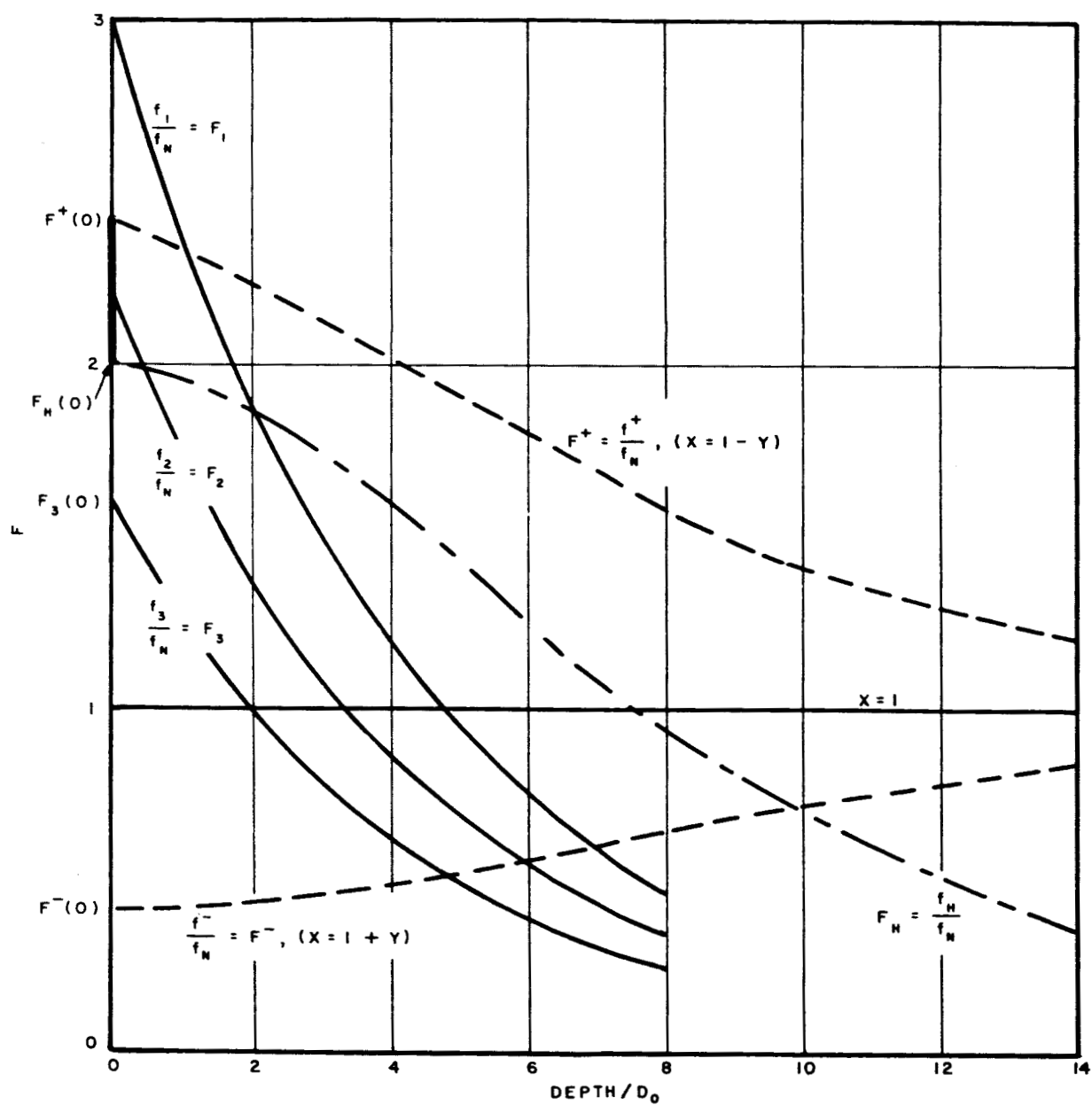Frequencies ($F_3$ in Figure 68) for which

FIGURE 68.  PROPAGATION CHARACTERISTICS OF x-WAVE
(CASE 1)

149
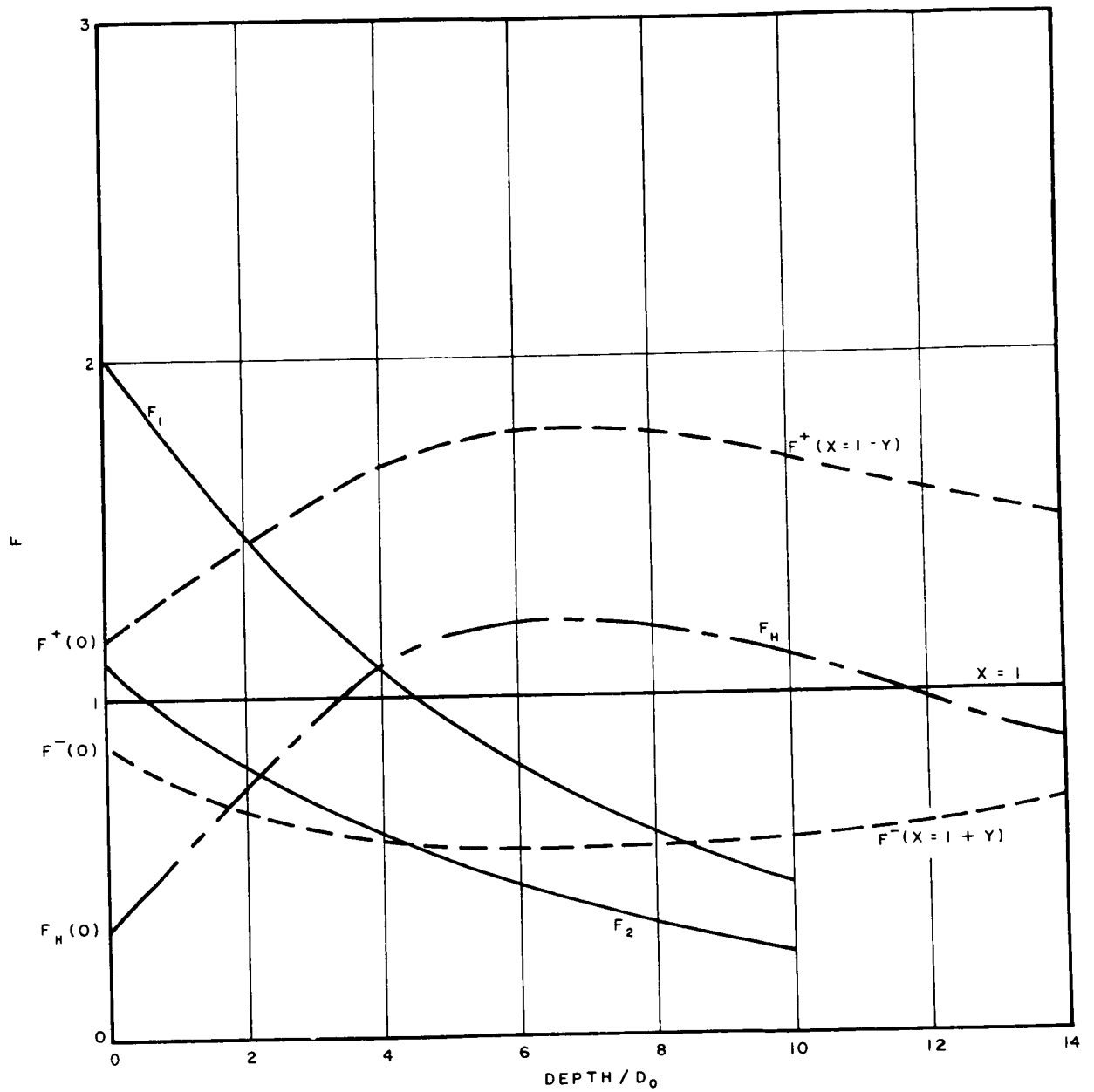
FIGURE 69. PROPAGATION CHARACTERISTICS OF x-WAVE
(CASE 2)
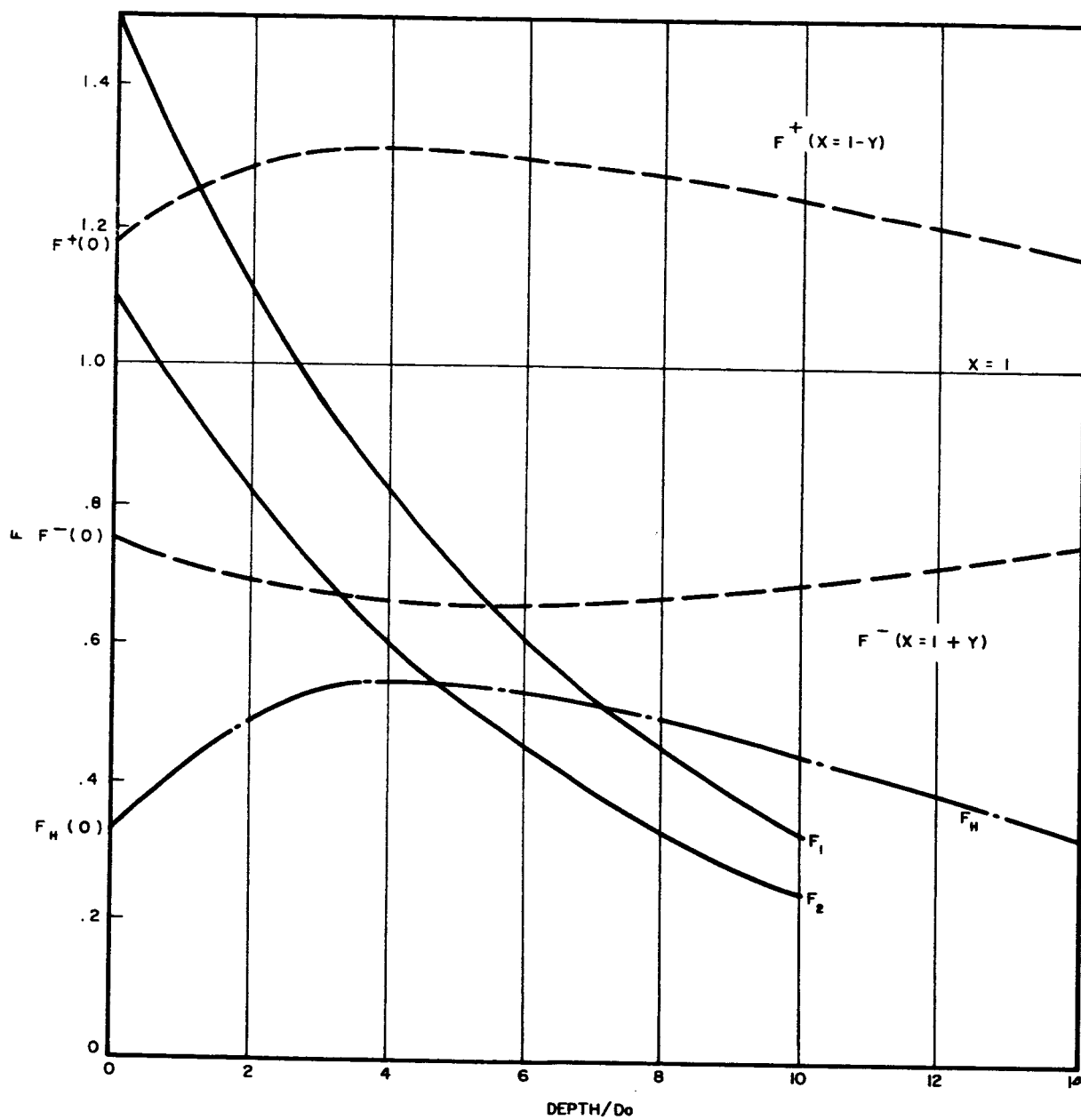
FIGURE 70. PROPAGATION CHARACTERISTICS OF x-WAVE (CASE 3)

$F^-(0) < F(0) < F_H(0)$, will propagate
down to the $X = 1 + Y$ depth. Within
the frequency range bounded by $F_H(0)$
and $F^+(0)$, however, Y is less than
unity, but $X > 1 - Y$. Therefore, in
this frequency range, the medium sur-
rounding the antenna is cut off and
downward x-wave (not the z-mode)
propagation is not possible. $F_2$ is
an example of a cutoff frequency.
Figure 71 summarizes these results
for Case 1. Virtual depth is quali-
tatively indicated by the plots.
Propagation is represented by the
clear areas, whereas propagation does
not occur for the frequencies within
the cross-hatched regions.

Case 2--The band from zero to $F^-(0)$ is cut off
since $X > 1 + Y$. Gyro resonance may
occur at $F(0) = F_H(0)$. For the con-
figuration shown in Figure 69, $F_H(0)$
is less than $F^-(0)$. Another configura-
tion that falls in the Case 2 category
is possible in which $F_H(0)$ is greater
than $F^-(0)$. These two possibilities
result in somewhat different propaga-
tion characteristics between $F^-(0)$ and
$F^+(0)$. The situation illustrated in
Figure 69 will be described first.

$F_H(0) < F^-(0)$--In the region $F^-(0)$ to
$F^+(0)$, $Y < 1$ and $X > 1 - Y$. Therefore,
this region is cut off. $F_2$ is a typical
frequency in this region. This case is
shown in Figure 71.
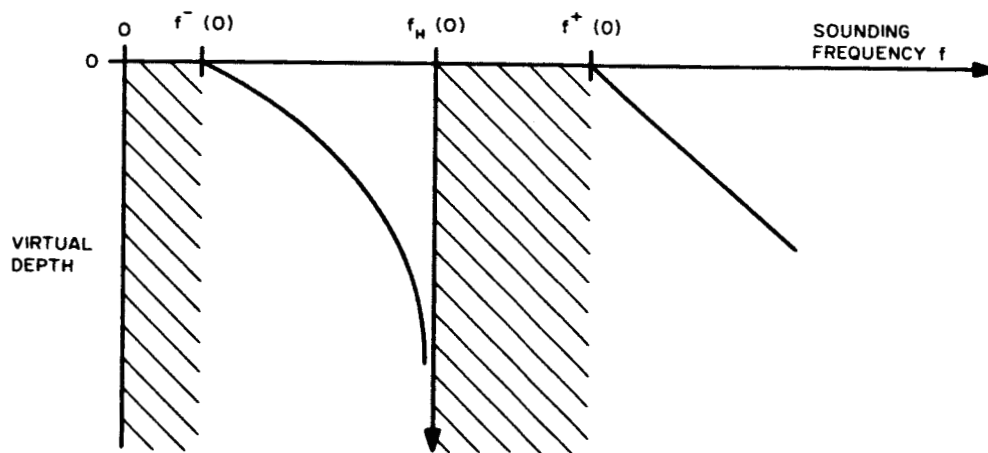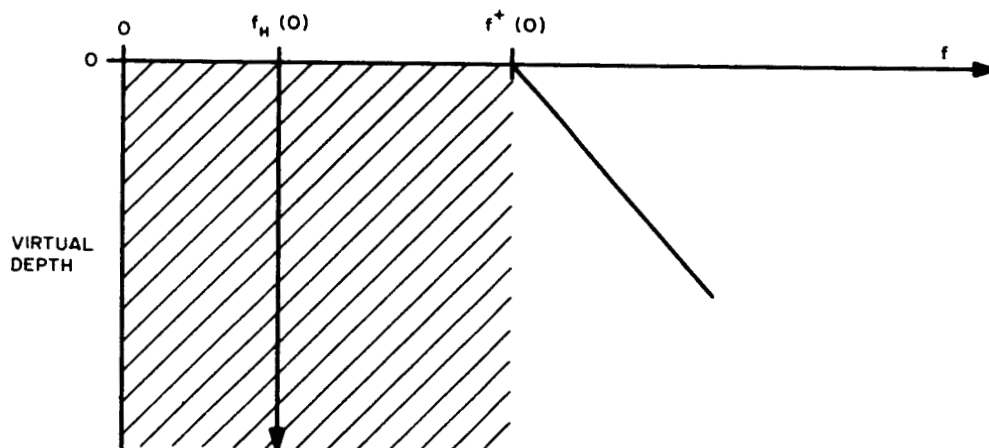
FIGURE 71.  SOUNDING DATA CHARACTERISTICS FOR CASES
1, 2, AND 3

$F_H(0) > F^-(0)$--In the region $F^-(0)$ to $F_H(0)$, $Y > 1$ and $X < 1 + Y$ and the x-wave propagates. From $F_H(0)$ to $F^+(0)$, $Y < 1$ and $X > 1 - Y$ and the x-wave is cut off. The propagation for this case is qualitatively identical to Case 1 as shown in Figure 71.

Case 3--Analysis of this case shows it to be identical to the two possibilities in Case 2. Case 3 may be considered a subcase of Case 2. The only difference is the crossover points of the gyro-frequency and plasma frequency curves of Case 2 which do not occur for Case 3. These crossover points do not enter the analysis, although they may bear on coupling in the region near $X = 1$.

# SECTION 5
## CONCLUSIONS AND RECOMMENDATIONS

The investigation of planetary ionosounding has resulted in the material contained in this report. In the techniques area, requirements and methods have been examined parametrically. Basic systems which are known from the radar technology were considered and related to planetary ionospheric sounding. An approach which is applicable to many missions out to very long ranges was developed that appears promising within the constraints of size, weight, and power to be expected in an interplanetary mission. This approach was worked out and described for a possible Voyager-type flight to Mars.

Many aspects of the techniques study remain to be investigated. A basic system, however, has been outlined. It is recommended that these studies be continued by constructing key elements of such a system to establish their feasibility and to proceed beyond this to the development of a complete breadboard system. Further study of various trade-offs would be included in this effort for optimization of the system with respect to a mission such as Voyager. Key elements of interest are pulse compression, coherent detection, and digital processing and storage. Although the state of the art is well established for these areas in radar, their application to ionospheric sounding is new. Once a breadboard system is evolved, the technique may be evaluated by bottomside sounding and with flight models by rocket tests. Finally, long-range sounding techniques should be considered as a possible means of synchronous or nearly synchrohous altitude measurement of the Earth's ionosphere.

In the theoretical area, virtual depth studies have been conducted using single- and double-layer models of ionospheres in the presence of a constant magnetic field. The incremental increase in path length due to the ionosphere, when sounding at long distances has been studied in detail and related to the electron density gradient, the planetary magnetic field, and the propagation frequency. Modifications of these results for closer approaches in which the sounder is placed at a finite altitude within the ionosphere have also been examined.

Virtual height profiles were constructed and studies were made of their interpretation and the methods of interpretation, both with and without knowledge of the magnetic field. A method was evolved which could provide a first approximation to both the true height profile and the magnetic field profile without the elaboration of the usual laminated model approach. However, for final refinements, the latter method is preferred.

A qualitative study was also made of the propagation characteristics of the medium in a magnetic field that varies with altitude.

Many aspects of the theoretical studies remain to be investigated. It is recommended that the effort be continued to include more comprehensive models which would include electron and ion temperatures, gravitational constants, and a magnetic field that vary with altitude. It is also highly recommended that an error analysis be performed for the purposes of improved data reduction and interpretation. In this regard, errors could be purposely introduced into virtual depth data derived from an ionospheric model. Such errors would represent measurement errors as well as those arising from physical assumptions. A true electron density profile corresponding to the resultant virtual depth data can be determined. On comparing the known model with this derived

data, errors in the computed profile that are due to the various virtual depth errors can be determined. The information gathered from this process can also be related to system accuracies and requirements and their variation with frequency.

In addition, it would be desirable to continue studies, for the purposes of data reduction, analysis and interpretation, to examine the use of the asymptotic behavior of the differential virtual depth and the dips in the virtual depth ionograms, since such characteristics are related to scale heights and magnetic fields. Such aspects of the virtual depth data provide ionospheric information without resorting to true depth computations and may serve to check the true depth results.

A further area for continued studies would be the application of the method of approximating the profiles from virtual depth data, as outlined in Section 4-E. In particular, the method can be applied to Alouette data and the results compared with the Alouette-derived profiles.

It would be desirable to include another study area in addition to the techniques and propagation studies. This area would include theoretical treatment of the planetary atmospheres and ionospheres, updating previous efforts by the inclusion of the Mariner 4 data and such other measurement data as may become available. This effort would attempt to predict the ionospheres of Mars and Venus, so as to establish more realistic models and to guide in the selection of appropriate sounding frequencies, the design of the sounder, and the analysis of data.

# REFERENCES

1. S. I. Rasool, "Structure of Planetary Atmospheres," AIAA Journal, Vol 1, p 6-19, 1963.

2. R. L. Carpenter and R. Goldstein, "Rotation of Venus, Period Estimated From Radar Measurement, Science, Vol 139, p 910, 1963.

3. L. Kaplan et al., "Analysis of Spectrum of Mars," Astrophysical Journal, Vol 139, p 1, 1964.

4. A. Dolfus, "Mesure de la quantité de Vapeur d'eau Contenue dans l'atmosphère de la planete Mars," Comptes Rendus, Vol 256, p 3009, 1963.

5. G. P. Kuiper, "Planetary Atmospheres and Their Origin," University of Chicago Press, Chapter 12, 1952.

6. G. de Vaucouleurs, "Physics of the Planet Mars," Faber, London, 1954.

7. G. de Vaucouleurs, "Remarks on Mars and Venus," Int Geophysical Research, Vol 64, p 1739, 1959.

8. V. I. Moroz, "The Infrared Spectrum of Mars," ($\lambda 1.1 - 4.1\mu$), Soviet Astronomy, Vol 8, p 273, 1964.

9. T. Owen and G. P. Kuiper, "A Determination of the Composition and the Surface Pressure of the Martian Atmosphere," Communications of the Lunar and Planetary Laboratory, Vol 3, No. 32, 1964.

10. G. P. Kuiper, "The Spectrum of Mars, 1-2.5 Microns, and the Structure of Its Atmosphere," Communications of the Lunar and Planetary Laboratory, Vol 3, No. 31, 1964.

11. A. Dolfus, "Planets and Satellites," University of Chicago Press, Chapter 9, 1961.

12. H. Spinrad, "Spectroscopic Temperature and Pressure Measurements in Venus Atmosphere," Publication of the Astronomical Society of the Pacific, Vol 74, p 187, 1962.

13. G. P. Kuiper, "Communications of the Lunar and Planetary Laboratory," Vol 1, No. 83, 1962.

14. H. Spinrad and E. H. Richardson, "An Upper Limit to the Molecular Oxygen Content of the Venus Atmosphere," Astrophysical Journal, Vol 141, p 282, 1965.

15. W. S. Adams and T. Dunham, Jr., Publication of the Astronomical Society of the Pacific, Vol 44, p 243, 1932.

16. A. Dolfus, "Observation de la Vapeur d'eau sur la planete Venus," Comptes Rendus, Vol 256, p 3250, 1963.

17. R. K. Sloan, "Scientific Results from Mariner Missions to Venus and Mars," Conference on the Exploration of Mars and Venus, Virginia Polytechnic Institute, August 1965.

18. A. J. Kliore et al., "Radio Propagation Measurements of Planetary Atmospheres and the Mariner 4 Occulation Experiment," National Meeting of the American Geophysical Union, Dallas, September 1965.

19. H. A. Taylor et al., "Direct Measurements of Helium and Hydrogen Ion Concentration and Total Ion Density to Altitude of 940 Kilometers," Int Geophysical Research, Vol 68, p 4339, 1963.

20. A. D. Danilov, "Model of Venus and Mars Ionospheres," Geomagnetism and Aeronomy, Vol 1, p 314, 1961.

21. J. E. Chamberlin, "Upper Atmospheres of the Planets," Astrophysical Journal, Vol 136, p 582, 1962.

22. G. Yanow, Journal of Astronautical Science, Vol 8, No. 4, p 103, 1961.

23. R. Norton, "A Theoretical Study of the Martian and the Cytherean Ionospheres," NASA Technical Note No. D-2333, July 1964.

24. M. G. McElroy et al., Journal of Applied Physics, Vol 141, p 1523, 1965.

25. R. D. Davies and D. Williams, "Observations of Mars at 21.2 cm," General Assembly of International Astronomical Union, Hamburg, 1964.

26. K. G. Budden, "Radio Waves in the Ionosphere," Cambridge University Press, 1961.

27.  D. H. Shinn and H. A. Whale, "Group Velocities and
     Group Heights from Magneto-ionic Theory," Journal of
     Atmospheric and Terrestial Physics, Vol 2, p 85, 1952.

28.  K. Rawer, "The Ionosphere," Ungar Publishing Company,
     1956.

29.  R. J. Fitzenreiter and L. J. Blumle, "Analysis of Top-
     side Sounder Records," NASA Report No. X-615-63-207,
     October 1963.

# BIBLIOGRAPHY

Airborne Instruments Laboratory, "Final Report for Javelin Radio Astronomy Rocket Probe (Flight 8.33)." Goddard Space Flight Center, January 1965.

S. J. Bauer, "On the Electron Density Distribution Above the F2 Peak," NASA Report No. D-1171, January 1962.

S. J. Bauer and R. E. Bourdeau, "Upper Atmosphere Temperatures Derived from Charged Particle Observations," Astrophysical Journal, Vol 19, p 218, 1962.

W. Becker, "Tables of Ordinary and Extraordinary Refractive Indices, Group Refractive Indices and $h'_{ox}$ (f) Curves for Standard Ionospheric Layer Models," Communications of the Planck Institute, No. 4, 1960.

C. E. Cook and J. E. Chin, "Linear FM Pulse Compression," Space/Aeronautics, Vol 34, p 124, 1960.

W. B. Davenport and W. L. Root, "Random Signals and Noise," McGraw-Hill, 1958.

T. Flattau and R. Donegan, "Final Report for Study of Topside Sounder for Mars and Venus Ionospheres from Mariner Spacecraft," (NASA Contract No. NASW-513), October 1963.

J. M. Kelso, "Doppler Shifts and Faraday Rotation of Radio Signals in a Time Varying Inhomogeneous Ionosphere, I. Single Signal Case," Journal of Geophysical Research, Vol 65, No. 12, p 3909, 1960.

J. M. Kelso, "Doppler Shifts and Faraday Rotation of Radio Signals in a Time Varying Inhomogeneous Ionosphere, II. Single Signal Case," Journal of Geophysical Research, Vol 66, No. 4, p 1107, 1961.

J. M. Kelso, "Radio Ray Propagation in the Ionosphere, McGraw-Hill, 1964.

J. R Klander et al., "The Theory and Design of Chirp Radars," Bell Systems Technical Journal, Vol 39, p 745, 1960.

J. A. Ratcliffe, "The Magneto-Ionic Theory and Its Application to the Ionosphere," Cambridge University Press, 1959.

S. A. Schelkunoff and H. T. Friis, "Antennas--Theory and Practice," Wiley, 1952.

M. I. Skolnik, "Introduction to Radar Systems," McGraw-Hill, 1962.

P. M. Woodward, "Probability and Information Theory With Applications to Radar," McGraw-Hill, 1953.

# APPENDIX I

## ASYMPTOTIC EXPRESSIONS FOR $\mu'$ AND COS $\emptyset$ NEAR THE REFLECTION POINT

Budden[26] gives the following asymptotic expressions for group refractive index.

1.  For an o-wave when X approaches unity and $\epsilon = 1 - X$:

$$\mu_o' \approx \sqrt{\epsilon}\,\frac{\cosec\theta}{\sqrt{\epsilon'}}\left\{1 - \frac{3}{2}\,\epsilon\,\cot^2\theta + 0(\epsilon^2)\right\} \qquad (I-1)$$

2.  For a x-wave when X approaches the reflection point $1 \pm Y$ and where $\epsilon = 1 \pm Y - X$:

$$\mu_X' \approx \left\{2\epsilon(1 \pm Y)(1 + \cos^2\theta)\right\}^{-\frac{1}{2}}\left\{2 \pm Y + 0(\epsilon)\right\} \qquad (I-2)$$

where the plus sign is used when Y > 1 and the minus sign when Y < 1.

3.  When $\theta = 0$, the longitudinal wave reflects at $X = 1 + Y$, therefore if we set $\epsilon = 1 + Y - X$ equation 22 may be rewritten as:

$$\mu_o' \approx \frac{1}{2\sqrt{\epsilon'}(1 + Y)^{\frac{3}{2}}}\left\{(2 + Y)(1 + Y) + \epsilon Y + 0(\epsilon^2)\right\} \qquad (I-3)$$

Near the reflection point, the following asymptotic evaluations are found for $\cos\emptyset$ and $\mu'\cos\emptyset$:

1. o-wave, $\Theta \neq 0^\circ$, $\epsilon = 1 - X$

$$\cos\emptyset = \sqrt{\epsilon} \qquad\qquad (I-4)$$

and

$$\mu_0' \cos\emptyset \approx \text{cosec}\,\Theta\left\{1 - \frac{3}{2}\epsilon\cot^2\Theta + 0(\epsilon^2)\right\} \qquad (I-5)$$

2. o-wave, $\Theta = 0^\circ$, $\epsilon = 1 + Y - X$

$$\cos\emptyset \approx \sqrt{\frac{2\epsilon}{2+Y}}\left\{1 - \frac{\epsilon}{2(2+Y)} + 0(\epsilon^2)\right\} \qquad (I-6)$$

and

$$\mu_0' \cos\emptyset \approx \frac{(2+Y)(1+Y) + \epsilon\frac{Y-1}{2} + 0(\epsilon^2)}{(1+Y)\left[2(1+Y)(2+Y)\right]^{\frac{1}{2}}} \qquad (I-7)$$

3. x-wave, $\epsilon = 1 \pm Y - X$ (+ sign if $Y > 1$,
   − sign if $Y < 1$)

   $\cos\emptyset$ is given by equation I-6 if $Y > 1$

$$\qquad\qquad (I-8)$$

$$\cos\emptyset \approx \sqrt{\frac{2\epsilon}{2-Y}}\left\{1 - \frac{\epsilon}{2(2-Y)} + 0(\epsilon^2)\right\} \text{ if } Y < 1$$

and

$$\mu_x' \cos\emptyset \approx \frac{2 \pm Y + 0(\epsilon)}{\left[(2\pm Y)(1\pm Y)(1+\cos^2\Theta)\right]^{\frac{1}{2}}} \qquad (I-9)$$

# APPENDIX II

## ASYMPTOTIC VALUES FOR DIFFERENTIAL VIRTUAL DEPTH OF o-WAVE IN ZERO FREQUENCY LIMIT ($\theta \neq 0$)

As the sounding frequency approaches zero, it is desirable to evaluate $\Delta h'(f)$ in the zero frequency or infinite Y parameter limit in the interest of completeness for the idealized problem considered. In fact, for a finite sounding altitude, the differential virtual depth is identically zero at the cutoff frequency for that altitude as defined by the Appleton-Hartree relation. This calculation not only completes the $\Delta h'$ curves by finding asymptotic values for Figure 37 but, much more importantly, serves as an independent check of the computer calculations.

In order to propagate an o wave at very low frequencies, the sounding vehicle must be assumed to be very far away in a region of sufficiently low electron density. When the sounding frequency approaches zero, the sounder altitude must in fact approach infinity. At very high altitudes the electron density is assumed to decrease exponentially with altitude. Therefore, using the slope given by equation 40 and the transformation $X = \sin^2 \emptyset$, equation 30 may be rewritten as

$$- \frac{\Delta h'}{H} = \int_0^{\pi/2} (\mu_0' - 1) \cot \emptyset \, d\emptyset \qquad (II-1)$$

and

$$\mu_0' = \frac{N}{D\mu} + \frac{1}{\mu} \qquad (II-2)$$

where

$$N = 1 - X - \mu^2 + \frac{Y^2}{2} \cos^2 \theta \; (1 - X^2)(1 - \mu^2)/R \qquad \text{(II-3)}$$

$$R = \sqrt{Y^2 \cos^2 \theta \; (1 - X)^2 + \frac{Y^4}{4} \sin^4 \theta} \qquad \text{(II-4)}$$

$$D = 1 - X - \frac{Y^2}{2} \sin^2 \theta + R \qquad \text{(II-5)}$$

$$\mu^2 = 1 - \frac{X(1 - X)}{D} \qquad \text{(II-6)}$$

As $Y \rightarrow \infty$, equations II-3 through II-6 become

$$R \approx \frac{Y^2}{2} \sin^2 \theta \qquad \text{(II-7)}$$

$$D \approx 1 - \sin^2 \emptyset \qquad \text{(II-8)}$$

$$\mu^2 \approx 1 - \sin^2 \emptyset \qquad \text{(II-9)}$$

Integral II-1 may now be broken into two parts:

$$\lim_{Y \rightarrow \infty} \left( \frac{-\Delta h'}{2H} \right) = \underbrace{\int_0^{\pi/2} \cot^2 \sin \emptyset d\emptyset}_{I_1} + \underbrace{\int_0^{\pi/2} (\sec \emptyset - 1) \cot \emptyset d\emptyset}_{I_2} \qquad \text{(II-10)}$$

The first integral evaluates simply to $I_1 = \cot^2 \theta$. The second integral, however, must be integrated as shown since separation of the integrand creates singularities. We know, in fact, that the logarithmic singularity of $-\int_0^{\pi/2} \cot \emptyset d\emptyset$

must be canceled by a corresponding singularity of $\int_0^{\pi/2}$ sec $\emptyset d\emptyset$. Letting $v = \sin \emptyset$, the second integral is

$$I_2 = \int_0^1 \frac{1 - \sqrt{1 - v^2}}{\sqrt{1 - v^2}} \frac{dv}{v} \qquad (II\text{-}11)$$

Further transformation letting $y = 1 - \sqrt{1 - v^2}$ simplifies the integration.

$$I_2 = \int_0^1 \frac{dy}{(2 - y)} = \ln 2 \qquad (II\text{-}12)$$

The low-frequency asymptotic limit is obtained from $I_1 + I_2$ and is plotted in Figure 40.

$$\lim_{\substack{f \to 0 \\ Y \to \infty}} \left( -\frac{\Delta h'}{H} \right) = 2(\cot^2 \theta + \ln 2) \qquad (II\text{-}13)$$

# APPENDIX III

## ZERO FREQUENCY LIMIT OF LONGITUDINAL WAVE ($\theta = 0$)

Using equations 31, 32, and 33, the differential virtual depth is

$$\frac{\Delta h'(Y)}{H} = \int_0^{\pi/2} (\mu_o' - 1) \frac{2 \sin \phi + Y}{\sin^2 \phi + Y \sin \phi} \cos \phi \, d\phi \qquad \text{(III-1)}$$

where

$$\mu_o' = \frac{(\sin^2 \phi + Y \sin \phi) \left[ \frac{2 + Y}{2(1 + Y)} - 1 \right]}{(1 + Y) \sqrt{1 - \frac{\sin^2 \phi + Y \sin \phi}{1 + Y}}} + \qquad \text{(III-2)}$$

$$\frac{1}{\sqrt{1 - \frac{\sin^2 \phi + Y \sin \phi}{1 + Y}}}$$

For very large values of Y, equation III-1 in a singly exponential layer becomes

$$\lim_{\substack{f \to 0 \\ Y \to \infty}} \left( -\frac{\Delta h'}{H} \right) \approx -\underbrace{\int_0^{\pi/2} \frac{\sin \phi}{2\sqrt{1 - \sin \phi}} \cot \phi \, d\phi}_{I_1} + \qquad \text{(III-3)}$$

$$\underbrace{\int_0^{\pi/2} \left( \frac{1}{\sqrt{1 - \sin \phi}} - 1 \right) \cot \phi \, d\phi}_{I_2}$$

The first integral evaluates simply to $I_1 = -1$. $I_2$ has once again been formulated so as to eliminate the singularity at $\emptyset = 0$. Letting $y = 1 - \sqrt{1 - \sin \emptyset}$ the following is obtained.

$$I_2 \approx \int_0^1 \frac{2}{(2 - y)} \, dy = 2\ln 2 \qquad \text{(III-4)}$$

Therefore, the desired result is

$$\lim_{\substack{\gamma \to \infty \\ f \to 0}} \left( \frac{\Delta h'}{H} \right) = 1 - 2\ln 2 \qquad \text{(III-5)}$$

# APPENDIX IV
## ASYMPTOTIC LOW-FREQUENCY LIMIT OF x-WAVE DIFFERENTIAL DEPTH

From equations 37, 38, and 39 we have for a single layer

$$- \frac{\Delta h'(Y)}{H} = \int_0^{\pi/2} (\mu_x' - 1) \frac{2 \sin \phi + Y}{\sin^2 \phi + Y \sin \phi} \cos \phi \, d\phi \qquad \text{(IV-1)}$$

where

$$\mu_x' = \frac{N}{D_\mu} + \frac{1}{\mu}$$

$$N = 1 - X - \mu^2 - \frac{Y^2}{2} \cos^2 \theta (1 - X^2)(1 - \mu^2)/R \qquad \text{(IV-2)}$$

$$D = 1 - X - \frac{Y^2}{2} \sin^2 \theta - R \qquad \text{(IV-3)}$$

R and $\mu$ are given by equations II-4 and II-6 respectively and $X = \sin^2 \phi + Y \sin \phi$.

When $f \to o$, the asymptotic expressions are as follows:

$$R \approx \frac{Y^2}{2} \sqrt{\sin^4 \theta + 4 \cos^2 \theta \sin^2 \phi} , \qquad \text{(IV-4)}$$

$$D \approx - \frac{Y^2}{2} d, \qquad \text{(IV-5)}$$

$$N \approx \frac{2Y^2 \cos^2 \theta \sin^4 \emptyset}{d(d - \sin^2 \theta)} \quad , \tag{IV-6}$$

$$\mu^2 \approx 1 - \frac{2 \sin^2 \emptyset}{d} \quad , \tag{IV-7}$$

where

$$d = \sin^2 \theta + \sqrt{\sin^4 \theta + 4 \cos^2 \theta \sin^2 \emptyset} \tag{IV-8}$$

The above asymptotic expressions are substituted into equation IV-1.

$$-\frac{\Delta h'}{H} \approx \int_o^{\pi/2} \frac{-4 \cos^2 \theta \sin^3 \emptyset}{d^{3/2}(d - \sin^2 \theta)(d - 2 \sin^2 \emptyset)} \cos \emptyset \, d\emptyset$$

$$+ \int_o^{\pi/2} \left\{ \sqrt{\frac{d}{d - 2 \sin^2 \emptyset}} - 1 \right\} \cot \emptyset \, d\emptyset \tag{IV-9}$$

The last integral, in the same manner as Appendixes II and III, has been written in this manner to cancel the singularity at $\emptyset = 0$.

In order to integrate $I_1$ and $I_2$, the first and second integrals of equation IV-9, respectively, we make the following change of variable:

$$d = y = \sin^2 \theta + \sqrt{\sin^4 \theta + 4 \cos^2 \theta \sin^2 \emptyset} \tag{IV-10}$$

$$- \frac{\Delta h'}{H} = \overbrace{\frac{1}{2\sqrt{2}\,\cos\theta} \int_{2\,\sin^2\theta}^{2} \frac{y - 2\,\sin^2\theta}{y\,\sqrt{2 - y}}\,dy}^{I_1} \qquad (IV\text{-}11)$$

$$+ \int_{2\,\sin^2\theta}^{2} \overbrace{\frac{y - \sin^2\theta}{y(y - 2\,\sin^2\theta)\,\sqrt{2 - y}}}^{I_2} \left[ \frac{2\,\cos\theta}{\sqrt{2}} - \sqrt{2 - y} \right] dy$$

Upon integration, we obtain

$$I_1 \approx -1 - \frac{\sin^2\theta}{2\,\cos\theta}\,\ln\frac{1 - \cos\theta}{1 + \cos\theta} \qquad (IV\text{-}12)$$

and

$$I_2 = -\frac{\cos\theta}{2}\,\ln\frac{1 - \cos\theta}{1 + \cos\theta} + \ln(2\,\sin\theta) \qquad (IV\text{-}13)$$

Combining the two integrals, the low-frequency limit of the x-wave differential depth is

$$\frac{\Delta h'}{H} \approx 1 + \frac{1}{\cos\theta}\,\ln\frac{\sin\theta}{1 + \cos\theta} - \ln(2\,\sin\theta) \qquad (IV\text{-}14)$$

Equation IV-14 is displayed graphically in Figure 42.

# NASA SCIENTIFIC AND TECHNICAL PUBLICATIONS

**TECHNICAL REPORTS:** Scientific and technical information considered
important, complete, and a lasting contribution to existing knowledge.

**TECHNICAL NOTES:** Information less broad in scope but nevertheless of
importance as a contribution to existing knowledge.

**TECHNICAL MEMORANDUMS:** Information receiving limited distribu-
tion because of preliminary data, security classification, or other reasons.

**CONTRACTOR REPORTS:** Technical information generated in connection
with a NASA contract or grant and released under NASA auspices.

**TECHNICAL TRANSLATIONS:** Information published in a foreign
language considered to merit NASA distribution in English.

**SPECIAL PUBLICATIONS:** Information derived from or of value to NASA
activities. Publications include conference proceedings, monographs, data
compilations, handbooks, sourcebooks, and special bibliographies.

**TECHNOLOGY UTILIZATION PUBLICATIONS:** Information on tech-
nology used by NASA that may be of particular interest in commercial and other
nonaerospace applications. Publications include Tech Briefs; Technology
Utilization Reports and Notes; and Technology Surveys.

*Details on the availability of these publications may be obtained from:*

## SCIENTIFIC AND TECHNICAL INFORMATION DIVISION

# NATIONAL AERONAUTICS AND SPACE ADMINISTRATION

Washington, D.C. 20546